

# Beyond solid-state lighting: Miniaturization, hybrid integration, and applications of GaN nano- and micro-LEDs

Cite as: Appl. Phys. Rev. **6**, 041315 (2019); doi: [10.1063/1.5096322](https://doi.org/10.1063/1.5096322)

Submitted: 30 May 2019 · Accepted: 26 November 2019 ·

Published Online: 19 December 2019 · Publisher error corrected: 20 December 2019



Hutomo Suryo Wasisto,<sup>1,2,a,b)</sup> Joan Daniel Prades,<sup>3,a)</sup> Jan Gülink,<sup>1,2</sup> and Andreas Waag<sup>1,2,b)</sup>

## AFFILIATIONS

<sup>1</sup>Institute of Semiconductor Technology (IHT), Technische Universität Braunschweig, Hans-Sommer-Straße 66, D-38106 Braunschweig, Germany

<sup>2</sup>Laboratory for Emerging Nanometrology (LENA), Technische Universität Braunschweig, Langer Kamp 6a, D-38106 Braunschweig, Germany

<sup>3</sup>MIND-IN<sup>2</sup>UB, Department of Electronic and Biomedical Engineering, Universitat de Barcelona, C/Martí i Franquès 1, E-08028 Barcelona, Spain

<sup>a)</sup>**Contributions:** H. S. Wasisto and J. D. Prades contributed equally to this work.

<sup>b)</sup>**Authors to whom correspondence should be addressed:** [h.wasisto@tu-braunschweig.de](mailto:h.wasisto@tu-braunschweig.de) and [a.waag@tu-braunschweig.de](mailto:a.waag@tu-braunschweig.de).

Tel.: +49 531 391 65322. Fax: +49 531 391 5844.

## ABSTRACT

Gallium nitride (GaN) light-emitting-diode (LED) technology has been the revolution in modern lighting. In the last decade, a huge global market of efficient, long-lasting, and ubiquitous white light sources has developed around the inception of the Nobel-prize-winning blue GaN LEDs. Today, GaN optoelectronics is developing beyond solid-state lighting, leading to new and innovative devices, e.g., for microdisplays, being the core technology for future augmented reality and visualization, as well as point light sources for optical excitation in communications, imaging, and sensing. This explosion of applications is driven by two main directions: the ability to produce very small GaN LEDs (micro-LEDs and nano-LEDs) with high efficiency and across large areas, in combination with the possibility to merge optoelectronic-grade GaN micro-LEDs with silicon microelectronics in a hybrid approach. GaN LED technology is now even spreading into the realm of display technology, which has been occupied by organic LEDs and liquid crystal displays for decades. In this review, the technological transition toward GaN micro- and nanodevices beyond lighting is discussed including an up-to-date overview on the state of the art.

© 2019 Author(s). All article content, except where otherwise noted, is licensed under a Creative Commons Attribution (CC BY) license (<http://creativecommons.org/licenses/by/4.0/>). <https://doi.org/10.1063/1.5096322>

## TABLE OF CONTENTS

I. INTRODUCTION .....	2
II. GAN LED TECHNOLOGY AND PROCESSING .....	3
A. Material aspects and epitaxy of planar architectures.....	3
B. Material aspects and epitaxy of 3D architectures .....	6
C. Top-down fabrication of 3D architectures .....	8
D. Laser micromachining and lift-off processing of GaN LEDs .....	11
E. Hybrid integration of GaN micro-LEDs with Si CMOS electronics .....	11
F. Transfer of GaN micro- and nano-LEDs onto flexible substrates.....	12

## III. GAN LED APPLICATIONS BEYOND SOLID-STATE

LIGHTING .....	12
A. High-brightness micro-LED displays.....	12
1. Micro-LED displays for augmented reality (AR) .....	12
2. Nano-LED arrays for super resolution microscopy.....	13
B. Visible light communication (VLC).....	14
1. Structure of the VLC system .....	14
2. Micro-LEDs as an emitter in the VLC system .....	14
C. Biomedical sensors and imaging systems .....	15
1. Compact lensless microscopes .....	16
2. Optoelectronic tweezers.....	18

3. Fluorescence-based sensors.....	20
4. Optogenetics .....	21
E. Chemical sensors for environmental monitoring..	24
1. Conductometric chemical sensors .....	24
2. Luminescent chemical sensors.....	26
3. Airborne micro-/nanoparticle sensors.....	28
IV. CONCLUSION.....	30

## I. INTRODUCTION

The research field of gallium nitride (GaN)-based semiconductors, with first light-emitting-diodes (LEDs) demonstrated in the early 1990s,<sup>1</sup> has since then been developed into a very mature semiconductor technology (Fig. 1). Main drivers have been solid-state lighting including LEDs and laser diodes,<sup>2–4</sup> as well as high-frequency (HF) and—more recently—power electronics.<sup>5–8</sup> Today, LEDs are an integral part of many consumer products like light engines for general lighting, smartphones, or automobiles, often enabling new functionalities (e.g., higher efficiency and endurance, more compact form factor, and higher design flexibility), if compared with their traditional counterparts.

Until now, both optoelectronic and electronic applications (e.g., LEDs, laser diodes, and FETs), have been based on planar approaches.<sup>9</sup> In particular, LEDs made for solid-state lighting need to be large (on the order of square millimeters) to achieve a high lumen output. This scaling behavior is contrary to the well-known Moore's law in silicon-based microelectronics. There, transistors are becoming smaller and smaller, with more and more functionality per area on the chip. As a consequence, cost reduction in LED fabrication has been—and still is—much more challenging, relying on a continuous optimization of nitride material growth methods and better fabrication strategies instead of only structure size reduction.

This continuous optimization has led to a steady increase in efficiencies, which will approach theoretical limits over the next few years<sup>10</sup> (see Fig. 1). A luminous efficacy of above 250 lm/W has become available not only in the lab, but also in the consumer market.

In 2014, Cree, Inc., an American LED manufacturer has demonstrated a world-record luminous efficacy of 303 lm/W from white high-power LEDs, which has surpassed the previous product-best value of 276 lm/W.<sup>11</sup> Meanwhile, in the same year, OSRAM Opto Semiconductors GmbH has obtained peak efficacies as high as 307 lm/W employing direct green LEDs emitting at 536 nm.<sup>9</sup> For comparison, the theoretical maximum efficacy is around 350 lm/W. An exact theoretical limit cannot be stated since this depends on the assumed quality of the “white” spectrum—in terms of color rendering index—of the LED emission. Finally, the systematic improvement of efficiency will lead LEDs to reach saturation values in efficiency over the next five years. Other challenges are now coming into focus, like cost reduction, new device concepts, and improvement in the accessible wavelength range from the blue-green into the UV and red spectral range.

This has consequences for global GaN research and development. While in the past the focus has been on material quality and its improvement (by understanding, e.g., epitaxy processes) as well as device design, it is now more and more shifting into processing technology. Until now, processing of “large” area devices, like power LEDs with 1 W light output with an area of 1 mm<sup>2</sup>,<sup>9</sup> has been intensively researched by GaN community. Today, however, new possibilities emerge from combining micro- and nanoscale fabrication techniques with GaN technology, paving the way toward micro- and nano-LEDs or nanosized field-effect transistors (nano-FETs). A rising amount of research budget is allocated in this direction due to good reasons. The potential markets to be addressed in the future are very attractive. GaN micro-LED technology might even become a core display technology not only for augmented reality (AR) applications, but also for large area screens. GaN nano-FET technology might spread out from HF electronics into power electronics and even into an integration of optoelectronic components (based on GaN) and complementary metal-oxide semiconductor (CMOS) technology based on silicon electronics.

The expectations are huge. Micro- or nanoscale GaN structures can be free of extended defects, building a perfect material platform

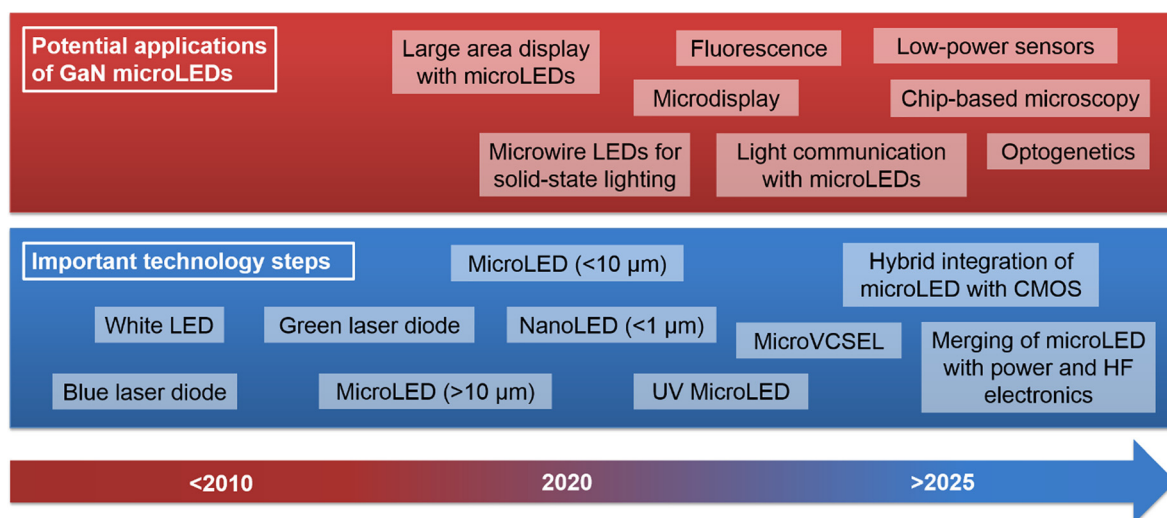


FIG. 1. Estimated road map for key applications of micro-LEDs including relevant technology milestones.

for future GaN technology. This is why—besides market pull—there is a strong technology push toward GaN micro- and nanodevices.

A first driver of innovation is related to the production of vertical GaN nanostructures. Today, it is possible to grow the 3D GaN nanostructures, embodying a full LED<sup>4,12,13</sup> or an FET<sup>6-8,14,15</sup> device in a vertical, core-shell configuration of only about a few hundred nanometers in diameter and a few micrometers in length (Fig. 1). Such 3D nano-LEDs and nano-FETs give access not only to extreme miniaturization, but also to (1) superior material properties (e.g., lower defect density), (2) better compatibility with other technologies (e.g., more resilience to lattice mismatch with the substrate and transferable to flexible carriers<sup>12</sup>), and (3) potential for complementary MOS approaches in nitrides (a CMOS-like technology, but based on GaN).

A second technology driver of innovation is the possibility of transferring electronic- and optoelectronic-grade GaN structures to silicon-based chips with microelectronic functionality. As a matter of fact, with laser lift-off methods,<sup>16</sup> the planar as-grown GaN structures can be transferred from the sapphire substrates needed to grow high-quality GaN to better suited substrates like silicon at a wafer scale.<sup>9</sup> Besides the cost argument, sapphire is a passive substrate with limited possibilities in terms of added functionality and micromachining. Therefore, the combination of GaN devices with active substrates—like silicon—opens the door to new developments that combine the advantages of GaN (superior optoelectronic, high frequency, and high-power properties), with the flexibility of CMOS (miniaturization and standardized highly integrated analog and digital functionalities).<sup>17</sup>

In contrast to traditional trends in lighting applications, these two enabling technologies are in the direction of miniaturization. As a consequence, emerging applications aim at exploiting the advantages of GaN technology (high-efficiency, long endurance, high brightness—not achievable by its organic counterparts) in the context of miniaturized and compact designs. This is the case for microdisplays<sup>18-20</sup>—the core technology for future augmented reality<sup>21</sup>—and for optical excitation in communications,<sup>22-24</sup> imaging,<sup>25</sup> and sensing<sup>26</sup> (Fig. 1).

The goal of this review is to discuss this technological transition toward GaN micro- and nanodevices and to provide an overview on the present state of the art. This is particularly related to GaN processing of micro- and nanoscale devices and their integration into flexible and silicon technologies, which are the newly emerging processing possibilities that push toward new applications of GaN far beyond the traditional markets of lighting. Some of these applications, like microdisplays, visible light communications (VLCs), imaging, and sensing, will also be discussed in detail.

## II. GaN LED TECHNOLOGY AND PROCESSING

### A. Material aspects and epitaxy of planar architectures

Due to the quite special material properties of GaN, metalorganic vapour-phase epitaxy (MOVPE) is by far the most often used growth technique today. At the high growth temperatures of 1000 °C and above needed for producing high-quality GaN, a high amount of active nitrogen has to be available to stabilize the GaN surface from dissociation. At the same time, reactive nitrogen atoms readily recombine to the very stable N<sub>2</sub> molecule, which is then lost for the chemical reaction. Ammonia (NH<sub>3</sub>) has been proven to be a very versatile nitrogen precursor for MOVPE. Tri-Ethy-Gallium (TEGa) and its aluminum and indium modifications are used with NH<sub>3</sub> for the growth of GaN,

AlN, and InN and all their ternary and quaternary alloys. Numerous very good reviews are available focusing on the MOVPE of as well as LED development for solid-state lighting,<sup>27-31</sup> so that details on both will only be described here where necessary.

It is this high growth temperature of MOVPE that makes the growth process incompatible with silicon microelectronics. Neither the MOVPE growth of GaN on processed silicon chips nor the processing of silicon electronic circuitry after the growth of GaN layers on top of silicon substrates seems to be a viable strategy to combine both worlds. Due to this incompatibility of jointly processing GaN and silicon on the same wafer, this review does not cover this type of monolithic integration, but focuses on hybrid integration of GaN and silicon microelectronic chips, with the main advantage that both types of devices can draw on separately optimized process technologies without any compromises.

Besides MOVPE, molecular beam epitaxy (MBE) has also been developed further to grow LED structures.<sup>32,33</sup> The limited throughput (in comparison to MOVPE), the complexity of working with ultrahigh vacuum, and the success of MOVPE have however prevented MBE from entering industrial production. MBE will therefore not be in the focus of this review.

Today, MOVPE of nitrides is well under control and LED heterostructures have been optimized at a very high level. Modern LED structures consist of many layers, up to 100 and more, in order to guarantee key requirements for a good LED: high efficiency in current injection, efficient photon generation and photon extraction, and stable operation conditions along the lifetime of more than 50 000 hours. This optimization is related to active regions with highest internal quantum efficiency (IQE), efficient electron blocking layers, defect-reduced buffer layers, *p*-GaN layers with reduced absorption, and increased conductivity, in combination with an optimization of chip processing for achieving highest possible photon extraction and lowest feasible driving voltages. All this has resulted in more than 200 lm/W of lamp efficacy in 2014,<sup>34</sup> with these values further improving.

Initial development has been devoted to LEDs with wavelengths in the blue spectral range (400 nm–460 nm). For this spectral range, the indium content in the InGaN quantum wells (QWs), which serve as active regions, is in the 20% range. This is large enough for an efficient confinement of both electrons and holes. On the other hand, the indium content in “blue” quantum wells is still sufficiently small to allow to circumvent substantial material degradation due to the increasing lattice mismatch and the dissimilar material properties of InGaN and GaN.<sup>35-37</sup>

The fact that GaN LEDs with efficiencies close to their theoretical limit can be fabricated should not obstruct the view on still existing major challenges. One of these challenges is the so-called droop problem.<sup>38-40</sup> The maximum efficiency of blue GaN LEDs is achieved at relatively low current densities of a few amperes per square centimeter. Even though the fabricated devices have been efficient, their overall light output under these conditions is too low for high-power and low-cost GaN LEDs. Therefore, LEDs are usually operated at much higher current densities, in the range of 30–70 A/cm<sup>2</sup>. This increases the total light output, but at the same time reduces the device efficiency. The origin of this decrease was a matter of discussion over the past years. The community has agreed that Auger recombination processes contribute substantially and dominantly to carrier loss over the barriers, being the main course for carrier overflow and hence the reduction of

efficiency at higher current densities. Therefore, LEDs today use multiple quantum wells as active regions to reduce the carrier concentrations during operation. Hence, Auger effects can be minimized.

These blue LEDs exhibit a very interesting property, which initially has been unexpected. InGaN quantum wells in this spectral range can achieve IQEs of above 90%, even though the films are “suffering” from a density of extended defects of above  $10^8 \text{ cm}^{-2}$ .<sup>40,41</sup> This particularly attractive property of InGaN quantum wells is the main reason why the heteroepitaxy on sapphire—despite a huge lattice mismatch and despite a large mismatch in thermal expansion coefficients—has been so successful. The reason for this insensitivity to defects has been a matter of long debate. The keys to it are laterally inhomogeneous potentials in the quantum well (QW), caused by indium gradients, blocking carriers away from dislocations.<sup>42</sup> For GaN quantum wells, this localization is no longer active, so that UV LEDs presently have much worse performance data.

Starting out from the blue spectral range, it is a huge challenge extending the emission wavelengths beyond the green into the red and infrared (IR) range. For tuning the bandgap of the active region into the red and infrared, a much higher amount of indium has to be used. The respective lattice mismatch in combination with the incompatibility of InN and GaN concerning ideal growth temperatures is challenging.<sup>43</sup> Nevertheless, InGaN technology is stepwise pushing into the green and red ranges. Indeed, green InGaN LEDs have a lower wall plug efficiency. However, it has recently been demonstrated that this is not due to a reduced material quality, but because of an increased droop effect instead.<sup>44,45</sup> At lower current densities, the performance of green LEDs is almost the same as that of blue LEDs. The originally stated “green gap” for LEDs, meaning that only blue InGaN and red InGaAlP high-power LEDs can be fabricated, with an efficiency gap in between, is closing. The reduction in efficacy is mainly due to the shift in efficiency maximum to lower current densities rather than a principal issue.<sup>44</sup> Further work will very likely eliminate the green gap in the future.

The extension of the spectral range into the UV is also very challenging, but due to different reasons. In the UV spectral range, GaN quantum wells need to be used as active regions, relaxing the conditions for carrier localization. The strong carrier localization in InGaN quantum wells is believed to be the main reason for the stability of nitride LEDs against the existence of extended defects. Figure 2 shows this effect. Whereas, IQEs of close to 100% can be reached in InGaN quantum wells even at defect densities as high as  $10^8 \text{ cm}^{-2}$ , the efficiency is reduced to less than 0.1% for UV-C at similar defect densities. Reducing the defect densities is believed to be a key requirement for future UV LED technology.<sup>46–48</sup>

A current strategy for reducing threading dislocation density includes growth on AlN bulk substrates [threading dislocation density is around  $10^3 \text{ cm}^{-2}$  (Ref. 49)]. However, these bulk substrates are very expensive and only available up to 2 in. in diameter, thus not meeting the requirements for high-throughput production. In addition, high-quality AlN bulk substrates suffer from strong absorption in the UV range.<sup>50,51</sup> An effective reduction of the defect density in AlN/AlGaN templates is urgently needed in order to increase the IQE of UV LEDs for all wavelengths while still maintaining cost effectiveness and scalability of substrate sizes.

All the developments described so far have been obtained using a planar approach: growing planar thin film structures on flat wafers, e.g., on 6-in. sapphire. Meanwhile, many companies offer this material commercially at the wafer level, so that it can be a serious basis for future technology development. Also, GaN foundry services offer even a full-scale wafer level processing of GaN LEDs and other microdevices.<sup>52</sup>

For state-of-the-art planar InGaN-based blue LEDs, the external quantum efficiencies (EQEs) of more than 60% can be regularly obtained.<sup>9,53</sup> The highest reported EQE even reached maximum values under optimized operation conditions of beyond 80% for InGaN-based blue LEDs at 50 mA with a die size of  $450 \times 450 \mu\text{m}^2$ .<sup>54</sup> At a regular forward-bias current of 350 mA, these devices have an emission

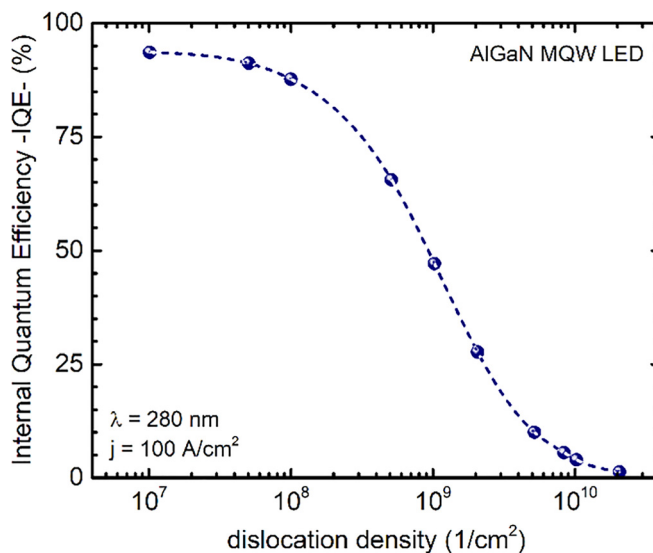


FIG. 2. Simulated internal quantum efficiency (IQE) against the dislocation density for 280 nm UV LEDs.<sup>48</sup> Reproduced with permission Kneissl et al., Semicond. Sci. **26**(1), 014036 (2011). Copyright 2011 IOP Publishing.

wavelength, an output power, and an EQE of at 440 nm, 756 mW, and 71.0%, respectively. Due to a huge challenge to grow a high-quality InGaN QW with low strain, InGaN-based green LEDs exhibit a typical external quantum efficiency (EQE) of ~20% at 20 mA, which is much lower than that of top-level blue LEDs.<sup>55</sup> Green LEDs with a record high EQE of 28.3% at 20 mA, a die size of  $1 \times 1 \text{ mm}^2$ , an output power of 13.3 mW, and an emission wavelength of 529 nm were reported using semipolar plane concepts.<sup>56</sup> Thus, to improve the efficiency of GaN-based green LEDs, several techniques have been continuously investigated, e.g., employing restrained layers underneath the QW, inserting AlGaN between the QW and the barrier, and growing semipolar/nonpolar QWs. Meanwhile, for AlGaN-based UV LEDs the highest reported EQE and output power in the UV-C range (at 280–300 nm emission) are 14.3% and 153.4 mW, respectively, which are believed to be continually improved in the next few years.<sup>57,58</sup> The shortest emission wavelength reported to date for UV LEDs is 210 nm by Taniyasu *et al.* from NTT Basic Research Laboratories, Japan.<sup>59</sup>

Several approaches have been developed and attempted to overcome efficiency droop in GaN LEDs, e.g., (1) modification of QWs using a thick well, double heterostructure or increased QW number in the active region to lower the effective carrier density in QWs,<sup>60–62</sup> (2) suppression of quantum-confined Stark effect (QCSE) in c-plane based on energy band engineering to shorten the radiative recombination lifetime [e.g., employing the staggered QW,<sup>63,64</sup> creating thin barrier coupled QWs,<sup>65</sup> and replacing QWs with quantum dots (QDs)<sup>66</sup>], (3) polarization matching of individual quantum barrier and well layers of the MQW active region by utilizing ternary InGaN or quaternary AlInGaN barriers,<sup>67,68</sup> (4) replacement of c-plane by nonpolar/semipolar planes or engineering of micro-/nanostructures with semi-/nonpolar facets,<sup>69–71</sup> (5) insertion of additional carrier recombination channels (e.g., surface plasmon coupling) to shorten the carrier lifetime,<sup>72,73</sup> and (6) conversion of spontaneous emission to stimulated emission by introducing a stimulated radiative recombination process.<sup>74</sup>

Among them, making the QWs thicker is considered to be the simplest way. However, when using thicker active layers (QW) and double heterostructures, the material quality and recombination rate of QWs can be worsened because of the formation of additional defects and accumulation of strain as well as a stronger quantum-confined Stark effect.<sup>75</sup> Whereas although the other mentioned methods are found to be efficient for reducing the internal electric field in the active region,<sup>61</sup> several challenges were still often faced in the realization of the device structures, i.e., more complicated growth and fabrication conditions of samples with other materials and structures than c-plane InGaN/GaN QWs. Thus, in 2016, Yoo *et al.* introduced another effective technique to overcome the efficiency droop by utilizing conventional c-plane InGaN/GaN QW structures having thinner barriers and an increased number of wells with a fixed single well thickness while keeping the same total active layer region (i.e., thickness of whole wells and barriers).<sup>76</sup> By employing this c-plane InGaN-based LED structures, internal electric field and carrier density can be reduced dramatically without complicated bandgap engineering and material quality decay, which improves overall efficiency (i.e., IQE is higher than 80%) and reduces efficiency droop issues. At the present status, even though massive experimental progress has been made to understand the efficiency droop in GaN LEDs, the debate on this problem has not been over yet.<sup>75</sup> Thus, several questions have still

arisen related to, e.g., the comparison of droop in InGaN LEDs with that in AlGaInP red LEDs, the most dominant factor for LED droop, accurate evaluation of LED efficiency without any assumption, and further feasible solutions to address the droop.

From the different strategies that can be applied to address the efficiency droop, the use of nonpolar and semipolar orientations has been vigorously researched since early work from Walterteit *et al.* in 2000<sup>77</sup> to boost the LED efficiency in the green spectral region by reducing the quantum-confined Stark effect and increasing the indium incorporation efficiency.<sup>56,71,78,79</sup> This is due to the fact that nonpolar and semipolar LEDs have numerous potential advantages over those c-plane counterparts (e.g., minimized polarization fields, reduced dependence on alloy content, larger wavefunction overlaps, increased optical matrix elements, faster recombination rates, and higher optical gain, more wavelength-stable emission, smaller hole effective mass, good emission anisotropy, and higher device design flexibility).<sup>71</sup> Anisotropic in-plane biaxial strain in nonpolar and semipolar orientations can boost the valence band degeneracy<sup>80</sup> and enable polarized light emission as well as anisotropic optical gain.<sup>81</sup> By eliminating the quantum-confined Stark effect, design of active regions can be made more flexible, where wide QWs can be implemented without putting concern on charge separation.<sup>82</sup> For InGaN-based blue LEDs employing various semipolar planes, the reported devices show good performances, in which an output power of 0.24–37.0 mW, efficiency (EQE) of 0.43%–80.8%, droop of 3.7%–71.4%, and peak electroluminescence wavelength of 407–480 nm at 20 mA have been demonstrated.<sup>56</sup> Compared to c-plane LEDs, the semipolar LEDs can have much lower efficiency droop, especially at high current density (i.e., an efficiency droop of only 5% at  $100 \text{ A/cm}^2$  and 18% at  $300 \text{ A/cm}^2$ ).<sup>83,84</sup> By incorporating more Indium content, in recent years, InGaN-based green LEDs with different semipolar planes have been reported showing an increasing trend on their device performances in terms of output power (2.3–13.3 mW), efficiency (EQE of 4.0%–28.2%), droop (24.3%–57.1%), and spectral response (peak electroluminescence wavelength of 516–529 nm at 20 mA).<sup>56,84–86</sup> Table I lists the recently developed high-performance blue and green InGaN/GaN LEDs.<sup>54,56,82,84–92</sup> More comparison of the LED device structures and performances can be found in Ref. 56. It should be noted that almost all those InGaN blue and green LEDs were grown on bulk GaN substrates, in which UC Santa Barbara, USA, has been the most active developer in this semipolar LED optimization. The trade-offs between the modulation bandwidth and efficiency (IQE) for nonpolar and semipolar InGaN/GaN LEDs have also been investigated,<sup>71,93</sup> where the bandwidth-IQE product is found to be a potential figure of merit for optimizing speed and efficiency in InGaN/GaN LEDs, especially for visible light communication (VLC).

Another approach to access nonpolar and semipolar planes is to grow micro-/nanostructures with exposed nonpolar or semipolar facets. Depending on the applied mask geometries and growth conditions, various micro-/nanostructure architectures can be realized (e.g., wires or fins as well as nonpolar or semipolar).<sup>4,56</sup> Because of the reduced or eliminated polarization-induced quantum-confined Stark effect, modulation bandwidth in nonpolar and semipolar InGaN/GaN LEDs can be enhanced. A modulation speed and a record 3 dB modulation bandwidth of 1.1 GHz and 1.2 GHz, respectively, have been demonstrated using GaN/InGaN coreshell nanowire LEDs with primary nonpolar active regions.<sup>71,94</sup> It is believed that further research

**TABLE I.** Comparison of high-performance blue and green InGaN/GaN LEDs. Wavelength is peak electroluminescence wavelength at 20 mA. Light output power (LOP) and external quantum efficiency (EQE) are values at 20 mA. Droop is calculated at 100 mA, except that Refs. 89 and 88 are calculated at 80 mA.

Year (Reference)	Developer	LED type, plane, and structure	Wavelength (nm)	Light output power (mW)	EQE (%)	Droop (%)
2006 (Ref. 84)	Kyoto University and Nichia Corporation, Japan	Green, $(1\bar{1}2)$ , 3 nm SQW	527	2.3	4.0	31.7
2007 (Ref. 85)	UC Santa Barbara, USA	Green, $(1\bar{1}2)$ , 4 nm 6 QWs	516	5.0	10.5	49.8
2008 (Ref. 86)	UC Santa Barbara, USA	Green, $(1\bar{1}2)$ , 4 nm 6 QWs	519	9.0	18.9	44.4
2010 (Ref. 89)	UC Santa Barbara, USA and Sharp Corporation, Japan	Green, $(20\bar{2}1)$ , 3.5 nm SQW	516	9.9	20.4	57.1
2010 (Ref. 54)	Nichia Corporation, Japan	Blue, $(0001)$ , 3 nm 6 QWs	460	37.0	80.8	18.3
2010 (Ref. 90)	UC Santa Barbara, USA	Blue, $(10\bar{1}\bar{1})$ , 3 QWs	411	31.1	54.7	3.7
2010 (Ref. 91)	UC Santa Barbara, USA	Blue, $(10\bar{1}\bar{1})$ , 3 nm 6 QWs	420	22.8	39.5	4.2
2011 (Ref. 92)	UC Santa Barbara, USA	Blue, $(20\bar{2}\bar{1})$ , 3 nm 3 QWs	423	30.6	52.2	8.5
2012 (Ref. 87)	UC Santa Barbara, USA	Blue, $(20\bar{2}\bar{1})$ , 12 nm SQW	446	28.2	52.7	4.7
2013 (Ref. 88)	UC Santa Barbara, USA	Green, $(20\bar{2}\bar{1})$ , 3 nm SQW	518	5.8	11.9	56.5
2014 (Ref. 82)	UC Santa Barbara, USA	Blue, $(30\bar{3}1)$ , 15 nm SQW	413	29.8	49.5	9.5
2018 (Ref. 56)	Arizona State University, Sandia National Laboratories, UC Santa Barbara, USA	Green, $(20\bar{2}\bar{1})$ , 3.5 nm SQW	529	13.3	28.2	24.3

related to nonpolar and semipolar III-nitrides will continuously be conducted in the upcoming years to increase the efficiency, especially for green LEDs.

Downscaling of InGaN LEDs mitigates the efficiency droop effect, as their electrical and optical properties are improved in micro/nano-LEDs.<sup>38,95,96</sup> It has been reported that by scaling down the LED from 200 to 20  $\mu\text{m}$ , the peak EQE occurs at a higher injection current density for smaller LEDs. In this case, a peak EQE of 83.7% was obtained in the 20  $\mu\text{m}$  micro-LED compared to that in the 80  $\mu\text{m}$  micro-LED (only 70.2%). At a bias voltage of 10 V, the measured current densities of 200  $\mu\text{m}$  and 20  $\mu\text{m}$  LEDs were 20 A/cm<sup>2</sup> and 492 A/cm<sup>2</sup>, respectively. A uniform current spreading (larger fraction) in smaller micro-LEDs can enhance their electrical property<sup>97</sup> and EQE.<sup>98</sup> Besides, having a reduced size, the current crowding effect in the active region is less significant, leading to reduced Auger recombination probability and local heating.<sup>99</sup> It was also demonstrated that strain relief can further improve EQE characteristics in smaller InGaN micro-LEDs (diameter size < 50  $\mu\text{m}$ ), apart from the current spreading effect.<sup>97,98</sup> Strain relaxation reduces the quantum confined Stark effect and creates a less tilting band diagram, which consequently increases the overlap of the electron and hole wavefunctions and provides more suppression of Auger recombination, leading to enhanced radiative recombination and reduced nonradiative recombination probabilities. Thus, it will improve the overall quantum efficiency. As a result, the efficiency droop can be lowered while reducing the LED size, which then leads to the possibility of deploying micro-/nano-LEDs as the building block for large effective-area, high brightness emitters.

## B. Material aspects and epitaxy of 3D architectures

In the past years, however, another approach has gained substantial interest and a lot of work has been devoted to 3-dimensional (3D)

GaN architectures like nanorods and nanofins (see Fig. 3). The original motivation for 3D architectures has been that these high-aspect micro- and nanostructures possess some key features, which potentially are very attractive for future devices: (1) increasing the active area in core-shell architectures by more than a factor 10 and (2) being free of extended defects (3) enabling nonpolar *m*- or *a*-oriented sidewall quantum wells. Consequently, such 3D architectures address the two key challenges, which have been mentioned before: reducing the current density in core-shell architectures for potentially reducing droop and enabling better UV LEDs by making low defect density LEDs available.

Switching to 3D growth rather than planar growth in MOVPE makes a substantial difference. It took many years of intense research to finally have vertical MOVPE growth of GaN nanorods or nanofins under control. Whereas pulsed growth techniques were in the focus during the early days of GaN nanowires by metal-organic chemical vapor deposition (MOCVD),<sup>100,101</sup> later continuous growth methods have been developed.<sup>4,102–107</sup> The strategies are usually based on substrates patterned by a passivating mask with hole or line patterns. SiO<sub>2</sub> has turned out to be a versatile and thermally stable mask on GaN buffers on the sapphire substrate. Due to the amorphous nature of the mask, a 100% selectivity can be achieved, provided the openings are not too far apart, since no chemical bonds are available for the incorporation of gallium or nitrogen on the mask. MOVPE growth can be tuned into a mode where not only growth on the mask surface, but also lateral growth in the GaN openings is inhibited.<sup>103,108</sup> For that, very low V/III ratios must be used during growth. It has also been shown that silicon doping during growth substantially enhances the vertical growth rates.<sup>103,109,110</sup> Initially, the development of 3D GaN microrods has been hampered by the lack of suitable characterization techniques in 3 dimensions. Cathodoluminescence in combination with nanoneedles for electrical contacts has been demonstrated to be a very versatile tool for analyzing the optical

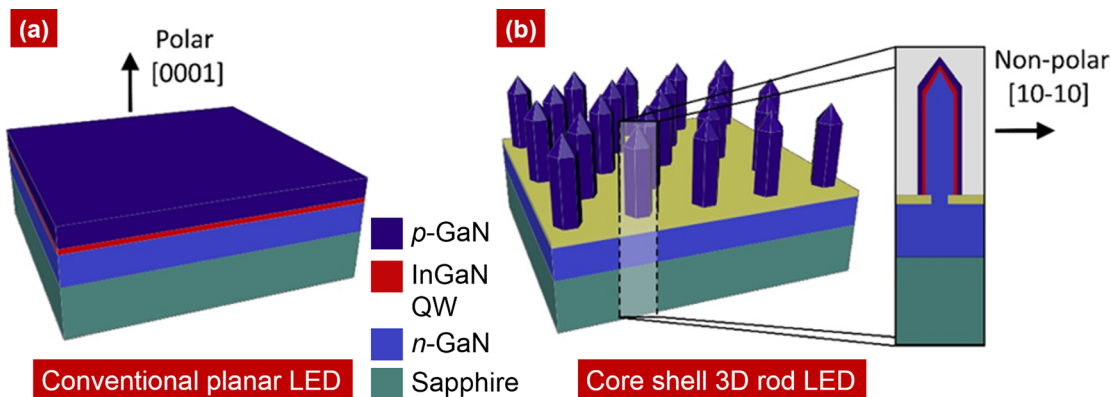


**FIG. 3.** 3D GaN architectures: (a) planar thin film with c-plane quantum wells and (b) high-aspect-ratio microrods with nonpolar a- or m-quantum wells at the sidewalls.

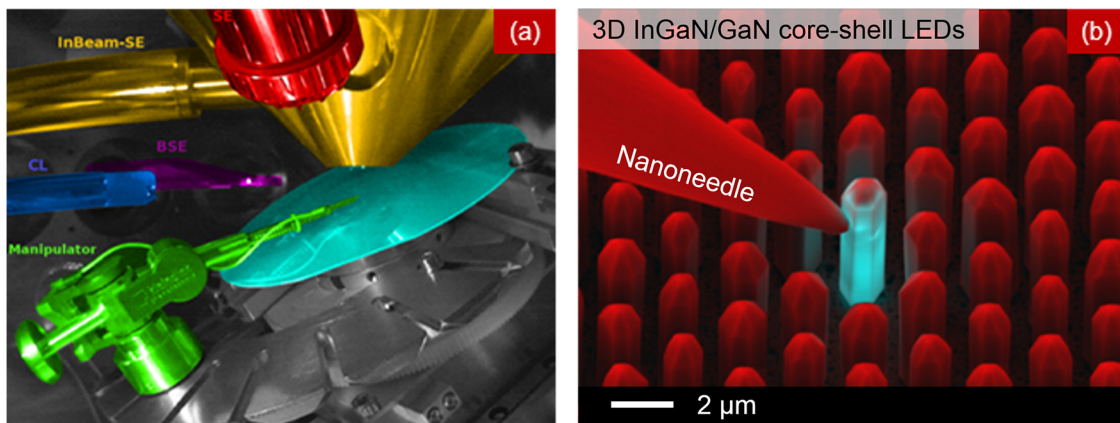


**FIG. 4.** (a) Geometry of the cathodoluminescence setup equipped with nanoneedles for electrical contact. (b) Electron beam induced current image of a core-shell p-GaN/InGaN/n-GaN LED indicating a complete coverage of the micro-LED surface with p-type GaN.

and electrical properties of 3D GaN structures with high spatial resolution [see Figs. 4(a) and 4(b)].<sup>110,111</sup>

Meanwhile, the first blue and even white microrod LEDs have been demonstrated (Fig. 5). For white microrod LEDs, the regular large grain phosphors had been converted into highly efficient micro-grain phosphors in order to fill the phosphor particles in between the microrods.<sup>105</sup>

Even though huge progress could be made, nanorod LEDs today do not yet reach efficiencies of their blue-emitting planar counterparts. It is likely that this is due to the limited research effort put into 3D processing. In any case, a physical limitation has not yet been identified for that. Rather, sidewall quantum wells with high IQEs of up to 60% (Ref. 112) have been demonstrated. However, these high IQEs could not yet be transferred into micro-LED devices with high external quantum efficiency (EQE), being reported to be about 10%.<sup>105</sup> One of the reasons for the somewhat low speed of development is the difficulty in analyzing 3D nanorods in the same way planar thin films are analyzed, which is retarding technological progress. It has, e.g., only recently become clear that a pronounced gradient of indium incorporation along the sidewalls could be one of the reasons why processed

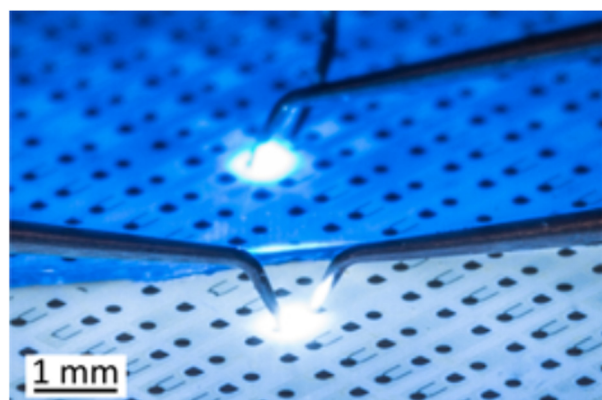


**FIG. 5.** Emission from the first phosphor converted white microrod LED. Reprinted with permission from Schimpke *et al.*, Phys. Status Solidi **213**, 1577 (2016).<sup>105</sup> Copyright 2016 Wiley-VCH Verlag GmbH & Co. KGaA.

microrod LEDs do suffer from low EQEs.<sup>102,110</sup> In addition, data on the IQE along the sidewall of a high-aspect-ratio microrod are still very limited. This, however, would be a key element for further optimization.

3D architectures are particularly interesting for the UV spectral range, with many additional advantages. Besides the possibility to obtain a defect-free material, an additional aspect is related to a change in the valence band sequence in AlGaN for a higher Al content (see Fig. 6).<sup>113</sup> Due to this modified valence band structure, UV LEDs based on conventional *c*-plane quantum wells tend to be polarized in a way that is detrimental to vertical emission. In contrast to that, the polarization in nonpolar, *a*-, or *m*-oriented quantum wells is favorable for vertical emission. Therefore, research efforts are presently on the way to explore 3D architectures for the fabrication of UV microrod or microfin LEDs.<sup>114,115</sup>

While most of the studies on 3D architectures have focused on nanorod or microrod geometries, fin geometries are very promising and have recently attracted substantial interest.<sup>102,116</sup> Fin architectures have the key advantage that the analysis of their internal properties is much easier compared to that of microrods. In contrast to microrods, open internal surfaces of fin samples emerge in a controlled and reproducible way after only cleaving the sample. These cross sections can then be analyzed optically, e.g., by cathodoluminescence and electrically, e.g., by nanoneedles in a customized SEM setup [see Fig. 4(a)].<sup>110</sup> Another substantial advantage of fins related to microrods is the fact that their 3D epitaxy seems to exhibit a much larger stable growth window in comparison to their microrod counterparts. Fins with dimensions in the micrometer range can be produced homogeneously on large substrates.<sup>116</sup> Many details on fin growth have recently been reported. It remains to be seen whether all that knowledge can be transformed into highly efficient fin LEDs.

Even though the 3D growth of GaN structures like microrods or microfins is well under control, the requirement of a low V/III ratio during growth and the most frequently used high silicon doping have put some restrictions on the properties of GaN.<sup>116</sup> For core-shell LEDs, a highly doped GaN in the core is advantageous. For other devices, however, it might be necessary to adapt composition or doping profiles along the *c*-axis of the 3D structure. This is, e.g., the case for vertical FETs.<sup>7</sup> In such cases, another approach for fabrication of 3D structures could be advantageous, which is offering a better control on

vertical material and doping profiles: patterning and top-down etching of the planar parent material.

### C. Top-down fabrication of 3D architectures

Top-down patterning methods, generally by means of etching techniques, are introduced as a low-cost but highly efficient way toward fabrication of high-aspect-ratio 3D GaN micro-/nanostructures, which are mainly employed by researchers for implementations of both optoelectronic and electronic devices.<sup>117,118</sup> In the last few years, this technique has more and more attracted immense attention, as it has achieved an amazing degree of control.<sup>119</sup> In comparison to the direct 3D MOVPE growth of high-aspect-ratio microstructures, the top down approach is much more flexible, as the etching processes are directly performed on GaN epitaxial or bulk wafers. Prior to etching, the thin film architecture (i.e., layer stack) defines the vertical design of the final microstructures in a first and fully independent step, in which the dimensions of micro-/nanostructures are later defined by lithography and subsequent etching processes. Figure 7 illustrates the morphological changes of 3D GaN micro-/nanostructures during the top-down fabrication process using a hybrid dry/wet etching concept.

The high degree of control both at the micro- and nanoscale is based on precise vertical and lateral etching in combination with a proper mask material. Similar to the 3D silicon top-down approach,<sup>120,121</sup> plasma dry etching [e.g., inductively coupled plasma reaction ion etching (ICP-RIE)] can be directly used to create GaN micro-/nanostructures, using hard materials (e.g., oxides or metals) as etching masks. The masks can be patterned into arbitrary geometries by standard lithography [e.g., photolithography, nanoimprint lithography, colloidal nanoparticle lithography, or electron beam lithography (EBL)].<sup>14,122–126</sup> The fabrication of large-area GaN nanocolumns on a Si (111) substrate with a sidewall oblique angle of 86° by using chlorine-based ICP chemistries has been demonstrated by Paramanik *et al.* in 2012.<sup>127</sup> Besides the standard Cl<sub>2</sub>-based chemistries during ICP etching, gas mixtures of SF<sub>6</sub>/H<sub>2</sub> have also been reported for dry etching of GaN.<sup>13,128</sup> In contrast to ICP etching of silicon nanostructures, GaN nanostructures usually possess damaged surfaces after ICP etching, due to the physical ion bombardment effects [see Fig. 7(a)], which are consequently not appropriate to be directly employed for building surface sensitive devices (e.g., FETs, LEDs, and laser diodes).<sup>129</sup>

As an alternative to dry etching, anisotropic etching using wet chemical etchant solutions has also been reported to result in GaN nanostructures, usually resulting in much smoother surfaces. In 2011, the fabrication of vertical GaN nanowire arrays on a sapphire substrate with well-aligned *c*-axis orientation by using a conventional electrode free photoelectrochemical method has been reported by Liu *et al.*<sup>130</sup> The etchant has been a mixed base solution of 1 M KOH and 0.1 M K<sub>2</sub>S<sub>2</sub>O<sub>8</sub>. The process is assisted with a 150 W Xe lamp as the UV light source generating free holes at the material surfaces and by that promoting the oxidation process. This etching process, however, is strongly dependent on dislocations, meaning that the etching solution can “dig down” along the threading dislocations. Thus, at the end of the etching process, a high material quality can be achieved regardless of the limitation of precise control in the nanowire number, location, and dimension (see Fig. 7).<sup>14</sup>

Later, a two-step hybrid etching method, involving sequential processes of dry and wet etching, has been proposed by several

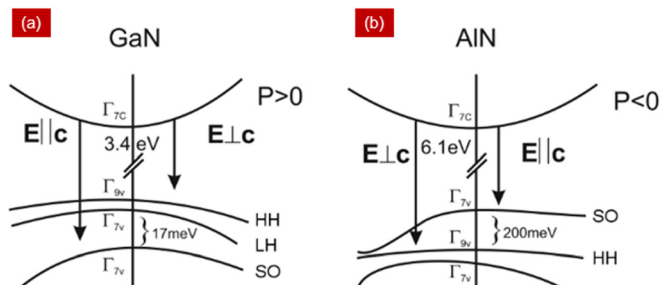
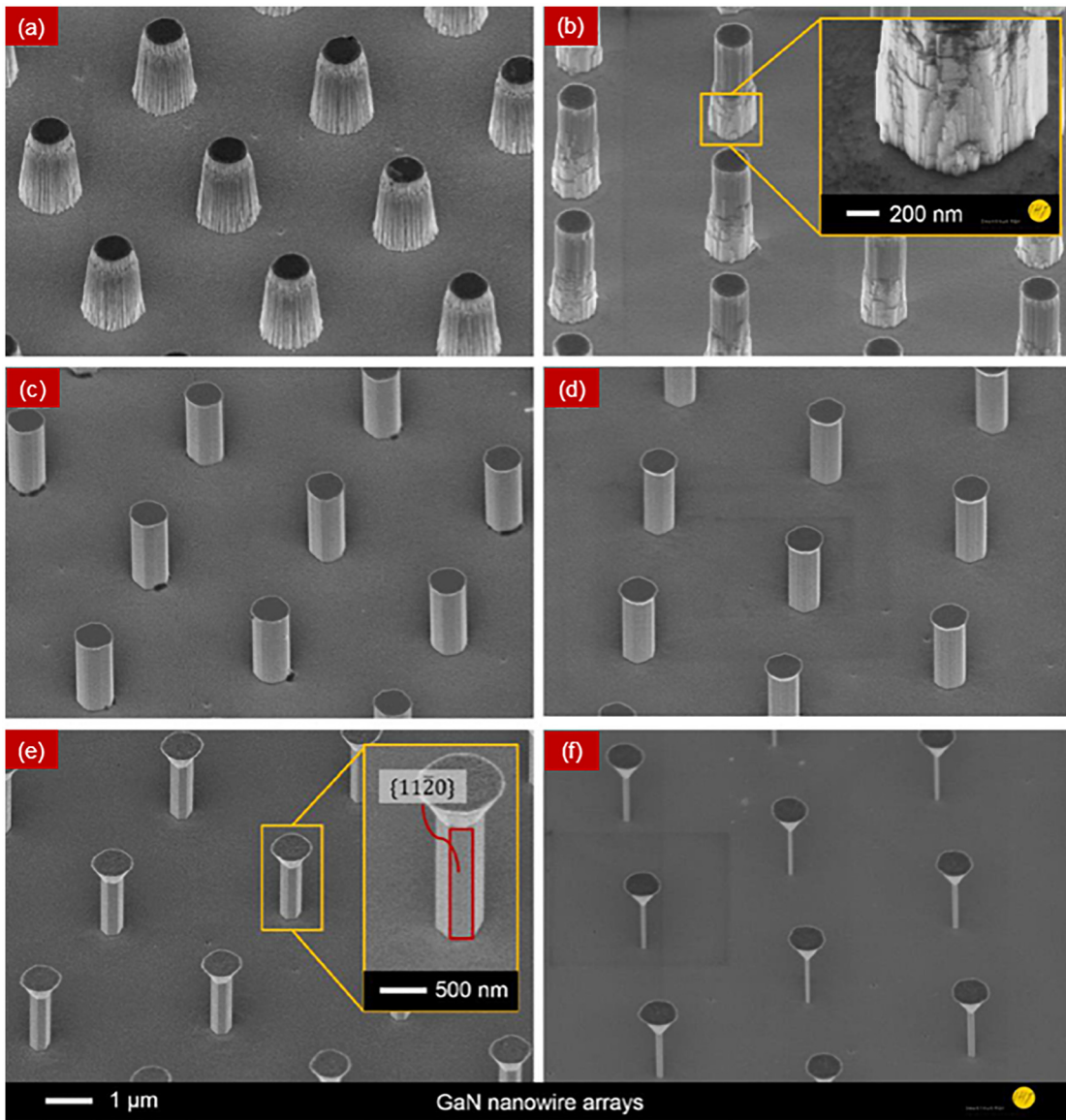


FIG. 6. Conduction band and valence band sequence in (a) GaN and (b) AlN, indicating a change of polarization. From Rass and Lobo-Ploch, *III-Nitride Ultraviolet Emitters*. Copyright 2016 Springer Nature. Reprinted with permission from Springer Nature.<sup>113</sup>



**FIG. 7.** 45°-tilted SEM images of GaN nanowire arrays after (a) ICP RIE followed by wet chemical etching for (b) 20 min, (c) 1 h, (d) 2 h, (e) 4 h, and (f) 6 h at 90 °C, respectively. All samples used in wet etching are with a metal mask on top. Insets are images of feature crystallographic textures with large magnification. Reprinted with permission from Yu *et al.*, Nanotechnology **28**(9), 095206 (2017). Copyright 2017 IOP Publishing.

researchers to combine the advantages in structure homogeneity and material quality.<sup>6,8,14,119,128,131–134</sup> Li *et al.* reported the fabrication of nontapered GaN nanowires by employing hybrid etching to achieve single-mode lasing with a linewidth of ~0.12 nm and a side-mode suppression ratio of >18 dB.<sup>134</sup> This has demonstrated that the hybrid-etched GaN nanowires can have a precise control in dimension as well as a high material quality for enhancing gain. Hybrid-etched GaN nanostructures were later successfully applied in power and high-frequency electronic applications.<sup>7,14,15,119,133,135</sup> In 2015, Jo *et al.* produced vertical GaN nanowire FET using SiO<sub>2</sub> and 5% tetramethylammonium hydroxide (TMAH) as the etch mask and solution,

respectively.<sup>135</sup> Next, Yu *et al.* reported vertical nano-FET based on hybrid-etched GaN nanowires using Cr and AZ400K developer (KOH-based solution) as the etching mask and etching solution, respectively. They obtained regular GaN nanowire arrays with diameters down to 50 nm and smooth hexagonal sidewalls, which were confirmed to be *a*-plane oriented sidewalls [see Figs. 7(e) and 7(f)].<sup>14,119</sup> By changing the etching solution concentrations, *m*-plane sidewalls can however also be obtained. Im *et al.* performed the hybrid etching of lateral GaN nanowires on GaN-on-insulator wafers by wet etching on ICP-patterned strips in 2016, where 5% TMAH solution was used in their case and triangle-shaped nanowires could be achieved.<sup>133</sup>

Following the success of the hybrid etching technique for 3D GaN nanowires, in 2017, Sun *et al.* have transferred this approach for building GaN nanofin or nanowall structures from a GaN bulk substrate using TMAH treatment.<sup>15</sup> This has shown the high flexibility and reproducibility of this top-down approach for creating any type of structures that are defined by lithography. The fins with both *a*- and *m*-plane sidewalls have been fabricated in their work, where the latter sidewall orientation presented smoother surface morphology. They have not only investigated the etching effect on GaN fins, but also successfully demonstrated a vertical GaN nanofin FET for power electronics with high breakdown voltage.

As mentioned before, the main advantage of this top-down approach in comparison to bottom-up technique is the flexibility in composition and doping along the *c*-axis of the micro- and nanorods. Both the composition and doping are controlled by the original parent material and its original thin film sequence. Here, well-established planar growth processes can be utilized. This has, e.g., successfully been implemented in the development of vertical nano-FETs based on n-p-n transitions inside the nanorod.<sup>7</sup> In the same way, micro- and nano-LEDs with an almost arbitrary internal structure can be fabricated.

Nevertheless, there are still challenges in device processing, which are generally related to the 3D nature of the micro-/nanostructures. Chip processing has to be transferred from a conventional planar technology into technology for processing of 3D micro-/nanostructures with a high aspect ratio. For example, in both nano-LEDs and nano-FETs, top and bottom contacts have to be fabricated. The bottom contact is quite straightforward, since the nanostructures are most often directly located on a buffer layer with high conductivity. For the top contact, however, a filling process is necessary in order to allow top metallization with subsequent photolithographic patterning (see Fig.

**8**). The filling of the open volume between high-aspect-ratio nanostructures fulfills two requirements. First of all, the sidewalls of the nanostructures have to be safely covered, so that they are not electrically short-circuiting the active device after metallization. Second, the filling has to leave the top part of the nanostructure open for metallization. Hence, good top contacts can be realized. Whereas in planar technology, a photolithography step with subsequent opening of contact pads is a standard process, which is challenging for 3D devices. It is difficult to control the original thickness of a photoresist spinning process in order to fulfill both requirements at the same time. Therefore, the first spinning process will need to cover the overall field of nano-LEDs, making a subsequent back-etching necessary. This back-etching process of the photoresist (or any other filling material) has to be well controlled to keep only the top part of the nanorods free of resist. Again, etch depth control is possible in planar geometries due to self-limiting etching procedures. For 3D geometries, however, the photoresist will not be completely flat, and these undulations caused by the 3D character of the underlying GaN structures might lead to open sidewalls after back-etching. One has to make sure that these open sidewalls do not cause a problem during later metallization. In nano-LEDs, for example, the active quantum well inside the p-n-junction is only a few 100 nm below the surface of the device, which imposes quite narrow limitations on the back-etching process. Much more details of this 3D processing of GaN nanowires are described in the publications of Feng *et al.*<sup>7,14,119</sup>

The described chip processes are more and more challenging as the lateral dimensions decrease and hence the aspect ratios increase. Due to its internal structure and the thickness of the original layers, the core part of a nano-LED should have a height of at least a few micrometers, including the cladding, active regions, and contact layers.

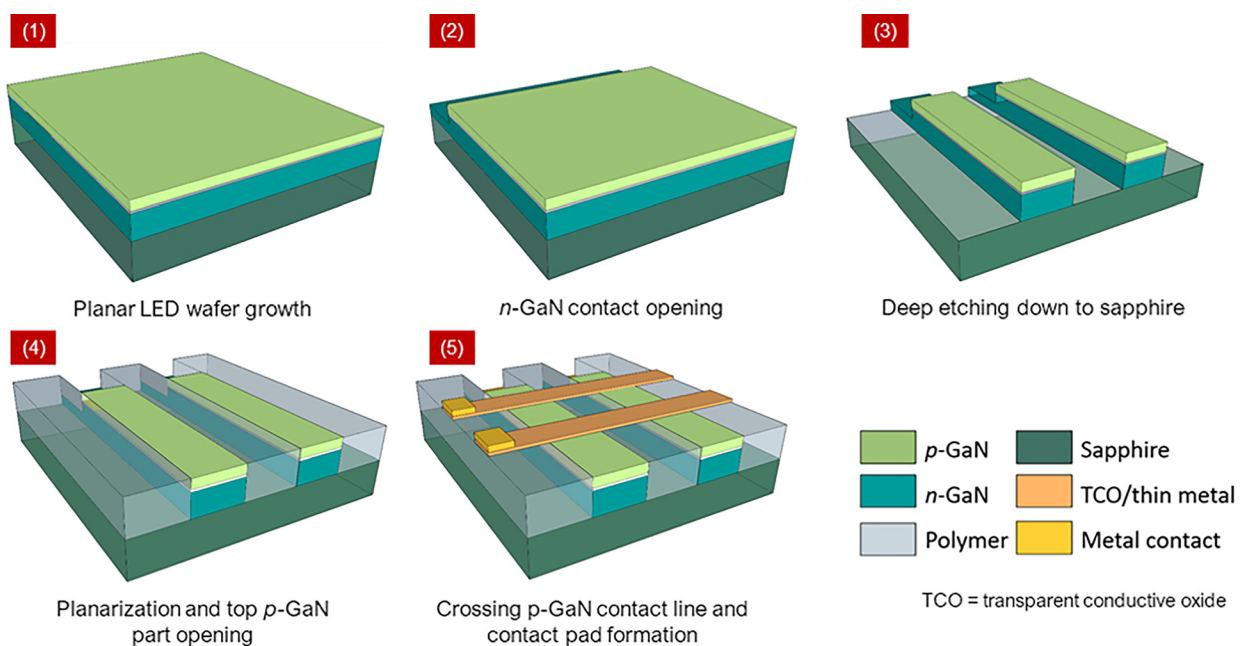


**FIG. 8.** Detailed processing sequence during 3D processing of GaN micro-LEDs. The critical step is the filling of the microstructures, since often very high aspect ratios lead to inhomogeneous distributions of polymers.

Micro-LEDs with dimensions of  $5\ \mu\text{m}$ , which need to be isolated by etching through the whole GaN buffer layer, therefore already approach aspect ratios of 1 and above.

One of the fundamental properties of LEDs is the fact that they are emitting monochromatic light. The wavelength is given by the bandgap of the active region. In many applications, however, polychromatic or full color emission is a requirement. Strategies of using nano-LEDs with different diameters, leading to a variation of indium incorporation, have been suggested.<sup>107</sup> During 3D growth of InGaN, the geometry of the 3D structure directly influences the kinetics of growth, including the Indium incorporation. This would allow to fabricate wavelength distributions on the chips, which can arbitrarily be chosen by the initial patterning of the mask used for selective area growth. Even though a lot of effort has been devoted in this direction, the degree of control is still quite limited.

Another approach might promise to be more feasible. A blue emitting micro-LED array can be converted into a full color microdisplay by adding phosphors, which convert blue light into green and red light. These phosphors need to be added with a spatial resolution similar to the pixel pitch of the micro-LED array, which is a challenge particularly for very small micro-LEDs. Since the downconversion efficiencies above 90% have been reported, this approach seems to be very promising.<sup>136</sup>

#### D. Laser micromachining and lift-off processing of GaN LEDs

Today, all high power LEDs rely on a “thin film design,” where the nitride LED-layers are removed from the original sapphire substrate and transferred onto a second carrier substrate (see Fig. 9). This carrier substrate, often a metal coated silicon wafer, increases the photon outcoupling dramatically, since the metal layer leads to a high reflectivity, which is reducing photon reabsorption intensely. At the same time, the carrier substrate fulfills additional requirements for high power LEDs: high electrical conductivity, thermal conductivity, and stability. The introduction of “thin film LED” has been a major breakthrough in pushing GaN LED efficiency toward its limits.<sup>137,138</sup> Removing an InGaN/GaN layer stack from its sapphire substrate is

realized by a process so-called “laser lift-off,” which has been developed in early 2000s (see Fig. 9).<sup>139,140</sup> The sapphire/nitride stack is hit by the beam of a high power excimer laser from the backside. The laser light is transmitted through the substrate and absorbed at the GaN/Sapphire interface. There, the high intensity leads to a dissociation of the GaN into gallium and nitrogen. Since gallium is liquid under these conditions, the nitride stack can subsequently be removed from its sapphire substrate and be transferred onto a second carrier, as indicated in Fig. 9.

The laser lift-off process used today is based on expensive excimer laser systems. The emission of these systems at a wavelength of usually 193–355 nm is absorbed in GaN, but not in sapphire.<sup>139,141–143</sup> However, the energy of the photons is not high enough to be absorbed in AlN. AlN buffer layers need to be used to grow high quality buffers for UV LEDs. The transfer of the well-known laser-lift-off process to UV LED technology is still an open question. A potential alternative is the usage of femtosecond laser pulses. Here, the absorption is due to multiphoton-processes, which also lead to efficient absorption when the photon energy is below the bandgap of the semiconductor to be processed (like AlN in this case). First experiments are presently on the way to explore the potential of this alternative approach to laser lift-off for creating free-standing nitride films.<sup>144,145</sup> Another ingredient for efficient light outcoupling is the roughening of the top *p*-GaN surface that can lead to a beneficial and arbitrary distribution of photon paths, which finally—in combination with highly reflective backside mirrors—result in very high outcoupling efficiencies of above 90%.<sup>146</sup>

#### E. Hybrid integration of GaN micro-LEDs with Si CMOS electronics

Removing a thin nitride LED stack from its original sapphire substrate is not only a powerful technique for putting LED thin films on highly reflective carriers and by that optimizing light outcoupling. Since the impact of the laser takes place at the sapphire-GaN interface only, leading to the dissociation of GaN, this process is a high temperature process, but only at the particular point where the laser is hitting the sample, leading to a very local impact only. Overall, for the rest of the wafer, it is a low temperature process step. This has important

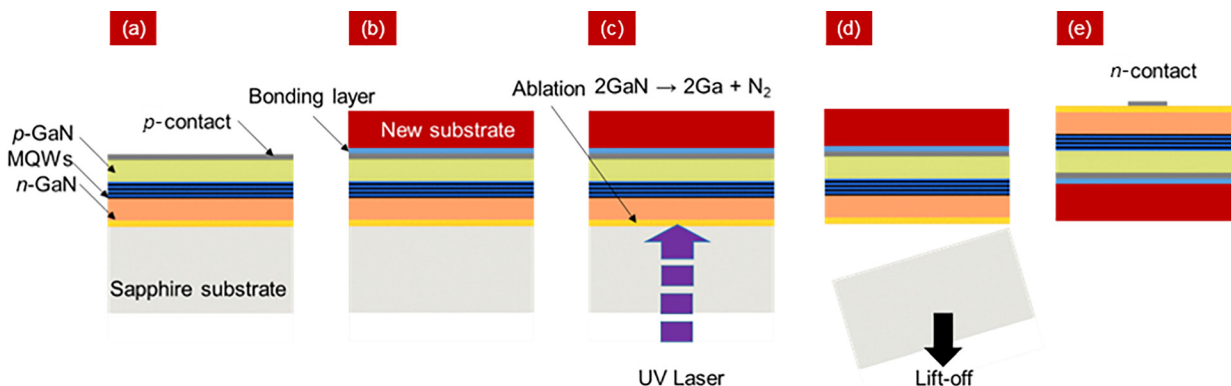


**FIG. 9.** Sequence of single steps during a laser lift-off process. (a) Original LED structures on a sapphire substrate, with *p*-contact on top. (b) Original wafer is bonded face-to-face to a new carrier, often with a mirror with high reflectivity in between. (c) The GaN-sapphire interface is exposed to strong UV laser irradiation, which leads to a disruptive dissociation of the GaN material in the interface region, leaving metallic gallium behind. (d) After that, the original sapphire wafer can be removed. The former interface region is now the new surface of the overall structure. The existing roughness is supporting light extraction. (e) Finally, an *n*-contact is made.

consequences, since laser lift-off can be used to transfer GaN thin films onto polymer carriers (in order to introduce mechanical flexibility, as discussed later), or onto processed silicon wafers, where the impact of the laser lift-off is sufficiently low to guarantee the stability of micro-electronic circuits on the silicon wafer. This opens up amazing possibilities and is believed to be one of the core technology drivers in the near future. As a result, laser lift-off would allow to combine photonic with microelectronic functionality in a fully hybrid approach. The silicon wafer can be processed first, making use of global foundry services having full access to silicon technology, and then, it can be connected by laser lift-off to GaN thin films adding photonic functionality. Subsequently, the GaN/silicon stack can then be processed in order to achieve GaN devices of choice.

This hybrid combination of GaN micro-LEDs with silicon CMOS technology is interesting in two directions. First, the CMOS chip can be used as a control device for the micro-LED device, e.g., offering intelligent connection and driving units to a micro-LED array. Second, GaN micro-LEDs can be used as light engines on a silicon CMOS wafer, e.g., toward optical communication. The wafer transfer technique with a subsequent lithography fully outperforms conventional pick-and-place assembly of discrete optical components, like laser diodes. GaN micro-LEDs can be modulated at gigahertz frequencies,<sup>94</sup> being combined with waveguides on wafer,<sup>147</sup> and by that have the potential to be at the root of a future hybrid photonic-microelectronic integration.<sup>148</sup> It should also be mentioned that miniaturization of LEDs in the GaN material system is much less critical in comparison to conventional III-V semiconductors due to much longer surface recombination time in GaN.<sup>149</sup>

#### F. Transfer of GaN micro- and nano-LEDs onto flexible substrates

Besides planar and 3D micro-/nano-LEDs that are grown on the original substrates or placed on solid substrates, nowadays an intense and extensive research has been performed to realize flexible inorganic LEDs using various approaches (e.g., polymer embedment, printing, flip-chip, and lift-off).<sup>150</sup> This is due to a fact that flexible LEDs have offered several novel functionalities and possessed unconventional opportunities to open up a new path toward other applications that cannot be covered by conventional rigid LEDs (e.g., foldable and deformable light sources,<sup>151</sup> wearable light on fabrics,<sup>152</sup> paper LED displays,<sup>153</sup> large-scale flexible displays,<sup>154</sup> or smart tactile sensing devices for robotics and human-machine interfaces.<sup>155</sup> Moreover, because of their simple processing, low material cost, high flexibility, various available substrates, promising performance, and possible large-scale production, flexible LED displays will certainly find large future markets.

In the last decades, the key technology for flexible optoelectronics has been organic LEDs (OLEDs).<sup>156</sup> However, the OLEDs have suffered from several issues related to device instabilities (e.g., caused by temperature variation, oxidation, aging, diffusion or mixture of the stacked organic layers, and recrystallization), which may degrade the conductivity and optoelectrical properties of the LED affecting the performance of the whole optoelectronic systems. Therefore, alternative materials based on inorganic III-V compound semiconductor materials with wideband gaps (e.g., GaAs, GaN, and AlInGaP) have been introduced to be integrated on the flexible substrates. Printing of GaAs micro-LEDs on a polyethylene terephthalate (PET) substrate has been

demonstrated by the group of Rogers.<sup>157,158</sup> Another type of flexible GaAs red LED array with noncoplanar serpentine bridges has been used in biosystems, clinical medicine, and robotics,<sup>158</sup> which can cover large areas on various surfaces with high flexibility. As a proof-of-concept measurement, monitoring of glucose concentration has been demonstrated by measuring the variation of transmitted light intensities using a photodiode. However, although GaAs LEDs are favorably used in biological sensing, they emit only red and infrared (IR) light due to their narrow wavelength range (630–700 nm), which consequently limits their further possible applications. Thus, GaN with its potential to cover the green to UV spectral range will massively enter these applications for micro-LEDs on flexible substrates in the future. Recent reviews related to the flexible GaN micro-/nano-LEDs can be found in Ref. 159.

### III. GaN LED APPLICATIONS BEYOND SOLID-STATE LIGHTING

In this section, some applications of the GaN LED devices that have been previously described in detail in terms of their fabrication and processing are shown.

#### A. High-brightness micro-LED displays

##### 1. Micro-LED displays for augmented reality (AR)

Until now, GaN technology has not been assumed to be a viable technology for displays. The display market is governed by liquid crystal display (LCD) and OLED technology, mainly due to cost considerations. As GaN technology follows a strict and successful cost reduction strategy over the past years, this perception meanwhile has completely been changed. Modular large area displays made of GaN micro-LEDs are meanwhile commercialized,<sup>160</sup> drawing from their major advantages in comparison to LCD and OLED:<sup>161,162</sup> highest brightness, contrast, efficiency, and modulation frequencies. These “micro-LED” displays, though, are using LEDs in the 50–100  $\mu\text{m}$  range. As there is still room for improvement moving toward even smaller LEDs, micro-LED displays are likely to enter a huge market served by GaN technology.<sup>19,107,163</sup>

Besides virtual reality (VR) systems, augmented reality (AR) systems are of increasing interest, as they combine the real-world images with artificial ones in real time using, e.g., glasses with displays. For such smart eyewear, the advantages of a GaN technology are even more striking, making GaN micro-LEDs by far the desired technology. In these AR applications, full resolution displays are supposed to have micro-LEDs with sizes in the 10–50  $\mu\text{m}$  range, since in order to display information into AR glasses, a very compact projection display is needed. The core requirements for a microdisplay are: smallest possible size (for best integration into glasses), highest possible brightness (even when in the micrometer range, for operation at daylight with smallest displays), being most efficient (for long battery lifetime), and have highest lifetime (since it will be operating continuously). For each single requirement, GaN-based displays are by far superior to OLED or LCD displays. This is the reason why innovative companies active in the field of augmented reality worldwide meanwhile are deeply involved into micro-LED development (e.g., Apple, Google, and Plessey Semiconductors partnering with Vuzix).

## 2. Nano-LED arrays for super resolution microscopy

For displays, there is no reason to reduce the pixel size of micro-LED arrays further down, possibly even below the optical resolution limit. On the one hand, all foreseen applications involve in one way or another the human vision, which has some evident limits concerning the smallest objects that can be seen by the naked eye (of about several tens of micrometers in the most favorable conditions<sup>164–167</sup>). Therefore, pixel resolutions in the range of a micrometer or less have remained fully unexplored. On the other hand, light intensity will be reduced with the pixel size, which is another argument against further miniaturization. The high brightness of inorganic GaN LEDs compared to their OLED counterparts—makes them a good technological choice if size reduction is attempted.

As discussed in Secs. II B and II C, there is no technological impediment to achieve today GaN LED emitters of nanometric sizes, and to arrange them in a 2D array configuration with pixel to pixel distances in the nanoscale [see Fig. 10(a)]. From a broad perspective, these nano-LED arrays would provide experimentalists a new tool: a set of almost ideal point light sources, which can be located in space with nanometric precision, without the need for any optical or mechanical system. This way the origin of the light emission could be

shifting from one nano-LED to another in a fully repeatable and accurate way, only switching one LED after the other. From a fundamental point of view, this will give access to light source displacements well below the diffraction limits (around 200 nm for light in the visible range) [see Figs. 10(b)–10(d)].

Among other applications, new strategies to improve optical resolution, based on ideas that remained dormant for years,<sup>168</sup> can now be implemented [see Fig. 10(d)]. The array can be scanned, switching on and off one single nano-LED at a time, separately and at a high rate.<sup>25</sup> In combination with a light detector, a signal related to light matter interactions occurring in the vicinity of each one of the nano-LEDs positions could be recorded. Thus, the photodetector signal in time could be transferred into a real space transmission image showing the “transmission” image of the object under investigation, placed right over the nano-LED array. In contrast to conventional microscopy, spatial resolution would be provided by the illumination source, and not by the optical detection system. Hence, the optical detection system would not require particular alignments, optical focusing systems or spatially resolved detectors, as spatial resolution will solely be limited by the distance between two neighboring nano-LEDs. Current estimations suggest that pixel-to-pixel distances in the range of 50 nm can be at reach with existing technologies.

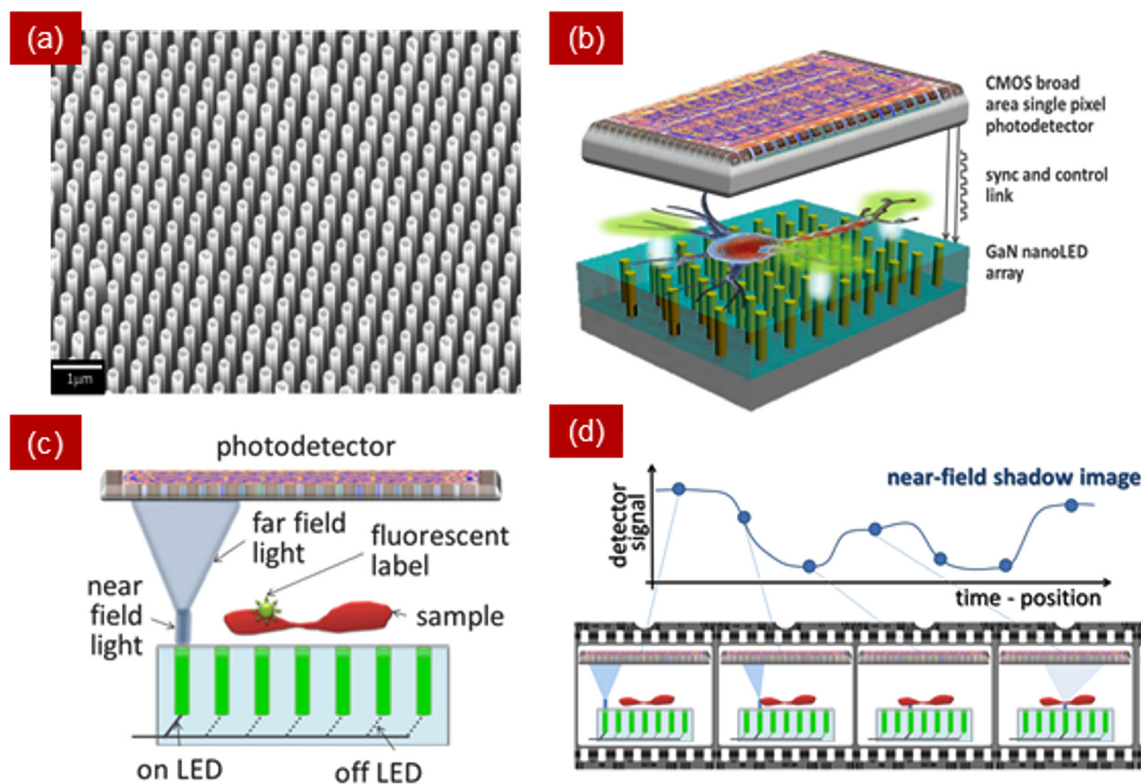


**FIG. 10.** (a) Array of InGaN 3D nano-LEDs. Each one of the nanorods contains one fully functional LED element, which can be activated as an independent point light source. Current technology makes it feasible achieving pitches between nano-LEDs of a few hundred nanometers. This means that independent point light sources with a spacing below the wavelength of the emitted light are at reach. (b) One possible application of this extremely dense nano-LED array is direct optical microscopy, without lenses, in combination with a broad area light detector, located in front and close to the nano-LED array. (c) and (d) Such a system can produce direct shadow images, by scanning the sample with one nano-LED pixel after the other, and monitoring the intensity through the sample, which means approaching the typical wavelengths of the light emitted. This approach opens the door to a new kind of highly miniaturized, high resolution microscope.

All this renders a new path toward what is known as superresolution microscopy, a set of microscopy techniques like stimulated emission depletion microscopy (STED), stochastic optical reconstruction microscopy (STORM), photoactivated localization microscopy (PALM), near-field scanning optical microscopy (NSOM), and structured illumination microscopy (SIM),<sup>169–171</sup> in which all those methods are based on bulky optical systems and complex sample preparations that allow for acquiring optical images with a spatial resolution beyond limits imposed by the diffraction of light.

## B. Visible light communication (VLC)

A discussion, which is ongoing for many years, is whether white LEDs—in addition to solid-state lighting—can also be used for optical communication. VLC describes an optical and wireless communication system that transmits information by modulating light in the visible spectrum (380 nm–780 nm). VLC would have the advantage that the information can safely be kept inside a room by physical reasons—by only blocking the windows or closing the doors. Walls are transparent to visible light, in contrast to WiFi radiation. When moving into the UV, exploiting the strong scattering of UV light, non-line-of-sight communication is another version of using modulated LEDs or laser diodes for communication. These high-frequency modulation schemes are not visible to the human eye, but can be detected by, e.g., smartphones and further internet of things (IoT)-based devices equipped with a detector in line of sight to the emitting LEDs.<sup>172</sup> The possibility and attractiveness to integrate such VLC systems into the world of lighting infrastructure are directly coupled to the uprising of LED technology in the last two centuries, as incandescent or fluorescence light bulbs cannot be modulated quickly, and are well driven by the demand for an ubiquitous but safe connection of smart devices. The advantages of VLC are the license-free operation,<sup>24</sup> the high spatial confinement to one room and therefore offering physical layer security,<sup>173</sup> and the possibility to supplement the RF data spectrum while possible even integrating the VLC systems into existing lighting solutions.<sup>174</sup> In particular, the micro-LED technology offers some advantages over conventional solid-state lighting solutions in terms of VLC performance, in particular concerning speed of operation.

### 1. Structure of the VLC system

A viable VLC system is based on three parts: transmitter, channel, and receiver.<sup>174</sup> The transmitter side includes the driver electronics to control the triggering of the optical emitter according to the input data. The illumination may be shaped by optics in front of the light source. The channel can either be a free space one (e.g., air) or based on waveguides. The receiver transduces the received optical intensities

to the electrical output data. Therefore, optical receivers with a high bandwidth and adequate optics and an amplifier circuit are required. A schematic of the described system is shown in Fig. 11.

In this paper, only the most frequent systems with a free space channel and commonly available detectors are considered. Hereby, one light source can be detected by one detector (single input single output) or multiple light sources (e.g., micro-LED arrays) can be detected by multiple detectors (multiple input multiple output). The light source can be modulated via different modulation schemes as described in detail in Refs. 174–176.

The main requirement for a high-speed data VLC system is a high bandwidth throughout all parts of the system. Detectors based on charge-coupled device (CCD) or CMOS image sensors can be used on the receiver side. However, these sensors are designed for a low number of frames per second and achieve data rates in the kbit/s range.<sup>177</sup> Photodiodes such as silicon PIN photodiodes or avalanche photodiodes (APDs) reach data rates up to 1 Gbps (Refs. 178 and 179) and are therefore more suitable for high-speed data communications.

### 2. Micro-LEDs as an emitter in the VLC system

Commercially available GaN-based LEDs with the main purpose of solid-state lighting usually have chip sizes of 200 μm and above and are coated with a phosphor to convert the blue bandgap emission from the LED to an overall white light emission. Those off-the-shelf LEDs have modest modulation bandwidths of 10–20 MHz,<sup>24</sup> while their VLC performance is limited by the aforementioned properties.<sup>180</sup>

Micro-LEDs exhibit several characteristics, which make them more suitable for VLC applications. At first, a smaller LED size leads in general to lower RC constants, which contribute to a higher modulation capability of the transmitter.<sup>181</sup> A smaller LED footprint also allows for higher current densities during operation, which reduces the carrier lifetime in the active area and therefore offers a higher modulation frequency.<sup>182</sup> The modulation bandwidth therefore strongly depends on the injected current density. Moreover, the carrier lifetime can be reduced further by the employment of nonpolar or semipolar-based micro-LEDs instead of usual c-plane micro-LEDs. This is due to the larger electron-hole wavefunction overlap of non-/semipolar LEDs in comparison to c-plane LEDs and the effect is especially pronounced at lower current densities.<sup>93</sup>

Table II shows the performance comparisons of GaN micro-LEDs with other technologies based on nanowire LEDs and laser diodes for VLC applications. In terms of the micro-LED-based VLC system, the highest data rate of 7 Gbit/s has been achieved by Rajbandari *et al.*<sup>183</sup> using a 6 × 6 micro-LED array with a diameter of

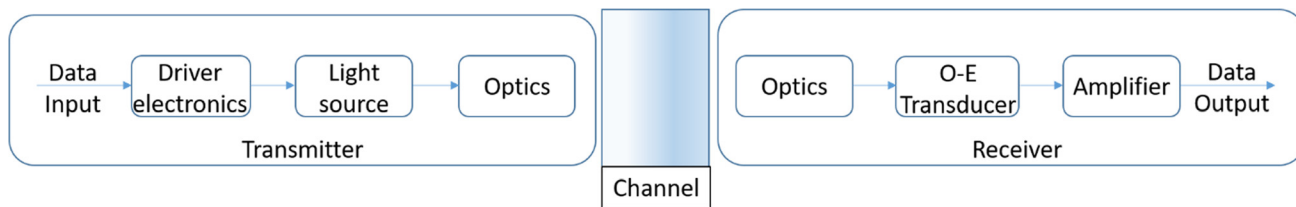


FIG. 11. Visible light communication (VLC) system consisting of the transmitter, channel, and receiver.

**TABLE II.** Performance comparison of GaN micro-LED technology with other devices (i.e., nanowire LED and laser) used for visible light communication (VLC). PAM, pulse-amplitude modulation; OFDM, orthogonal frequency division multiplexing modulation; OOK, on-off key modulation.

Light source	Device property	Modulation type	Bandwidth	Data rate	Year (Reference)
GaN micro-LED	Array = $6 \times 6$ ; diameter = $39 \mu\text{m}$ ; color = blue (450 nm)	PAM	140 MHz	7 Gbit/s	2017 (Ref. 183)
GaN micro-LED	Diameter = $20 \mu\text{m}$ ; color = blue (450 nm)	PAM	450 MHz	2 Gbit/s	2016 (Ref. 184)
GaN micro-LED	Diameter = $24$ and $42 \mu\text{m}$ ; color = blue (450 nm)	OFDM	800 MHz	5 Gbit/s	2016 (Ref. 24)
GaN micro-LED	Diameter = $24$ and $42 \mu\text{m}$ ; color = blue (450 nm)	PAM	800 MHz	3.5 Gbit/s	2016 (Ref. 24)
GaN micro-LED	Diameter = $84 \mu\text{m}$ ; color = blue (450 nm)	OFDM	400 MHz	3 Gbit/s	2014 (Ref. 22)
GaN micro-LED with polymer color converter	Diameter = $50 \mu\text{m}$ ; color = white after light conversion	OFDM	531 MHz	1.68 Gbit/s	2014 (Ref. 185)
GaN micro-LED	Diameter = $99 \mu\text{m}$ ; color = blue (450 nm)	OOK	150 MHz	1.5 Gbit/s	2013 (Ref. 186)
GaN micro-LED	Array = $16 \times 16$ ; diameter = $72 \mu\text{m}$ ; color = blue (450 nm)	OOK	245 MHz	1 Gbit/s	2010 (Ref. 23)
GaN nanowire LED	Diameter = $400 \text{ nm} - 1.5 \mu\text{m}$ ; length = $15 \mu\text{m}$ ; density = $1.10 \text{ wire}/\mu\text{m}^2$ ; color = blue (448 nm)	OOK	...	1 Gbit/s	2015 (Ref. 94)
GaN laser diode	Type = OSRAM optosemiconductors, PL 450B; spectral linewidth = $0.67 \text{ nm}$ ; color = blue (450 nm)	OFDM	1.5 GHz	9 Gbit/s	2015 (Ref. 187)
GaN laser diode with a remote phosphor	Type = OSRAM optosemiconductors, PL 450B; color = white after light conversion	OFDM	1.3 GHz	5.2 Gbit/s	2015 (Ref. 188)
GaN laser diode with a remote phosphor	Type = Thorlabs, LP450-SF-15; color = white after light conversion	OFDM	1 GHz	4 Gbit/s	2015 (Ref. 189)

$39 \mu\text{m}$  and an emitted blue wavelength of 450 nm. The obtained bandwidths of micro-LEDs in VLC are ranging from 140 to 800 MHz. Using commercial blue GaN laser diodes, the systems can result in higher bandwidths (1–1.5 GHz) and data rates (4–9 Gbit/s) than those employing micro-LEDs.<sup>187–189</sup> In such a system, a remote phosphor is normally used to realize white light communication. For modulation, several schemes have been employed, i.e., pulse-amplitude modulation (PAM), orthogonal frequency division multiplexing modulation (OFDM), and on-off key modulation (OOK). More devices other than micro-LEDs, nanowire LEDs, and lasers were also introduced for VLC (e.g., commercial white LED and RGB LED), in which deeper discussion for all the demonstrated VLC systems for the last decade can be found in another review paper.<sup>174</sup>

Several multi-Gbit/s VLC data link rates based on micro-LEDs have been realized by the adoption of different modulation and equalization schemes and are described in Refs. 22, 24, and 190. It should be mentioned, however, that the integration of lighting systems and VLC systems can also be viewed as being critical. Lighting systems are often switched off, whereas VLC systems should be available continuously. In addition, specialized electronics will be necessary, and it is unlikely that lighting housing will regularly be equipped with this. Nevertheless, VLC is being viewed as an interesting approach for future industry 4.0 and smart home environments, but it is more likely that separate specialized units will be developed for this. Micro-LEDs have an advantage concerning modulation speed. On the other side, intensities are becoming a critical issue when larger distances and light sources with a broad spatial emission are to be used. In view of the rather broad emission of LEDs in comparison to laser diodes, multi-wavelength transmission will certainly remain to be a challenge for the next years.

### C. Biomedical sensors and imaging systems

GaN micro-LEDs and nano-LEDs with various wavelengths from UV to visible ranges have been implemented in different types of biomedical sensors and imaging systems. The micro-LED chips need to be combined with sensitive photodetectors [e.g., CMOS camera and single-photon avalanche diode (SPAD)] and other supporting elements (e.g., microfluidics, 3D-printed housings, driver circuits, and reconstruction software), ideally in a fully integrated architecture. Lensless mini microscopes, optoelectronic tweezers, and fluorescence-based sensors have attracted immense attention from the biological and biomedical research communities, in which they are used in different biological targets (e.g., microparticles, cells, neurons, and molecules). In the last few years, the demands on the biosensors have moved toward portable or wearable low-cost instruments that can be employed as personal sensors to be used out of the labs. During miniaturization and cost reduction processes, the performance (e.g., sensitivity or imaging resolution) is not to be sacrificed. This has been made possible with the development of advanced microfabrication processes enabling on-chip biosensors and imaging systems.

For all types of developed biomedical sensors, the integration of micro-/nano-LEDs as a light source can either provide additional new function or improve the existing feature of the optical sensing systems. By scaling the LEDs down to micro-/nanosized structures, high-spatial-resolution sensors will be made feasible targeting only on specific objects (e.g., bioparticles, proteins, or neurons) at specific locations, without affecting other parts of object systems. This is, for example, very important for optogenetics where in most cases localized illumination is needed at a very small area, so that other parts of nontargeted neurons will not be influenced, in which fluorescence-based

measurements are normally carried out. Moreover, in combination with MEMS for *in vivo* investigation inside the body, the hybrid-joined optogenetic devices should be made as small as possible to have less or noninvasive measurements. This is, of course, not possible when conventional large LEDs are used, as the emitted light from these types of devices will illuminate the whole object system, leading to unwanted biological mechanisms. Moreover, by having smaller dimensions, the required power to activate the LED-based sensor will dramatically shrink resulting in ultimate low-power sensors. Hybrid integration of micro-LEDs with a CMOS-based electronic driving circuit and image detector can be also realized to produce very compact chip-based optical sensors or microscopes. In this case, highly efficient optical sensors are expected, as the droop efficiency can be reduced and overall light outcoupling efficiency (EQE) can be maintained at a high value for micro-/nano-LEDs. For a holographic lensless mini microscope, the use of an integrated InGaN micro-LED can be an alternative for the conventional setup of already established microscopes, where surface-mounted LEDs (SMD LEDs) are normally coupled with an optical fiber or pinhole element to create such a point light source, so that the device can be made more compact and the photon loss in the whole system can be reduced. Additionally, higher modulation speed and bandwidth of micro-LEDs (up to G) open a new route to realize fast optical sensors used for the detection of single flowing bioparticles inside a microfluidic chip. However, the current challenges are still the realization of individually addressable nano-LED arrays and their joining and packaging technique as well as the improvement of light outcoupling of such devices.

### 1. Compact lensless microscopes

Recently, LED arrays have been used as a light source in various configurations of LED-based imaging systems,<sup>191–200</sup> which subsequently have been considered as a versatile platform for computational microscopy.<sup>201</sup> Several types of LEDs with different wavelengths have been reported, where mostly red-green-blue LEDs (RGB LEDs) are employed<sup>191</sup> for biological applications. In LED array-based microscopes, the addressable LEDs are positioned in the source plane of a microscope to realize various label-free imaging modes by controlling the illumination toward the sample. Multicontrast imaging (i.e., bright-field, dark-field, and differential phase contrast<sup>191,196,197</sup>) and Fourier ptychographic-based high-resolution imaging with a large field of view have also been demonstrated using LED array platforms. However, those microscopes are still bulky because they are equipped with complex optics limiting their usage in other applications, where mobility, harsh environments, and quick analysis become important factors. Therefore, some researchers have attempted to develop LED-based mobile microscopes by assembling available optical and electronic components into low-cost lightweight microscopes [Fig. 12(a)]. It has been a trend to integrate mobile microscopes with smartphones. Those smartphone-based devices can exhibit an imaging quality similar to that produced by more expensive high-quality benchtop microscopes.<sup>202–204</sup> LED light, given appropriate source dimensions and optical bandwidth, can be utilized as a spatially coherent light source for coherent imaging techniques.<sup>205,206</sup> Furthermore, the possibility of utilizing multicolored RGB LEDs as a multiwavelength source does not only add the ability to obtain color images,<sup>207</sup> but also offers the possibility to reconstruct the phase information in dense samples.<sup>192</sup>

Among other microscopy methods, digital inline-holography provides a promising way of using micro-LED arrays as a spatially coherent light source in combination with an image sensor to build a compact digital microscope [Fig. 12(a)].<sup>208,209</sup> It does not rely on complicated and expensive optical elements such as mirrors and lenses. In lensless holographic microscopy, the recorded spatial information is the interaction of the incident micro-LED emission with the object. The new wave front includes interference between a reference light wave of known properties (i.e., the unperturbed light wave that passes through the transparent sample substrate), and the light wave that has been partly absorbed and scattered by unknown objects or samples placed on the object plane.<sup>201</sup> As a consequence, the intensity is modulated in space and includes interference patterns; with that information, the optical properties of the unknown object can be inferred [Fig. 12(b)] by reconstruction of the wave front in the object plane. Dissimilar to other types of holography, the reference wave used here is “in-line” with the scattered wave generated by the object.<sup>210</sup> Thus, this technique is known as digital in-line-holography. In this microscopy, besides the possibility of creating an inexpensive and robust measuring setup,<sup>211</sup> the opportunity of utilizing the optical phase information leads to new possibilities in sample analysis.<sup>212</sup> The microscope resolution and field of view are practically decoupled from each other and only depend on the spatial resolution of the optical sensor.<sup>213</sup> Therefore, the field of view can be enlarged simply by using sensors with a larger active area. On top of that, the incorporation of multiple illumination angles can be utilized for tomographic 3D reconstruction.<sup>149</sup> The obtained 3D images can reveal sample structures that would be otherwise obscured in microscopic images.

Due to fast device development, such cost-effective LED-based portable or mobile microscopes<sup>203</sup> have been employed in a wide range of biomedical diagnostics, including for investigating schistosomiasis disease (*S. haematobium* and *S. mansoni*),<sup>202</sup> pathogenic bacteria (*Cronobacter* spp.),<sup>214</sup> 3D motion of free-swimming sperm cells,<sup>215</sup> biomolecular interaction of protein A/G with immunoglobulin G (IgG) antibody,<sup>216</sup> flagellated protozoa (*Trypanosoma brucei* spp.),<sup>217</sup> histochemical stains,<sup>218</sup> encapsulated islets,<sup>219</sup> type 2 diabetes mellitus disease (pancreatic islets),<sup>220</sup> mouse astrocyte cells,<sup>221,222</sup> neuroblastoma and prorocentrum minimum cells<sup>223</sup> biofilms,<sup>224</sup> and NIH 3T3 cells.<sup>225</sup> Moreover, accurate holographic color imaging using on-chip lensless microscopes could already be demonstrated using an absorbance spectrum-based colorization technique, which is done by assembling a colored image out of an estimated absorbance spectrum generated by multiple measurements with different wavelengths [Figs. 12(c) and 12(d)].<sup>218</sup> It has been tested to image several pathological samples including tissue samples of liver, kidney, artery, lung, and esophagus. Another simpler technique that can be employed to create holographic color images is a direct RGB combination method, in which the spectral reflectance or transmittance of the sample is discretely sampled at three chosen wavelengths (i.e., RGB) and the colored images are directly composed by taking those measurements as the single RGB color channels. Nevertheless, this method has a drawback in terms of color accuracy with respect to the color perception of the human eye.<sup>226</sup>

Different shapes and configurations of the LEDs have been reported in-state-of-the-art compact microscopes (e.g., ring-shaped LED array,<sup>202</sup> RGB LED array [Fig. 12(e)],<sup>228</sup> fiber-coupled LED array,<sup>227</sup> domed LED array<sup>229</sup>). However, to further increase the

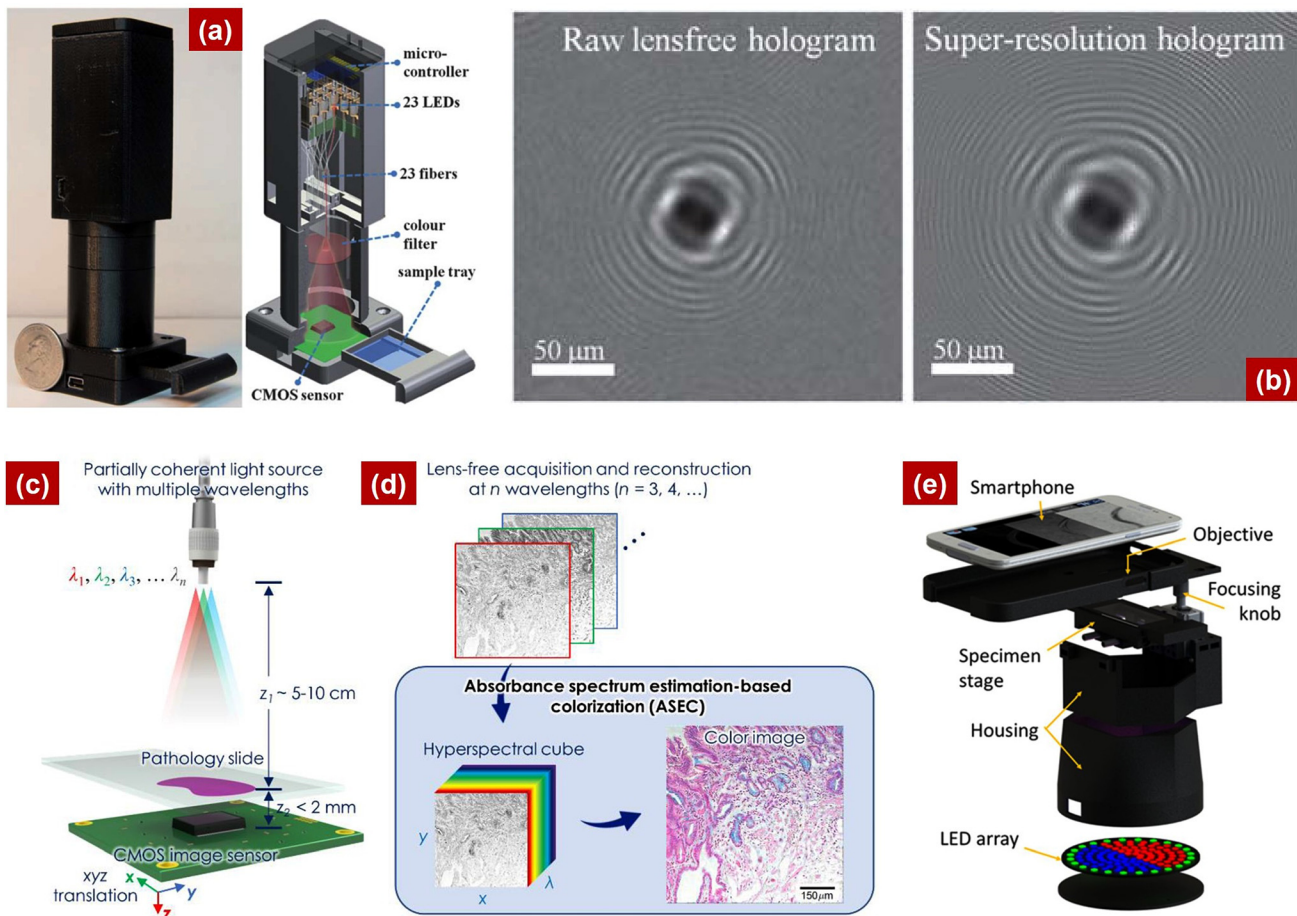


**FIG. 12.** (a) Photograph and schematic diagram of the LED-based lensless super-resolution microscope with a weight of 95 g and 23 fiber-optic-coupled LEDs. (b) A raw holographic image (left) generated by the lensless mini microscope in (a) and higher resolution holographic image (right) after multiple shifted lensless holograms have been processed using a computational pixel super-resolution algorithm. Republished with permission from Bishara *et al.*, *Lab Chip* **11**(7), 1276 (2011).<sup>227</sup> Copyright 2011 Royal Society of Chemistry. (c) Schematic of accurate-color lens-free holographic microscopy based on RGB LEDs and (d) its image acquisition and reconstruction process applying an absorbance spectrum estimation-based colorization method to obtain a color-accurate sample image. Reprinted with permission from Coskun *et al.*, *Sci. Rep.* **4**, 6789 (2014).<sup>216</sup> Copyright 2014 Wiley-VCH Verlag GmbH & Co. KGaA. (e) Configuration of a multicontrast smartphone microscope with color-coded LED illumination patterns. Reproduced with permission from Jung *et al.*, *Sci. Rep.* **7**(1), 7564 (2017).<sup>228</sup> Copyright 2017 Author(s), licensed under a Creative Commons Attribution 4.0 License.

degree of integration and miniaturization, a reduction of LED sizes into micro-LEDs is necessary. GaN micro-LED arrays based on pin-hole structures have been recently reported to be applied in a compact digital in-line holographic microscope for real-time monitoring of cell cultures.<sup>221,230</sup> In comparison with commercially available SMD LEDs, those pinhole-LEDs could enhance the spatial coherence length of the light source and therefore allow for more flexible and compact geometries. If pixels in a micro-LED array can be individually controlled, several captured images from LEDs with different pixel positions can be used to develop a new image with pixel super-resolution. In this case, only the micro-LED module has to be switched, instead of moving the sample, as it is done in a more conventional approach to pixel super-resolution. Using this technique, deep subpixel resolution can be achieved [Fig. 12(b)]. The pixel super-resolution technique was originally proposed for other microscopy approaches where the resolution is pixel-limited.<sup>201</sup> In a conventional pixel super-resolution technique,

a sequence of images is acquired from the same object, where after each successive image, the object is moved across the image sensor by distances equal to a noninteger number of pixels. Subsequently, from the sequence of lower-resolution images, a single higher-resolution image of the observed object can be synthesized. Due to the near one-to-one magnification in LED-based lensless on-chip imaging systems, the obtained resolution of the reconstruction is equal to the resolution of the recorded hologram, so that a high-resolution hologram will yield a high-resolution image of the sample (i.e., so-called “pixel super-resolution”). Nowadays, different techniques to yield higher pixel resolutions have been reported (e.g., using wavelength scanning,<sup>231</sup> color demultiplexing process,<sup>232</sup> machine learning,<sup>233</sup> and deep learning<sup>204,234,235</sup>). The latter method, which is one of the machine learning types, has now become one of the mostly discussed and researched ways to improve the quality of images produced by the holographic microscope, as a matter of fact that the improvement of

microscope hardware (e.g., photodetector) has somehow almost reached its saturation point. Besides, artificial neural networks can be used for, e.g., quantifying moving cells automatically in a lensless microscope.<sup>222</sup> Taking advantage of high-end semiconductor technology, the LED pixel dimension can be further scaled down to a few hundreds of nanometers by means of electron beam lithography (EBL) patterning, in which that EBL processing has already been proven in the fabrication of a nanostructured color filter matrix with the grating period ranging from 360 nm to 640 nm.<sup>236</sup>

Lensfree holographic microscopes can be realized by two chips: the micro-LED array and the photodetector, without lenses or other complex optical components, and can therefore potentially be fabricated very cost efficient. In addition, the produced images will have large space-bandwidth products, can recover the phase of investigated objects, and can reconstruct 3D volumes.<sup>208,236</sup> Finally, it should be emphasized that by employing a CMOS image sensor chip with small pixel size (e.g.,  $\sim 1.1 \mu\text{m}$ )<sup>201</sup> and the computational LED-based lens free imaging technique,<sup>201,237</sup> a higher spatial resolution of up to  $\sim 225 \text{ nm}$  can be obtained. Thus, although the cost and size of the device will be further shrunk down, the quality of the produced images will be kept at very high resolution like those generated by the gold standard microscopes for diagnostics and screening purposes. In contrast to these optical microscopes, however, the chip microscope based on GaN micro-/nano-LEDs will have a much wider field of view, faster image generation and—as important—can be operated in harsh environments, e.g., inside biological incubators. This might lead to a revolution in point-of-care medical analysis or environmental analysis, which is definitely an important area of application of micro-LED modules. Moreover, highly efficient light sources can be realized by scaling down the size of micro-LEDs to nano-LEDs, as the droop can be minimized and the EQE can be increased. The fabrication of such a very small InGaN LED array with individually controlled pixels is however still a challenge, especially when a green LED is required like in common biological sensors. The upcoming research to solve the green gap issue will be very important to support the applications of compact mini microscopes.

## 2. Optoelectronic tweezers

In miniaturized biological and chemical analytical systems, methods for a quick, noncontact, and noninvasive micromanipulation of cells play a significant role toward further understanding of cell behavior. Currently, relatively powerful and bulky laser systems are normally used for this. Compact micro-LED arrays can contribute to be an alternative excitation source for a portable optoelectronic tweezer, which is principally a micromanipulator utilizing light-induced dielectrophoretic forces on a photoconductive substrate. This technique is considered to be relatively novel compared to other existing noncontact manipulation methods based on, e.g., electrical/pure dielectrophoretic,<sup>238–240</sup> surface acoustic wave,<sup>241</sup> ultrasonic wave,<sup>242</sup> optical,<sup>243</sup> and magnetic forces.<sup>244</sup> Using the optoelectronic tweezers, various biological samples (e.g., particles,<sup>245–247</sup> cells,<sup>245,247–253</sup> proteins,<sup>254</sup> and DNA molecules<sup>255,256</sup>) have been investigated in real-time using light images that are projected on transparent electrodes, e.g., indium tin oxide (ITO) and amorphous silicon coated glass (a-Si:H) [Figs. 13(a) and 13(b)].<sup>257</sup> Besides micro-LED arrays,<sup>23,257–259</sup> other light sources have been reported to trigger and pattern virtual electrodes [e.g., LCD

display,<sup>260</sup> digital micromirror device (DMD) projectors,<sup>245,247,261</sup> and laser beams<sup>262</sup>].

Although all available noncontact cell manipulation techniques have their own distinct advantages and disadvantages, the optoelectronic tweezer, especially if composed of micro-LED array, has shown its superiority among others. In comparison to conventional electrical or dielectrophoretic trapping, the optoelectronic tweezer can modify the light field simply by moving it from one pixel to the others.<sup>240,257</sup> Furthermore, several biological objects or particles can be manipulated in parallel depending on the micro-LED pattern. These two working options are not possible with magnetic or normal optical tweezers, which only offer one degree of control. Trapping by optoelectronic tweezers in general has been indicated to be 470 times stiffer than a conventional optical tweezer with a similar light intensity<sup>262</sup> and capable of manipulating high numbers of cell and particles in parallel (i.e., 15 000 trapped objects at once with only 1 mW of light).<sup>245,261</sup> An optoelectronic tweezer based on an  $8 \times 8$  GaN micro-LED matrix has been reported to be able to manipulate and trap multiple particles [e.g.,  $10 \mu\text{m}$  polystyrene beads and live cells, see Figs. 13(c) and 13(d)]. During trapping experiments, a light power density of  $0.4\text{--}0.6 \text{ W/cm}^2$  was sufficient to excite the cells on photoconductive electrode and to investigate their velocity profiles [Fig. 13(e)].

As the first demonstration of the micro-LED-based optoelectronic tweezer was mainly used to manipulate the “bare” cells,<sup>257</sup> a further improvement was made by developing a projection system based on individually controlled GaN micro-LED arrays to manipulation of fluorescently labeled cells [Fig. 13(f)].<sup>258</sup> The additional key components for this setup are two integrated objective lenses that can demagnify and project the light emitted from the micro-LED arrays onto the optoelectronic tweezer device, resulting in a smaller pixel size used to activate each cell trap. Moreover, differentiating from the other fluorescent-cell manipulators that normally combine two separate systems for trapping and fluorescence excitation,<sup>249</sup> the micro-LED-based projection system could demonstrate single-cell manipulation and fluorescence imaging using the same illumination source where two emission wavelengths have been investigated (450 nm and 520 nm).<sup>258</sup> This demagnification-based optoelectronic tweezer system has been successfully tested in a proof-of-concept biomedical measurement to study T-lymphocyte and dendritic cells, which are commonly used by pharmacists or medical researchers to investigate the immune system toward infection or vaccination.<sup>263</sup> A viscous drag method was employed to measure the cell velocity and trapping profile, in which Stokes' law was required to determine the dielectric force.<sup>264</sup> It should be noted that the cell velocity is directly proportional to the increase in the dielectrophoretic force on the “virtual imaged electrode” created by the projected micro-LEDs [Fig. 13(g)]. During trapping, the cells are attracted to the imaged LED pixels [Figs. 13(h) and 13(i)]. Furthermore, different types of cells in a mixed population can be distinguished by introducing two different contrasting fluorescent dyes [see Fig. 13(j)]. All these developments and experiments have demonstrated the feasibility of integrating GaN micro-LED arrays in compact and low-cost systems to build noncontact and noninvasive micromanipulator system for the investigation of biological objects, including cells.

For further development, GaN micro-LED arrays can be integrated directly with microlens array to realize novel optical tweezers, so that each pixel can be switched on/off individually at different

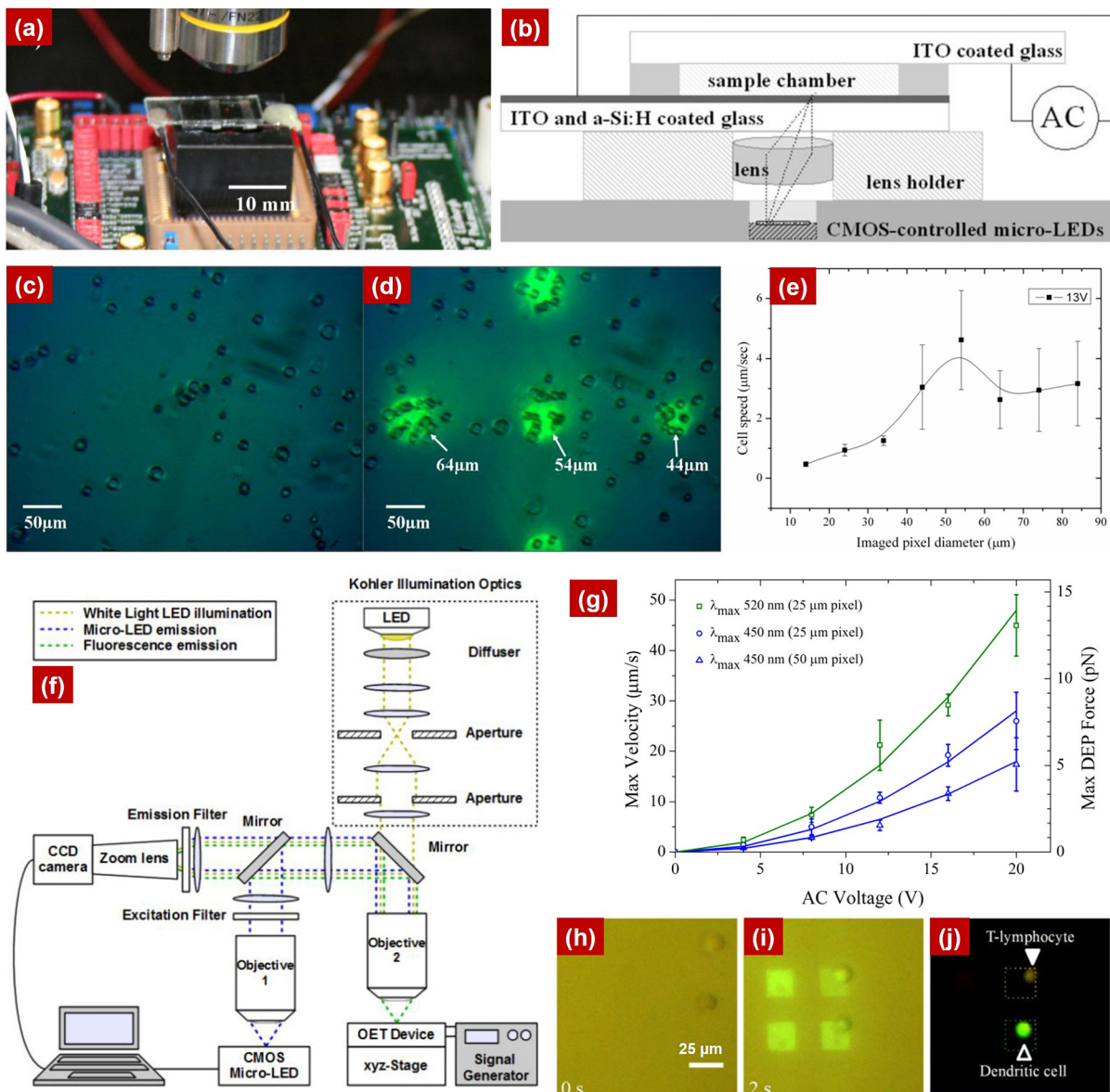


**FIG. 13.** (a) Photograph and (b) sketch of the integrated miniaturized optoelectronic tweezer using a CMOS-controlled LED array as the excitation source. The conditions during cell trapping experiments (c) before and (d) after some micro-LED pixels have been turned on. The used illuminating chip contains an array of  $8 \times 8$  GaN micro-LED pixels on a  $200 \mu\text{m}$  center-to-center pitch, flip-chip bonded to a CMOS control circuit. (e) Average cell velocity as a function of imaged pixel diameter with an applied AC voltage of 13 V between ITO electrodes. Reproduced with permission from Zarowna-Dabrowska *et al.*, Opt. Express **19**(3), 2720–2728 (2011).<sup>257</sup> Copyright 2011 Author(s), licensed under a Creative Commons Attribution 4.0 License. (f) Setup of the micro-LED projection system comprising two microscope objectives as demagnification tools for having a smaller size of pixels imaged onto the optoelectronic tweezer device. (g) Maximum average velocity of DO11.10 T-lymphocyte hybridoma cells affected by dielectrophoretic force as a function of applied voltage at a LED modulation speed of 30 kHz. Image sequence depicting the conditions of cells (h) before and (i) after micro-LEDs have been turned on as well as (j) the yielded fluorescence image of T-lymphocyte (orange) and dendritic cell (green). Reproduced with permission from Jeurissen *et al.*, Opt. Express **22**, 1372–80 (2014).<sup>258</sup> Copyright 2014 Author(s), licensed under a Creative Commons Attribution 4.0 License.

times. This is definitely not possible when the conventional large LEDs are used (for example SMD LEDs). Having lower efficiency droop and high modulation speed and bandwidth up to gigahertz, the GaN micro-LEDs can be used to manipulate physically the cells and particles that are flowing in the liquid (i.e., the objects are not only in

steady-state) with very high precision and high spatial resolution when the pitch of the micro-LED can be kept as short as possible. However, besides complicated GaN LED nanoprocessing to realize the nano-LED array, challenges are still on how to obtain sufficient light intensity that is comparable with that produced from laser as the LED size

is reduced and how to overcome the temperature increase inside the microfluidic chips or petri dish caused by the emitted light.

### 3. Fluorescence-based sensors

There has been growing interest for novel fluorescence-based sensors in the fields of biomedicine and life sciences, as these methods can be used not only for particle and tissue imaging,<sup>265–267</sup> but also for cellular imaging and tracking,<sup>265,268–271</sup> molecular imaging,<sup>272</sup> and DNA sequencing.<sup>273–275</sup> In fluorescence analytical systems, samples are labeled with fluorescent molecules that can absorb an excitation light from an illumination source and subsequently emit fluorescence signal at a longer wavelength, which is then detected and quantified using a photodetector. Depending on the light excitation and emission recording mechanism, the fluorescence measurements can be divided into two main types: steady-state and time-resolved fluorescence measurements.<sup>276</sup> A steady-state fluorescence characterization is conducted by exciting the fluorescent-labeled sample with a continuous illumination and recording the emitted spectra. Meanwhile, time-resolved fluorescence measurement offers higher sensitivity and selectivity than steady-state measurement because this technique is able to record high temporal resolution after a pulsed excitation comes from the light source. Thus, it will provide more detailed information about fluorescent molecular interactions and the surrounding chemical environment of the fluorophore (e.g., local viscosity in cell membranes and pH level).<sup>277–280</sup> In time-resolved experiments, the fluorescence decay profile is used to extract the fluorescence lifetime,<sup>178</sup> e.g., via time-gated<sup>281,282</sup> or time-correlated single photon counting techniques.<sup>283,284</sup>

For standard fluorescence microscopy tools, pulsed laser diodes with different wavelengths (deep UV, visible, and near infrared) and pulse repetition rates<sup>285–289</sup> are normally employed as fluorescence excitation sources. Previously, mercury arc lamps with broadband continuous emission have also been used.<sup>290</sup> However, their low efficiency, low stability, and large size have led to unsuitability for creating small portable biochemical monitoring systems. As an alternative, InGaN/AlGaN LEDs with an optical pulse of 4 ns, a repetition rate of 10 kHz, a peak current of 2 A, and a peak optical power of 40 mW were employed by Araki and Misawa in 1995 to demonstrate, for the first time, LED-based fluorescence lifetime measurement of quinine-sulfate solution.<sup>291</sup> Furthermore, the next improvement in terms of LED miniaturization for fluorescence measurement was achieved when an individual addressable blue microdisk LED array with a wavelength of 460 nm, a pixel number of  $64 \times 64$ , and a pixel size of 20  $\mu\text{m}$  was realized,<sup>292</sup> which however was still driven by an external driver circuit<sup>293</sup> for obtaining a pulse width of 2 ns and an average optical power of 40 nW under bias of 4 V.<sup>294</sup> In that system, a fast photomultiplier tube was utilized as the detector to capture the emitted fluorescence signal during lifetime measurement of the mitochondria staining dye Rhodamine 123.<sup>294</sup> In combination with microfluidics and a hydrogenated amorphous silicon (a-Si:H) pin photodiode, GaN micro-LEDs could be also used as a fluorescence biosensor to detect fluorescence from a streptavidin R-phycoerythrin conjugate that bound to biotinylated antibody-coated microbeads.<sup>295</sup> Other than micro-LED arrays, some research groups have used vertical cavity semiconductor devices [e.g., vertical-cavity surface-emitting laser (VCSEL)] to be integrated into fluorescence-based microanalytical devices.<sup>296,297</sup> Besides on rigid substrates, the microscale VCSEL array

has been also integrated on flexible, liquid-proof polyethylene terephthalate (PET) substrates for realizing flexible opto-fluidic fluorescence sensors.<sup>156</sup>

Utilizing currently developed advanced microfabrication methods and fast electronics, complete portable integrated optoelectronic systems have been built and demonstrated as a full optical lab-on-a-chip for measurements of fluorescence lifetime of fluorescence colloidal quantum dots based on time correlated single-photon counting, in which the CMOS-controlled UV micro-LED array as the illumination source was combined with silicon-based SPAD as the detector [Figs. 14(a)–14(f)].<sup>298–300</sup> In terms of the sensing system architecture, there are at least two different options that can be considered depending on the location of the SPAD and the capturing process of the emitted fluorescence light {i.e., reflection mode [see Fig. 14(b)] and transmission mode [see Fig. 14(e)]}.

For reflection mode, the fluorescence sample is located on top of the flipped transparent sapphire substrate [Fig. 14(b)]. Thus, once the sample has been excited by the light coming from the micro-LEDs, any returning or reflected fluorescence light will pass through the stack of LED layer and its sapphire substrate, approaching the SPAD array [Fig. 14(c)]. The typical fluorescence decay curves from the time-resolved measurements performed using individually addressable  $16 \times 4$  UV micro-LED array bump-bonded with CMOS chip [Fig. 14(a)] where each LED pixel has a diameter of 72  $\mu\text{m}$  on a 100  $\mu\text{m}$  pitch and a peak emission at 370 nm (Ref. 301) are shown in Fig. 14(g). In the joining process of the micro-LED with CMOS, oxygen plasma etching can be employed to remove the polyimide layer that originally covers the SPAD top surface, so that the photon detection probability of the underlying SPADs can be enhanced [Fig. 14(b)]. Detailed specifications related to the structures and performance of the employed SPAD have been described in Ref. 302.

For transmission mode, two-chip sandwich microsystem architecture can be realized by incorporating the Si-CMOS driving circuit, micro-LED array, a microcavity slide for the fluorescence sample, optical filter, and SPAD in a sequential cascade assembly [Fig. 14(e)].<sup>299,300</sup> This approach has been introduced by Rae *et al.* where they used a micro-LED array with a pixel number of  $8 \times 8$ , a pixel diameter of 72  $\mu\text{m}$ , a pitch of 200  $\mu\text{m}$ , and a peak wavelength of 450 nm as a light source [Fig. 14(d)],<sup>303</sup> even though pixel downscaling to 20  $\mu\text{m}$  with a larger number of  $128 \times 96$  array was also demonstrated.<sup>304</sup> Moreover, the optical filter could be employed to decrease measurement errors caused by the detection of scattered light from the original excitation. In this system, the micro-LED device was mounted on the dedicated printed circuit board (PCB) daughter card facing down to the SPAD detector chip that was located on a field-programmable gate array (FPGA) board [Fig. 14(f)] and was used to measure fluorescence lifetimes [Fig. 14(h)].

From all demonstrated results of those two systems (i.e., reflection and transmission modes), it is obvious that the development of nanosecond chip-based fluorescence sensors integrating CMOS-driven GaN micro-LED arrays and Si SPAD detectors has reached a much greater level of integration and miniaturization compared to other fluorescence-based analysis systems.<sup>291,294–296</sup> In terms of the excitation source, micro-LED arrays are versatile, as the wavelength, pixel number, and size can be easily adjusted. The device fabrication processing steps can be applied to any planar MOCVD-grown LED wafer. Meanwhile, from the detector side, SPADs provide several

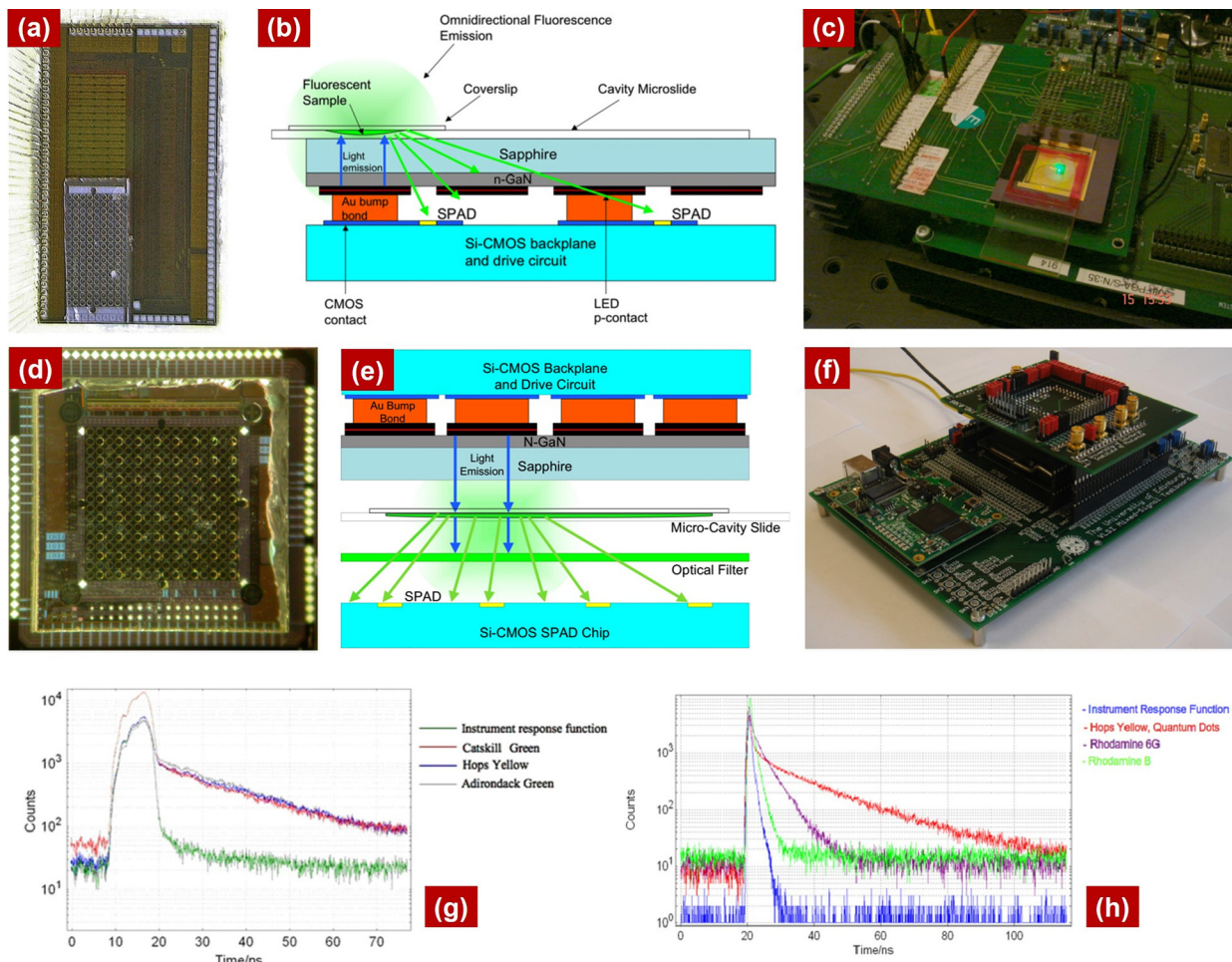


**FIG. 14.** Single-chip fluorescence microsensor system consisting of (a) 16 × 4 UV micro-LED array bump-bonded to the CMOS driving array, where (b) the transparent sapphire substrate allows the fluorescence emission to pass and reach the SPAD below in reflection mode. (c) Photograph of the single-chip fluorescence sensor system when the Adirondack Green quantum dots on a microcavity slide are excited by UV micro-LEDs. Reprinted with permission from Rae *et al.*, J. Phys. D: Appl. Phys. **41**, 94011 (2008). Copyright 2008 IOP Publishing. Two-chip fluorescence microsensor system comprising (d) 8 × 8 blue micro-LED array bump-bonded to the CMOS driving array, in which (e) the microcavity slide sealed by a coverslip to put the sample of interest is located between sapphire of the micro-LED and Si-CMOS SPAD detector. An optical filter prevents excitation light from approaching the detector array. (f) The printed circuit board (PCB) daughter card is physically supported by the stacked header pins that can be adjusted. Reproduced with permission from Rae *et al.*, Sensors **9**, 9255–9274 (2009). Copyright 2009 Authors, licensed under a Creative Commons Attribution 4.0 License. Instrument response function and fluorescent decay curves for (g) quantum dots at three different emission wavelengths in single-chip system configuration. Reprinted with permission from Rae *et al.*, J. Phys. D: Appl. Phys. **41**, 94011 (2008). Copyright 2008 IOP Publishing. (h) Quantum dots and Rhodamine samples in two-chip sensor system configuration. Reproduced with permission from Rae *et al.*, Sensors **9**, 9255–9274 (2009). Copyright 2009 Author(s), licensed under a Creative Commons Attribution 4.0 License.

significant advantages over other photodetectors (e.g., conventional photomultipliers,<sup>291,305</sup> CMOS photodiodes,<sup>306</sup> and 0.18  $\mu\text{m}$  CMOS image sensors<sup>307</sup>). They are extremely fast and sensitive to single-photon from the fluorescence signal (ns time-resolved detection possible), robust (not being destroyed by high light levels and insensitive to magnetic fields), and relatively straightforward to be fabricated (compatible with large scale Si CMOS production).<sup>308,309</sup> Moreover, SPAD detectors made of InGaAs/InP capable of detection in the near infra-red range have also been reported for quantum communication,<sup>310</sup> regardless of the inability of integrating their fabrication processes in silicon-based CMOS technology due to material incompatibility.<sup>310–313</sup> Furthermore, a low-cost configuration for continuous steady-state fluorescence measurement has

been reported as an on-chip wide-field holographic fluorescent imaging platform without any lens and mechanical scanner, which can perform high-throughput screening of cells.<sup>314</sup>

#### 4. Optogenetics

Apart from imaging, micro-LED arrays have been used to stimulate and sense neurons, serving as a high resolution light source for optogenetic applications, such as for neural stimulation in brain,<sup>315–319</sup> retinal prosthesis,<sup>320–322</sup> and in the auditory system (spiral ganglion neurons in cochlea).<sup>323–327</sup> The recent improvement of various techniques in optogenetics to both control and readout the neural activities

have revolutionized and transformed neuroscience into a new era of light.<sup>328,329</sup> In comparison to the widespread electrical stimulation, utilizing light as a stimulation tool provides several benefits. It is noninvasive, can be targeted with a very high spatial and temporal precision (especially when the devices are miniaturized into micro-/nanoscale), can be employed simultaneously at multiple locations, can be tailored to emit different wavelengths, and can inform and record the activity of specific molecules. Moreover, this development has been evolved over the past decade to overcome the issues and limitations in both *in vivo* (i.e., using a whole, living organism, typically applied in animal studies or clinical studies<sup>315,316</sup>) and *in vitro* (i.e., in a controlled environments outside of the living organism mimicking its real condition using cell culture or micro-/nanofluidic device<sup>330–332</sup>) experiments.

For the aforementioned optogenetic applications, light power densities of a few milliwatts per square millimeter are favorable to stimulate channelrhodopsin-2 (ChR2), which is a membrane channel protein whose gating is controlled by illumination.<sup>325,333–337</sup> Its expression in neurons enables the permeation of different monovalent and divalent cations,<sup>334,338</sup> causing a rapid and reversible light-controlled depolarization (i.e., reduction of cell membrane potential), hence regulating the activation/inactivation of neurons in specific locations.<sup>323,330,339,340</sup> In most cases, the photosensitive ChR-2 has been employed as an indicator in LED-based optogenetics as it has an active peak at around 460–470 nm, which is compatible to blue light emitted by InGaN/GaN LEDs.<sup>340,341</sup> The other protein molecules (opsins) in the cell membranes that are sensitive to the light are halorhodopsins [e.g., natromonas pharaonis halorhodopsin (NpHR)],<sup>342</sup> which can react well with illumination of 590 nm.<sup>343</sup>

During neural stimulation, the minimum spiking irradiance of ChR2 using 470 nm light is in the range of 0.1–1 mW/mm<sup>2</sup>, which corresponds to the minimum light source luminance of 10<sup>6</sup>–10<sup>7</sup> cd/m<sup>2</sup>.<sup>322,340</sup> Even though this irradiance level can also be obtained by other illumination sources (e.g., lasers,<sup>344</sup> xenon arc lamps,<sup>341</sup> and bulk high-powered LEDs<sup>345</sup>), these conventional approaches still can only offer low spatial resolution. In 2008, Poher *et al.* had successfully fabricated GaN micro-LED arrays in two different designs {i.e., 64 × 64 matrix addressable and 120 × 1 stripe addressable micro-LEDs [Figs. 15(a) and 15(b)]} that were demonstrated for imaging of stained pollen grains<sup>346</sup> and *in vitro* hippocampal neurons,<sup>350</sup> respectively, with three different wavelength options of 370 nm (UV), 470 nm (blue), and 520 nm (green) [Fig. 15(c)]. Matrix-addressed micro-LED arrays were formed by first insulating columns (lines) as the common cathode through Cl<sub>2</sub>/Ar-based ICP dry etching until sapphire, and then etching rectangular mesas only until *n*-GaN to form individual LEDs. A thin SiO<sub>2</sub> insulating layer was thereafter deposited on the whole substrate. Metal line anodes, which form ring-shaped *p*-contacts on top of rectangular mesa structures, were deposited across the mesa structures to finally connect all the LEDs, as well as to reduce any cross talk or leak effect.<sup>330,340,347</sup> The stripe micro-LED arrays of the UV and blue emitters could produce sufficient irradiances of 5 and 11 nW/μm<sup>2</sup>, respectively, to induce photoactivation of caged fluorescein (a strong fluorophore used in cell imaging and microfluidics measurements), as well as to evoke spikes in hippocampal ChR2-expressing neurons that were prepared from rat embryos.<sup>350</sup> However, each LED stripe still had a large dimension (i.e., length of 3600 μm, width of 17 μm, and total area per LED stripe of 61200 μm<sup>2</sup>) leading to inability to create

localized illumination to individual neurons or smaller parts of dendrites.

To improve spatial resolution, a 64 × 64 GaN micro-LED array with 20 μm pixel diameter and 50 μm center-to-center spacing [Fig. 15(c)] has been developed and used for a next phase of optogenetic experiments, where two types of neurons (i.e., hippocampal neurons obtained from tissue of Sprague-Dawley rats and ChR2-transfected retinas of knocked-out mice<sup>340</sup>) have been excited. The employed LEDs emitted light at 470 nm with a full width half maximum (FWHM) of 22 nm, so that they had an overlap with the peak sensitivity of ChR2.<sup>350</sup> A single micro-LED could produce an output power of 70 μW and irradiance of 250 mW/mm<sup>2</sup>, which was sufficient to surpass the stimulation threshold of ChR2. In addition, a demagnification approach has been chosen to further reduce the pixel size and simultaneously increase the spatial resolution [Figs. 15(d) and 15(e)]. As a consequence, this has led to the possibility of examining a single neuron in more detail as well as neural networks with a smaller size.<sup>330,340</sup> In terms of the architecture of individually controlled micro-LEDs, a directly addressed 16 × 16 GaN micro-LED array with 150 μm pitch and 25 μm diameter was also reported using a similar method from matrix-addressed μLEDs.<sup>351</sup> However, in this concept, each LED pixel has a separate anode connection and is equipped with a common cathode (*n*-contact). Flip-chip bonding was used to integrate the micro-LEDs in a 281-pin ceramic pin grid array (PGA) package, leading to a light emission through the sapphire substrate. From the experiment using retinal ganglion cell (RGC) neurons transfected with ChR2, this directly addressed micro-LED array has been found to effectively create 500 ms pulses at a frequency of 1 Hz.<sup>351</sup>

However, despite all promising photoactivation results of neurons, the demonstrations shown by Poher *et al.* and Grossman *et al.* were still performed *in vitro*.<sup>330,340</sup> In future, those concepts should be applicable to *in vivo* experiments as they can provide more insights on the real neural condition and effects of the photoactivated neurons in cells. Therefore, some research groups have attempted to develop microdevices with integrated micro-LED arrays that can be used to stimulate neurons *in vivo*.<sup>315–317,325,348,352–354</sup>

Based on implanting strategies of the optical devices into the targeted deep brain regions, implants can be classified into three different types: waveguide-based implants, implanted micro-LEDs, and coupling of micro-LEDs with implanted optical waveguides.<sup>318,355,356</sup> Before individually addressable micro-LEDs were introduced, *in vivo* optogenetics were performed by waveguide-based multipoint stimulation devices made of optical fibers.<sup>357–366</sup> This requires tethering of the targeted animal onto an optical bench to be coupled with light injection system, in which the typical used light sources are lasers (e.g., 473-nm ps-pulsed laser<sup>366</sup>). It should be emphasized that this approach has a severe drawback as the animal movement results in fiber bending and stretching, which can lead to cross-talk between the different waveguide channels and generate inhomogeneous light distribution.<sup>365,366</sup>

Meanwhile, several techniques involving neural probes were demonstrated to directly implant the LED array inside the target area [Fig. 15(f)].<sup>315,316,348</sup> These micro-LED-integrated neural probes can be merged with flexible substrates like in OLED structures,<sup>367,368</sup> combined with multimodal sensors, and powered wirelessly, which will provide benefits during slight movement made by the investigated animals.<sup>316,317,356,369</sup> The substrates used for implants can be varied

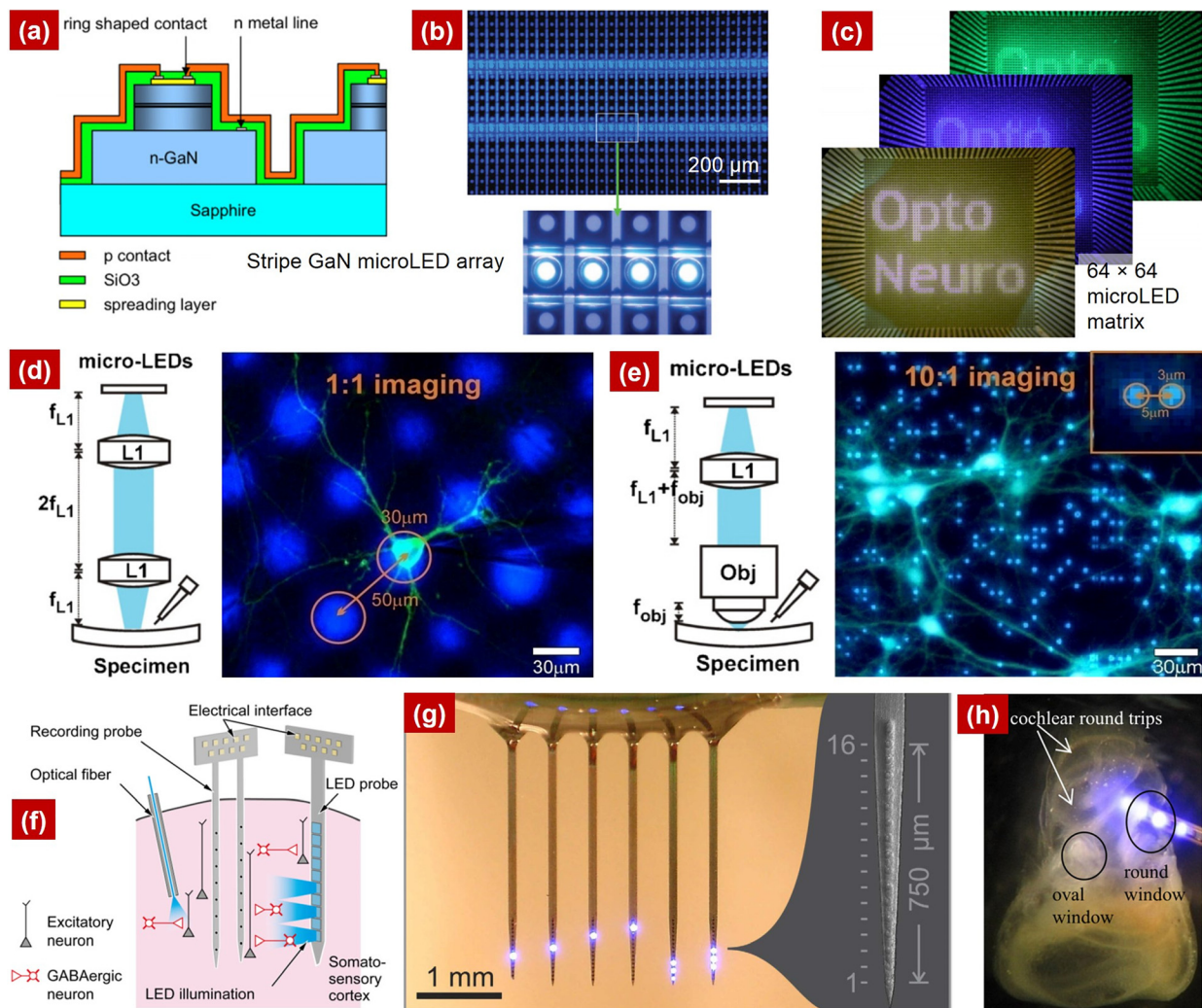


**FIG. 15.** (a) Cross-sectional sketch and (b) micrograph of the stripe-based addressable micro-LED array used for optogenetics. Reprinted with permission from Poher *et al.*, J. Phys. D: Appl. Phys. **41**, 094014 (2008).<sup>330</sup> Copyright 2008 IOP Publishing. (c) 64 × 64 matrix of 20 μm InGaN/GaN LED array with wavelengths of 370 nm (UV), 470 nm (blue), and 520 nm (green). Reprinted with permission from Poher *et al.*, J. Phys. D: Appl. Phys. **41**, 094014 (2008).<sup>330</sup> Copyright 2008 IOP Publishing. Imaging configurations and their experimental results during neuron stimulations when (d) micro-LED array is imaged 1:1 on the neural sample using two lenses in 4f relay architecture and (e) demagnification optical setup for 10:1 imaging using one lens and an objective is employed. Reprinted with permission from Grossman *et al.*, J. Neural Eng. **7**, 16004 (2010).<sup>340</sup> Copyright 2010 IOP Publishing. (f) Schematic of an implanted micro-LED-based optical probe and its corresponding recording probe providing multisite stimulation ability, in comparison with only an optical fiber providing a single optical stimulation site. Reprinted with permission from Ayub *et al.*, Biomed. Microdevices **19**(3), 49 (2017). Copyright 2017 Springer Nature.<sup>348</sup> (g) Scalable 6-shank micro-LED probe with 16 micro-LEDs per shank, resulting in 96 individually addressable stimulation sites. This is used to demonstrate the scalability of micro-LED probe. Reproduced with permission from Scharf *et al.*, Sci. Rep. **6**, 28381 (2016).<sup>349</sup> Copyright 2016 Author(s), licensed under a Creative Commons Attribution 4.0 License. (h) Implantation of 230 μm wide flexible probe with integrated micro-LEDs to a mouse cochlea. Reprinted with permission from Goßler *et al.*, J. Phys. D: Appl. Phys. **47**, 205401 (2014).<sup>324</sup> Copyright 2014 IOP Publishing.

depending on the targeted depth and shape of regions (e.g., silicon microneedles,<sup>348,349,352,370</sup> thin plastic films,<sup>315</sup> polyethylene terephthalate (PET) needles,<sup>316</sup> polyimide substrate [Fig. 15(h)],<sup>324</sup> and transparent epoxy resin E301<sup>327</sup>) The tip is usually designed as a thin but long shank, where its free end is created in a tapered shape to minimize tissue damage during insertion.<sup>354</sup> The other end of the probe consists of bonding pads allowing each micro-LED to be directly and individually addressed. Moreover, multiple shanks can be realized to

increase the number of optical sites during optogenetic experiments [Fig. 15(g)].<sup>349</sup> In terms of a flexible probe, Klein *et al.* had recently improved their previous devices<sup>324</sup> for optical cochlear implant by overcoming problems of pronounced thermomechanical probe bending.<sup>327</sup> In recent work, they reported the use of highly transparent epoxy resin E301 instead of polyimide as a substrate. Moreover, individually matrix-controlled blue micro-LEDs were distributed along a bendable probe shaft. Besides using micro-LED-based stimulation,

another strategy using infrared lasers was also reported to drive the auditory neurons (cochlea). Although this concept has been applied and researched in terms of its temporal fidelity, spatial excitation, and energy requirement,<sup>323</sup> it is still facing a severe problem in some *in vivo* cases, where the strong infrared laser pulse inducing photoacoustic stimulation does not trigger the auditory activity of entirely deafened cochleae effectively.<sup>371</sup> Furthermore, an *in vitro* experiment done using infrared light-excited cultured cells seems to require a higher activation energy, leading to a different membrane-bound optothermal mechanism of depolarization.<sup>339</sup> This suggests the necessity of performing optogenetic stimulation directly in the living organism (*in vivo*) to observe the phenomena of the biological neurons in its natural environment.

Despite all those advantages offered by micro-LED arrays, a heating problem during operation still needs to be tackled, since it may damage the surrounding tissue. Temperature increase during the *in vivo* test is suggested to be kept below 0.5 °C.<sup>353,354</sup> The minimum distance between multiple LEDs depends strongly on the presence of a dielectric material at the LED/tissue interface, which is limited by the Lambertian emission profile of the micro-LEDs and tissue scattering.<sup>354</sup> Furthermore, a hybrid technological approach consisting of micro-LED array coupled into MEMS-implanted waveguides was reported in recent years to try to overcome the faced issues.<sup>377–381</sup> Schwaerzel *et al.* have fabricated 3 × 3 independently controllable LEDs integrated with a microstructured silicon housing and optical glass fibers.<sup>379</sup> That device has been placed on a highly flexible polyimide ribbon cable. Similar work was reported by Kwon *et al.*, in which they coupled 4 × 4 micro-LEDs with slanted SU8-based microneedle waveguides. Their device could already be driven wirelessly and had allowed for a precise and simultaneous light delivery to multiple cortical layers of a rat.<sup>378</sup> Very recently, another device alternative for optogenetics using a hybrid approach was reported, which is the so-called Utah Optrode array. This device has integrated a 10 × 10 glass waveguide array, a micro-LED array, and a pinhole, which then enables the coupling of light into deep brain regions with excellent spatial control.<sup>377,380,381</sup> This hybrid method however still has main limitations related to the divergence of the light radiation pattern, which leads to a reduced spatial control.<sup>379</sup>

Micro-LED arrays have been utilized not only in the neural cells (brain and auditory system), but also for retinal ganglion cells to provide a retinal prosthesis (i.e., so-called optobionic vision).<sup>321,322</sup> This has been motivated by the conditions of blind patients.<sup>320,322</sup> Since the eyes are transparent, external photostimulation of ChR2 to render light sensitivity onto the residual retinal neurons<sup>322,340</sup> could be realized. Thus, direct implantation may not be required. However, ChR2-based retinal prostheses need to have a light source that is capable of generating 2D stimulation patterns (resolution > 1000 points) with micrometer (20 μm) and millisecond (< 1 ms) resolution and with sufficient radiance (> 50 mW/mm<sup>2</sup> sr) to induce action potentials in neurons.<sup>340</sup> For eye-related optogenetics, zebrafish has been normally used as a model to study these phenomena.<sup>319,382</sup> An array of 90 × 90 blue GaN micro-LEDs combined with CMOS driving circuit was developed by AMS foundry for retinal prosthesis with an eye-tracking system.<sup>383,384</sup>

Table III summarizes various micro-LEDs reported in the literature that are employed for optogenetics. They are mostly configured in three different types (i.e., micro-LED array on penetrating probe,

surface-mounted micro-LED array, and micro-LED-coupled optrode array). All of them employed blue InGaN/GaN LED substrates and emitted blue light (405–470 nm) with an intensity of 1–600 mW/mm<sup>2</sup>. Optogenetic test validations were also conducted both *in vivo* and *in vitro*. For the *in vivo* measurements, mouse brain (visual cortex) was commonly used to be the object of neural characterizations.

All in all, micro-LED-based optogenetics is believed to move quickly to more advanced devices in the next few years by combining individually controllable micro-/nano-LEDs and micro-/nanoelectromechanical systems (M/NEMS)-based structures (e.g., micro-/nano-optics to collimate the light emission from micro-LEDs<sup>385</sup>). All developed micro-LED arrays are currently still limited to sizes of a few tens to a few hundred micrometers. However, these LED dimensions will be further scaled down taking advantage of the continuously ongoing development in 3D nanoprocessing that has been applied for creating, e.g., vertical GaN nano-FETs.<sup>7,14,119,386</sup>

## E. Chemical sensors for environmental monitoring

In contrast to high-end analytical chemical systems—like chromatography, where high detection capabilities are a must,<sup>387</sup> sensors for environmental monitoring are mainly driven by the right balance between sufficient performance and acceptable cost.<sup>388–391</sup> While the former are regarded as singular investments, the latter are expected to be produced and deployed at mass scale, and thus, at reduced cost.

In this context, integrated light sources like micro-/nano-LEDs are sought-after resources for chemical sensors. If those were available, several chemo-electric transduction schemes, which are currently barely exploited, could be implemented in a cost-effective manner. For example, one of the most robust and affordable gas sensing technologies is those based on semiconductor materials.<sup>392</sup> In this technology, the electron structure of these solid materials can be dramatically altered by the presence of chemical species on their surface. This phenomenon can be used to transduce chemical signals into electronic (or optical) ones that can then be monitored by many means, as described in Secs. III E 1–III E 3. Moreover, as by scaling down the LEDs to micro-/nano-LEDs, their efficiency droop can be reduced and overall efficiency (EQE) can be increased. Thus, high-brightness but efficient light sources can be realized and integrated into different types of optical sensors used for environment monitoring.

### 1. Conductometric chemical sensors

Conductometric gas sensors are solid-state devices based on a semiconductor material—like a metal oxide (e.g., SnO<sub>2</sub>, ZnO, In<sub>2</sub>O<sub>3</sub>, and WO<sub>3</sub>)<sup>393,394</sup> or a carbon allotrope (e.g., carbon nanotubes and graphene),<sup>395</sup> in which the presence of gases leads to electrical resistance variations that are continuously monitored. It is well known that gas species can adsorb at the surface of such materials, involving charge exchanges with the bulk or dipolar interactions that are immediately reflected in a change of electrical resistance. The choice of one or another material, and its combination with other chemically active substance—like catalysts (e.g., Pt and Pd)<sup>396,397</sup> or molecular receptors (e.g., amines and thiols)<sup>398–400</sup>—determines the sensibility of the sensor toward one or another kind of gas. Similar principles have been demonstrated in more complex configurations involving semiconductor junction devices. It has been demonstrated that GaN-based junction can be used as electronic gas sensors as well.<sup>401–404</sup>

**TABLE III.** Micro-LEDs in different configurations used for optogenetics.

Light source	LED dimensions	Light intensity (maximum or used in test)	Emission color	Optogenetic test validation	Year (Reference)
Single micro-LED on penetrating polyimide probe	Size = $1000 \mu\text{m} \times 600 \mu\text{m} \times 200 \mu\text{m}$	0.7 mW/mm <sup>2</sup>	Blue (465 nm)	<i>In vivo</i> , mouse visual cortex	2013 (Ref. 372)
Single micro-LED on penetrating SU-8 probe	Size = $550 \mu\text{m} \times 290 \mu\text{m} \times 100 \mu\text{m}$	1 mW/mm <sup>2</sup>	Blue (450–495 nm)	<i>In vivo</i> , mouse brain	2014 (Ref. 373)
Micro-LEDs on penetrating polycrystalline diamond probe	Size = $550 \mu\text{m} \times 290 \mu\text{m} \times 100 \mu\text{m}$	0.6–1.5 mW/mm <sup>2</sup>	Blue (450 nm)	<i>In vivo</i> , mouse brain	2015 (Ref. 374)
Micro-LED array on penetrating sapphire probe	Array = $1 \times 5$ ; diameter = $40 \mu\text{m}$ ; pitch = $250 \mu\text{m}$	600 mW/mm <sup>2</sup>	Blue (450 nm)	None	2013 (Ref. 353)
Micro-LED array on penetrating epoxy probe	Array = $1 \times 5$ ; LED size = $50 \mu\text{m} \times 50 \mu\text{m} \times 6.45 \mu\text{m}$	7–17.7 mW/mm <sup>2</sup>	Blue (450 nm)	<i>In vivo</i> , mouse brain	2013 (Ref. 315)
Micro-LED array on penetrating SU-8 probe	Array = $1 \times 5, 5 \times 5$ ; diameter = $100 \mu\text{m}$ ; pitch = $120 \mu\text{m}$	7–17.7 mW/mm <sup>2</sup>	Blue (450 nm)	<i>In vivo</i> , mouse brain	2013 (Ref. 316)
Micro-LED array on penetrating flexible polyimide probe	Array = $3 \times 5$ ; LED diameter = $50 - 150 \mu\text{m}$	6 mW/mm <sup>2</sup>	Blue/violet (405–465 nm)	<i>In vivo</i> , mouse cochlea	2014 (Ref. 324)
Micro-LED array on penetrating silicon probe	Array = $1 \times 3$ ; LED size = $10 \mu\text{m} \times 15 \mu\text{m} \times 0.5 \mu\text{m}$ ; Pitch = $60 \mu\text{m}$	1 mW/mm <sup>2</sup>	Blue (460 nm)	<i>In vivo</i> , mouse brain (CA1 pyramidal cell layer)	2015 (Ref. 370)
Micro-LED array on penetrating silicon probe	Array = $1 \times 16$ ; LED diameter = $25 \mu\text{m}$ ; pitch = $50 \mu\text{m}$ probe number = 6;	400 mW/mm <sup>2</sup>	Blue (450 nm)	<i>In vivo</i> , mouse cortex (cortical GABAergic neurons)	2016 (Ref. 349)
Micro-LED array on penetrating flexible Si/polyimide probe	Array = $1 \times 10$ ; LED size = $270 \mu\text{m} \times 220 \mu\text{m} \times 50 \mu\text{m}$ ; pitch = 300 and 500 $\mu\text{m}$	1 mW/mm <sup>2</sup>	Blue (460 nm)	<i>In vivo</i> , mouse somato-sensory cortex	2017 (Ref. 348)
Micro-LED array on penetrating flexible transparent epoxy resin probe	Array = $12 \times 12$ ; LED diameter = $50 \mu\text{m}$ ; pitch = $100 \mu\text{m}$	407 mW/mm <sup>2</sup>	Blue (462 nm)	None	2018 (Ref. 326)
Surface-mounted micro-LED array	Arrays = $64 \times 64$ matrix, $120 \times 1$ stripe; Size = $17 \mu\text{m}$ Pitch = $34 \mu\text{m}$	5 – 30 mW/mm <sup>2</sup>	UV (370 nm), blue (470 nm), green (520 nm)	<i>In vitro</i> , ChR2 transfected neuron	2008 (Ref. 330)
Surface-mounted micro-LED array	Array = $64 \times 64$ ; diameter = $20 \mu\text{m}$ ; pitch = $50 \mu\text{m}$	250 mW/mm <sup>2</sup>	Blue (470 nm)	<i>In vitro</i> , CHR-YFP-encoded neuron, retina	2010 (Ref. 340)
Surface-mounted micro-LED array	Array = $16 \times 16$ ; diameter = $25 \mu\text{m}$ ; pitch = $150 \mu\text{m}$	86 mW/mm <sup>2</sup>	Blue (465 nm)	<i>In vitro</i> , retinal ganglion cell (RGC) neuron	2010 (Ref. 351)
Surface-mounted micro-LED array	Diameter = $200 \mu\text{m}$ ; pitch = $700 \mu\text{m}$	1 mW/mm <sup>2</sup>	Blue (460 nm)	<i>In vivo</i> , cortical interface	2013 (Ref. 375)
Micro-LED-coupled optrode array	Array = $4 \times 4$ ; LED size = $220 \mu\text{m} \times 270 \mu\text{m} \times 50 \mu\text{m}$ ; base size = $300 \mu\text{m}$ ; tip size = $30 \mu\text{m}$	1.4 mW/mm <sup>2</sup>	Blue (460 nm)	<i>In vivo</i> , rat primary visual cortex	2015 (Ref. 376)
Micro-LED-coupled Utah optrode array	Array = $10 \times 10$ ; LED diameter = $70 - 100 \mu\text{m}$ ; base size = $75 \mu\text{m}$ ; tip size < $1 \mu\text{m}$	> 80 mW/mm <sup>2</sup>	Blue (450 nm)	<i>In vivo</i> , mouse brain	2018 (Ref. 377)

Anyhow, it is important to bear in mind that these gas-surface interactions must occur continuously:<sup>405</sup> gas molecules must desorb from the surface shortly after being adsorbed to allow for other molecules to take their place. This way, the resistance signal reflects of the steady balance between adsorption and desorption of target molecules. Due to thermodynamic reasons, this balance scales with the gas concentration in the environment, which is the true magnitude of interest. Even more important: thanks to this dynamic picture, the sensor signal can retrace and return to its initial value if the gas concentration suddenly vanishes. So that the sensor is reversible and reusable.

Unfortunately, at room temperature, the adsorption rate of a chemical species usually is much larger than the desorption rate. Therefore, an appropriate dynamic balance between adsorption and desorption processes can only be achieved by adding external means to increase desorption.<sup>406</sup> After more than 50 years of development and presence in the market, the state of the art sensors use heat as an energy source.<sup>407</sup> By means of a Joule heater and a temperature sensor, the sensitive material is kept at a relatively high temperature (in the range of a few hundreds of Celsius degrees, to avoid the influence of ambient temperature fluctuations). This heating system is the major source of energy consumption of such kind of technology, and a major stopper for mobile, battery driven sensor systems. Today, low-end commercial devices need to be powered with hundreds of milliwatts to come into operation.<sup>408</sup> By means of miniaturization, such figure is lowered to a few tens of milliwatts in-state-of-the-art microintegrated devices.<sup>409,410</sup> At a research level, power consumptions in the range of microwatts are reported for nanointegrated devices.<sup>411,412</sup> However, mass scale production of this nanodevices hampers their widespread implementation.<sup>413</sup>

Besides heat, light can also be used to supply energy to the gas-surface interactions occurring in these semiconductor sensors.<sup>413,415</sup> UV and visible range photons [Fig. 16(a)] can be used both (1) to stimulate the reaction and adsorption of incoming molecules on the sensor surface, and (2) to break the bonds established between molecules and surface atoms after adsorption.<sup>416</sup> These are one-to-one interactions occurring between photons, electrons, and molecules, in contrast to the average statistical behavior occurring in temperature-driven sensors, where the process can be regulated by controlling one single easy-to-measure parameter like temperature. In light driven sensors, the photon flux (i.e., number of photons impinging on the material per unit of surface each unit of time) or equivalently the light irradiance (i.e., the same magnitude expressed in watts arriving per unit surface) must be controlled and balanced with the populations of molecules and electrons<sup>415,416</sup> [Fig. 16(d)].

Most of the first works exploring this approach are based on macroscopic light sources, like discharge lamps or encapsulated LEDs, placed at an arbitrary distance  $d$  of the sensing material [Fig. 16(b)]. This fact has two consequences. First, there is a general lack of details on the light flux/irradiance conditions used in most of the works, hampering the standardized comparison of results and the systematic development of this approach. Second, these devices are hardly reproducible and very inefficient energetically (with power consumptions well above hundreds of milliwatts). Only a few recent works attempted to harness as much light as possible, using reflectors underneath the sensor layer,<sup>417</sup> coating optical fibers with the sensor material<sup>418</sup> or stacking an (In)GaN LED with the sensor material film at macroscopic distances (e.g., between centimeters and hundreds of microns).<sup>419–421</sup>

These approaches represented a relative increase in efficiency, but with power consumptions still in the range of tens of milliwatts, since the LEDs used were not designed or optimized for this application.

Very recently, an optimized configuration, so-called the micro-light plate,<sup>26,422</sup> has been proposed [Fig. 16(c)]. In the microlight plates, the sensor material is stacked at a nanometric distance  $d$  on a micro-LED source. Due to this minimum distance between the light source and the sensor material, light spreading is minimized, harnessing all the light emitted to activate the sensor response. Also, the use of a miniaturized micro-LED—with an area [ $w \cdot l$  in Fig. 16(c)] that matches that of the sensor material—minimizes the total current needed to lit on the light source, and thus the power consumption. This is therefore a beautiful example of the opportunities opened by the current trend in LED miniaturization. In fact, power consumptions as low as tens of microwatts have already been demonstrated [Fig. 16(d)], using micro-LEDs made with conventional microprocessing methods that can be easily scaled up.

With these results, it is interesting also to realize that, to supply a similar amount of energy in order to the sensor material to achieve an equivalent functionality, the electro-optical conversion of the LEDs is much more power efficient than the electrothermal conversion of a Joule heater. On top of the intrinsic efficiency of the LEDs, another big difference is also that light can be confined and directed onto the area of interest, whereas temperature is spreading out across macroscopic regions of the device. Therefore, it is expected that such values can be significantly improved in the future by means of further miniaturization and higher localization of the light source.

Concerning specificity, a general trend points at an increased sensitivity toward oxidizing species, when  $n$ -type metal oxides are used as sensor materials [Fig. 16(d)]. This opens to door toward light activation methods that could increase the selectivity, one of the most challenging features in current sensors. In relation to GaN LEDs, which precisely operate in the wavelengths of interest—UV, visible-, current possibilities of microprocessing and microintegration open a promising path for fully integrated, cost effective, and power-efficient light-driven conductometric sensors. Some of the open challenges to address in this field are the prevention of undesired heating during LED operation, and the true regulation of the emission, beyond a mere monitoring of the electrical power applied.

## 2. Luminescent chemical sensors

The alterations in the electron structure of semiconductor materials by the presence of chemical adsorbates can also be monitored by optical means. It has been reported that presence of molecules at the surface of semiconductor materials can be interrogated by spectroscopic means.<sup>423,424</sup> Specifically, the photoluminescence (PL) signal of semiconductors like porous silicon,<sup>425</sup> ZnO,<sup>426</sup> SnO<sub>2</sub>,<sup>427</sup> and GaN<sup>428–430</sup> can be quenched by gaseous species.

Remarkably, this effect is quite specific to different kinds of molecules and occurs at relatively fast timescales. In contrast to electrically interrogated approaches, where the presence of gases can only be measured locally, right in the spot where the sensor is placed, photoluminescence sensors can be used to sense broader areas. For example, nanoprobe made of a heterostructured GaN nanoparticles can be produced in bulk amounts.<sup>431,432</sup> Due to their good optoelectronic properties, the PL signals of such nanoprobe is brilliant and can be easily

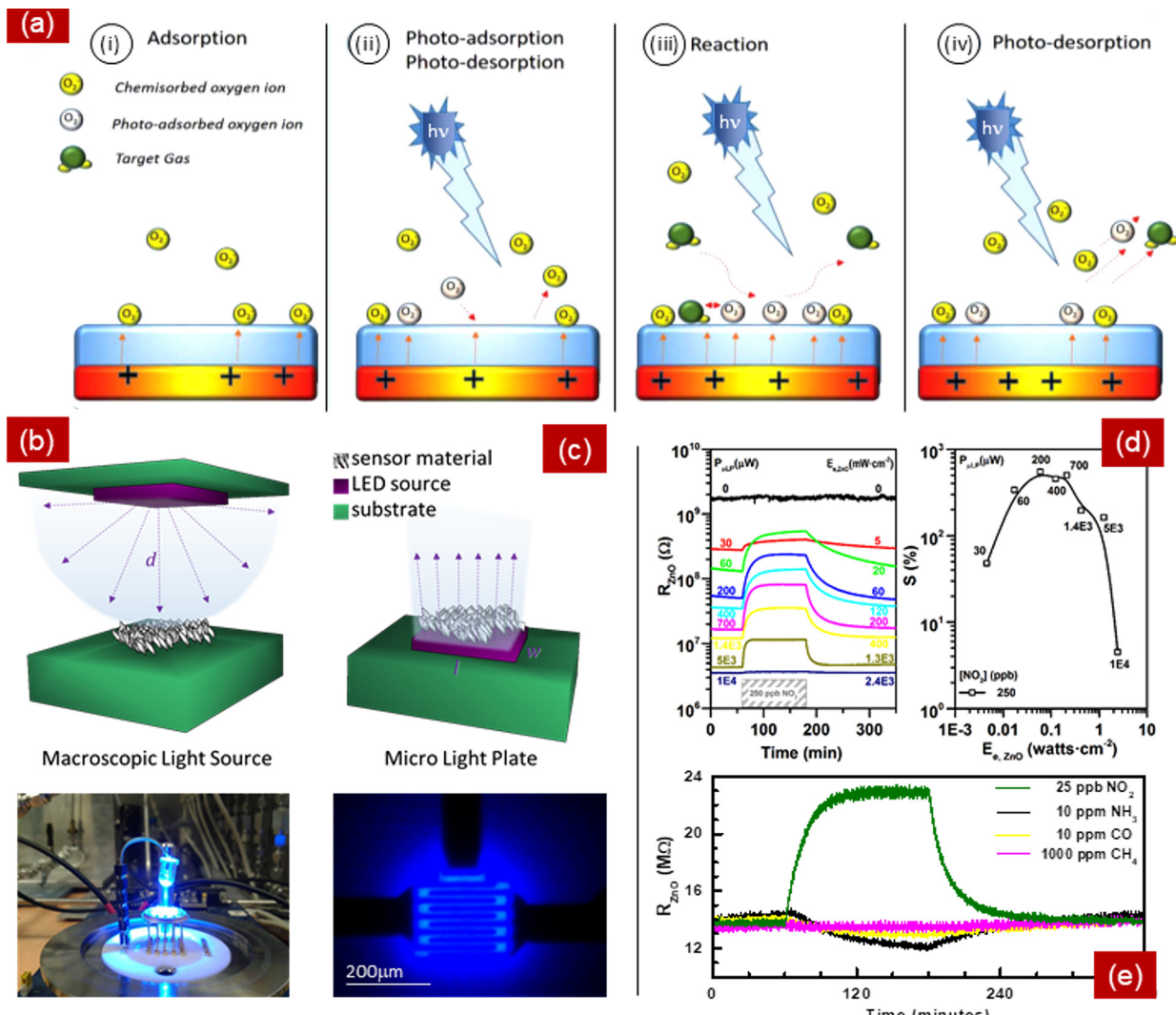


**FIG. 16.** (a) Chemical sensing mechanisms occurring under photoactivation. Photons promote (ii) photoadsorption and photodesorption of oxygen species from the sensor material surface that bring the sensor to a surface equilibrium state with oxygen in air different than that found (i) in dark conditions at room temperature. In the presence of target molecules, (iii) photons enable additional reaction mechanisms between these molecules, oxygen and the sensor surface. Also, (iv) photons can promote continuous desorption of target species. By combining these concurrent mechanisms, continuous charge exchanges between the semiconductor surface and the target molecules are enabled. Reproduced with permission from Espid and Taghipour, *Crit. Rev. Solid State Mater. Sci.* **42**(5), 416–432 (2017). Copyright 2017 Taylor & Francis Ltd.<sup>415</sup> Schematic and pictures of (b) a conventional setup based on macroscopic light sources, and (c) a power-efficient miniaturized configuration based on microlight plates. Reproduced with permission from Markiewicz *et al.*, *Appl. Phys. Lett.* **114**, 053508 (2019). Copyright 2019 AIP Publishing.<sup>26</sup> (d) Example sensor signal of a semiconductor material (ZnO) exposed to  $NO_2$  under increasing light irradiances ( $E_{e,ZnO}$ ) on a microlight plate. In dark conditions, no signal in the presence of the  $NO_2$  is recorded. As soon as light impinges on the sensor material (obtained with just 30  $\mu W$  of electrical power in the microlight plate configuration), a noticeable signal develops. This signal increase continues up to a certain optimum irradiance. Higher illumination fluxes beyond this point diminish the signal, due to excessive photodesorption [mechanism (iv) in (a)]. Reproduced with permission from Markiewicz *et al.*, *Appl. Phys. Lett.* **114**, 053508 (2019). Copyright 2019 AIP Publishing.<sup>26</sup> (e) Photoactivation tends to favor the responses toward oxidizing species, opening the door to improved selectivity toward this kind of species. Reprinted with permission from Casals *et al.*, *ACS Sens.* **4**, 822 – 826 (2019). Copyright 2019 American Chemical Society.<sup>422</sup>

recorded. As a matter of fact, the nanoprobes can be spread over a region of interest and their gas-related PL signal collected (or imaged) from a broad area. This approach allows for mapping the presence of chemicals either in gas phase or in liquids, including biocompatible applications. Also, the possibilities of band engineering in GaN-related

technologies (like InGaN) allow for stacking a number of PL regions and tuning their respective emission peaks to optimize their detection, and discrimination. In summary, this is a nice example on how recent developments in GaN processing open the door to new, very flexible, chemical transduction methods.

Of course, the integration of this kind of optochemical sensor is challenging, as it involves a light source for PL excitation, a filter for spectral separation, and an optical detector for PL signal integration. In this context, LED miniaturization can contribute positively in the future; for example following approaches similar to the microlight plates: A PL excitation source cut to size and placed at a very close distance of the PL-emitting sensor material would maximize the optical coupling and thus the PL-signal. Also, power consumption would directly downscale with the active area of the resulting device. Moreover, size reduction can also contribute to speed up the LED switching times, by reducing the parasitic capacities related to the LED area, enabling faster switching rates (e.g., down to the range of a few nanoseconds). This would open the door to use time-gated detection methods<sup>178,179</sup> that can save the need for optical filters to separate excitation from emission at the detector side, simplifying the embodiment of this type of sensor.

### 3. Airborne micro-/nanoparticle sensors

Airborne particles (aerosols) or particulate matter (PM), which are ubiquitous in both outdoor and indoor workplaces, may produce risks and potential adverse health effects, in particular of pulmonary diseases, for workers.<sup>133</sup> In the case of unexpected excessive concentrations of hazardous particles, the potentially exposed persons should be equipped with a personal portable airborne particle detector to prevent an overexposure; hence they can leave the rooms immediately once the sensors provide a warning signal or an alert because the upper concentration limit of particle exposure has been reached. In the aerosol community, the metrics that should be measured for such airborne particles are still debatable (i.e., either mass or number concentration of particles) considering the research results from the medical and biological scientists on the toxicity effects of particles affected by those two different parameters, besides the particles size. However, by doing calibration with other monitoring instrument, both metrics could be obtained with a few deviations because of the used approximation for transferring or calculating the detected particle number concentration (i.e., normally in particles/cm<sup>3</sup>) to particle mass concentration (i.e., usually in microgram per cubic meter), or vice versa.<sup>140,434,435</sup> Among other portable airborne particle sensors of different measurement principles [e.g., unipolar diffusion charger combined with electrometer,<sup>436–438</sup> CMOS-compatible capacitive microsensors,<sup>439</sup> gravimetric sensors based on micro-/nanoelectromechanical systems (MEMS/NEMS)<sup>434,440–453</sup>] optical sensors have attracted more attention in recent years as a consequence of recent advanced developments of optoelectronic components (e.g., micro-LED arrays) and their capability of having high-speed detection (nanosecond–millisecond).<sup>140,201,247,303,454–457</sup> Moreover, they do not need to be cleaned so frequently like the case of MEMS/NEMS sensors overloaded with particles after several hours of particle sampling,<sup>434,447,458–461</sup> which leads to the possibility of using optical sensors for long-term particle exposure assessments. The stereotypes of optical methods as expensive, bulky, and complicated airborne particle sensors like in the commercially available scanning mobility particle sizer (SMPS) or condensation particle counter (CPC) have therefore been eliminated.<sup>462–464</sup> In the SMPS spectrometer, particle size distribution with ranging from 3 nm to 1 μm can be measured by combining electrical mobility separation and laser diode-based optical sensing methods, where a

light-scattering technique is implemented to detect the particle droplets [i.e., nanoparticles that have been condensed or grown to micrometer sized particles (about 10 μm)]. The signal conversion from the adsorbed light to an electric pulse is performed by a photodetector, which is then recorded as a particle count. The whole particle size distributions can be scanned and measured by continuously ramping up the applied high voltage in the differential mobility analyzer electrode or the electrical field over a selected period of time.<sup>435,464,465</sup>

The latest developed optical sensors for airborne microparticle detection are based on lensless microscopy using visible LED arrays<sup>140,201,247,455–457</sup> and fluorescence spectroscopy,<sup>305,454</sup> which are made in a more compact and portable architecture, as the geometry and functionality of light sources (i.e., micro-LED array with individually controlled pixels) can be tailored specifically to the desired tasks and final designs of the whole sensor apparatus. Moreover, their much reduced size and fabrication cost have provided more advantages over conventional laser-based induced fluorescence systems utilizing solid-state lasers.<sup>466,467</sup> Total footprints of approximately 20 cm × 13 cm and 25 cm × 35 cm have been reported for spectral-filter [Fig. 17(a)] and spectroscopic fluorescence [Fig. 17(b)] detection systems using lenses, respectively.<sup>305,454</sup> In those setups, 32 UV LEDs are arranged in a linear array with a pixel size of 200 μm × 50 μm and pitch of 100 μm, yielding a total array length of approximately 3.2 mm. Each of the 32 LEDs of the array is individually addressable while sharing a common *n*-electrode. In general, for biological targets (i.e., bioaerosols or particles), UV LEDs are more exciting due to the fact that typical biological materials containing molecules (e.g., the amino acids tryptophan and tyrosine) exhibit light absorption only below 300 nm, whereas the nicotinamide adenine dinucleotide (NADH) has local absorption at maximum 340 nm. Those compounds possess characteristic fluorescence emission spectra, which can lead to discrimination between particles of targeted biological and nontargeted nonbiological origins.<sup>468,469</sup> Thus, two different UV micro-LED arrays with wavelengths of 290 nm and 340 nm [Figs. 17(c) and 17(d)] were designed and fabricated from MOCVD-grown AlGaN and AlGaInN, quantum-well *p*-*n* junction heterostructures, respectively,<sup>470,471</sup> to target tryptophan and NADH fluorescence [Figs. 17(e) and 17(f)].<sup>305</sup> Prior to demonstration of the UV micro-LED array for airborne microparticle detection, InGaN blue LED arrays were also reported,<sup>472</sup> in which the microlens array was coupled onto the top-side emission of blue LEDs (semitransparent *p*-electrode) individually for enhancing the light extraction. However, for the UV micro-LEDs, the light extraction was performed through the transparent sapphire backside. An opaque metal stack of Ni/Au was employed as *p*-contact, and the LED array was bonded onto a structured silicon submount via flip-chip bonding method using electrically and thermally conductive epoxies for obtaining electrical contact and thermal management, respectively. In addition to it, a single hyper-hemispherical sapphire lens covering the entire LED array was integrated onto the polished backside with refractive index of  $n = 1.56$  UV-transparent epoxy [Fig. 17(d)]. As the detector part of the system, a transmission grating has been combined with multianode photomultiplier (PMT) for acquiring 32-point spectra.<sup>305</sup>

Taking advantage of having simpler but powerful lensless architecture (i.e., entirely without objective lenses), the holographic microscope can be shrunk down to smartphone sizes or even smaller, leading to the possibility of making label-free single particle on-chip

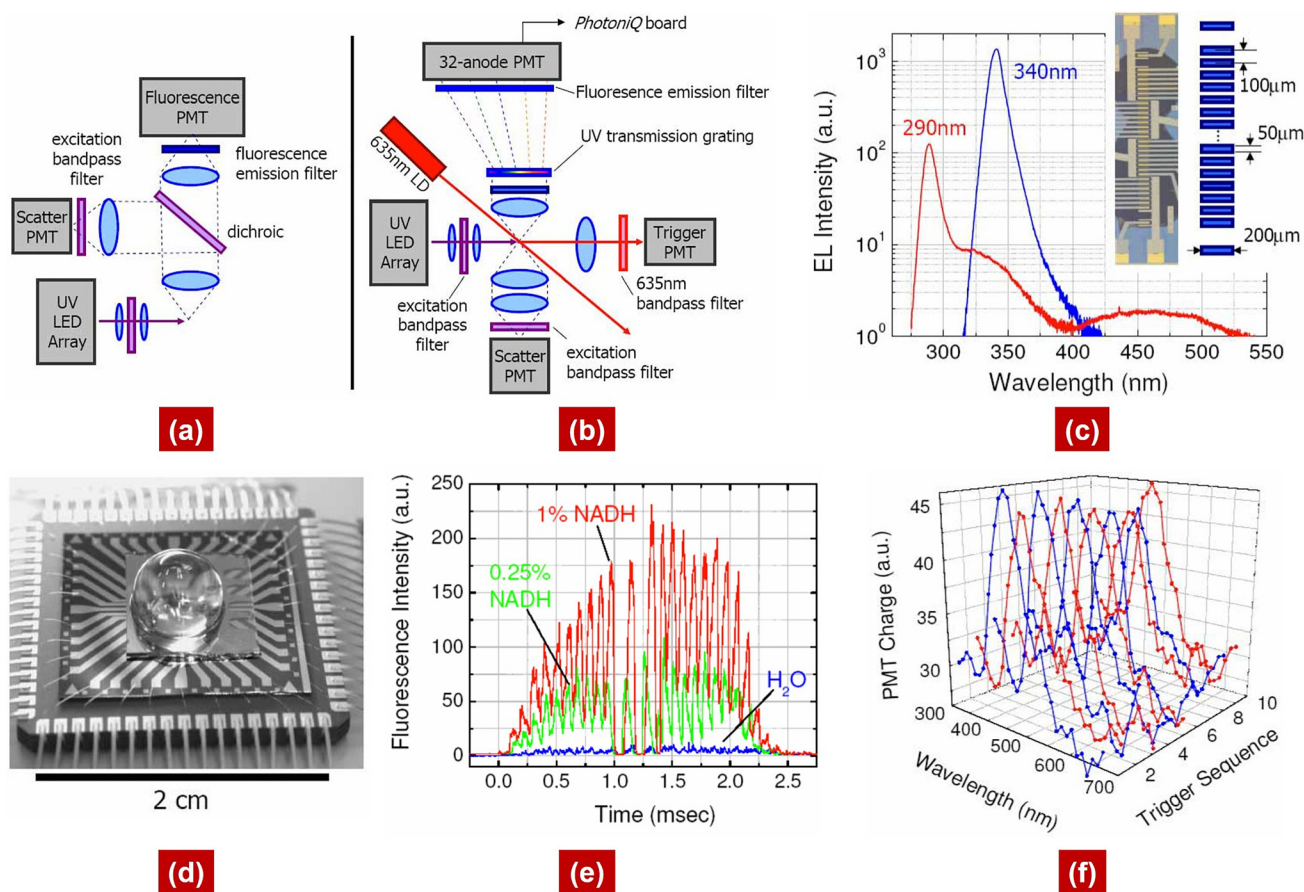


**FIG. 17.** Top-view setups of compact UV LED array-based airborne particle detection systems using (a) optical filters and (b) spectroscopic fluorescence detection. (c) Typical electroluminescence spectra of employed LED elements of 290 nm and 340 nm linear arrays under  $1\text{ kA/cm}^2$  injection current. Each LED pixel can be switched on and off after one to the others. (d) Photograph of packaged UV micro-LED array covered by lens. (e) Optical filter-based system response to fluorophore-doped water droplets showing real-time fluorescence channel recordings for single nicotinamide adenine dinucleotide (NADH) particles. (f) Ten single particle fluorescence spectra collected from ten successive particles of 0.025% NADH illuminated by a sequentially firing 340 nm UV LED array. Reproduced with permission from Davitt *et al.*, Opt. Express **13**, 9548 (2005). Copyright 2005 Author(s), licensed under a Creative Commons Attribution 4.0 License.

microscopes [Figs. 18(a)–18(d)].<sup>140,201,207,456</sup> The key component behind these microscopes is a small coherent, or partially coherent, light source, which is employed to illuminate a transmissive sample where the particles are collected using mechanical impaction method [Fig. 18(a)]. The interference between undisturbed light passing straight through the sample and the light scattered off by the objects on the sample creates a fringe pattern that can be directly captured by the image sensor located close to the sample holder. To reconstruct the original object, computational backpropagation of this recorded fringe pattern can be done. Phase recovery methods can then be introduced to this lensless holographic computational microscopy approach to realize a greater degree of robustness in the imaged samples. For the reported LED-based lensfree holographic on-chip microscope for air quality monitoring,<sup>140</sup> this compact system combines a micropump, an impaction-based air-sampler and a lens-free holographic on-chip microscope, and a custom-written software based on machine learning algorithm for remote data processing and particle analysis [Fig. 18(b)].

From the reported experiments, this device can have an airborne particle flow of  $13\text{ l/min}$  with particle sizing distribution accuracy of up to  $\sim 93\%$ , providing highly sensitive and rapid measurements of particle counts at low concentrations in air. From a slightly different setup, one of the smallest computational holographic LED microscopes that can be used for airborne nanoparticle detection has been demonstrated with a weight of  $145\text{ g}$  and a dimension of  $17\text{ cm} \times 6\text{ cm} \times 5\text{ cm}$ , which is suitable for field settings and point-of-care use, because the device can be brought outside the labs easily.<sup>207</sup> In this setup [Fig. 18(c)], the colorization algorithm with a source shifting based multiheight pixel superresolution technique has been merged to mitigate “rainbow”-like color artifacts that are typical in holographic imaging. Moreover, LED arrays with wavelengths of 624 nm (red), 527 nm (green), and 470 nm (blue) have been coupled with optical fiber to realize point-light sources in holographic detection systems. By using such mini systems, the sizing of individual nanoparticles as well as viruses, monodisperse particle samples, and complex polydisperse

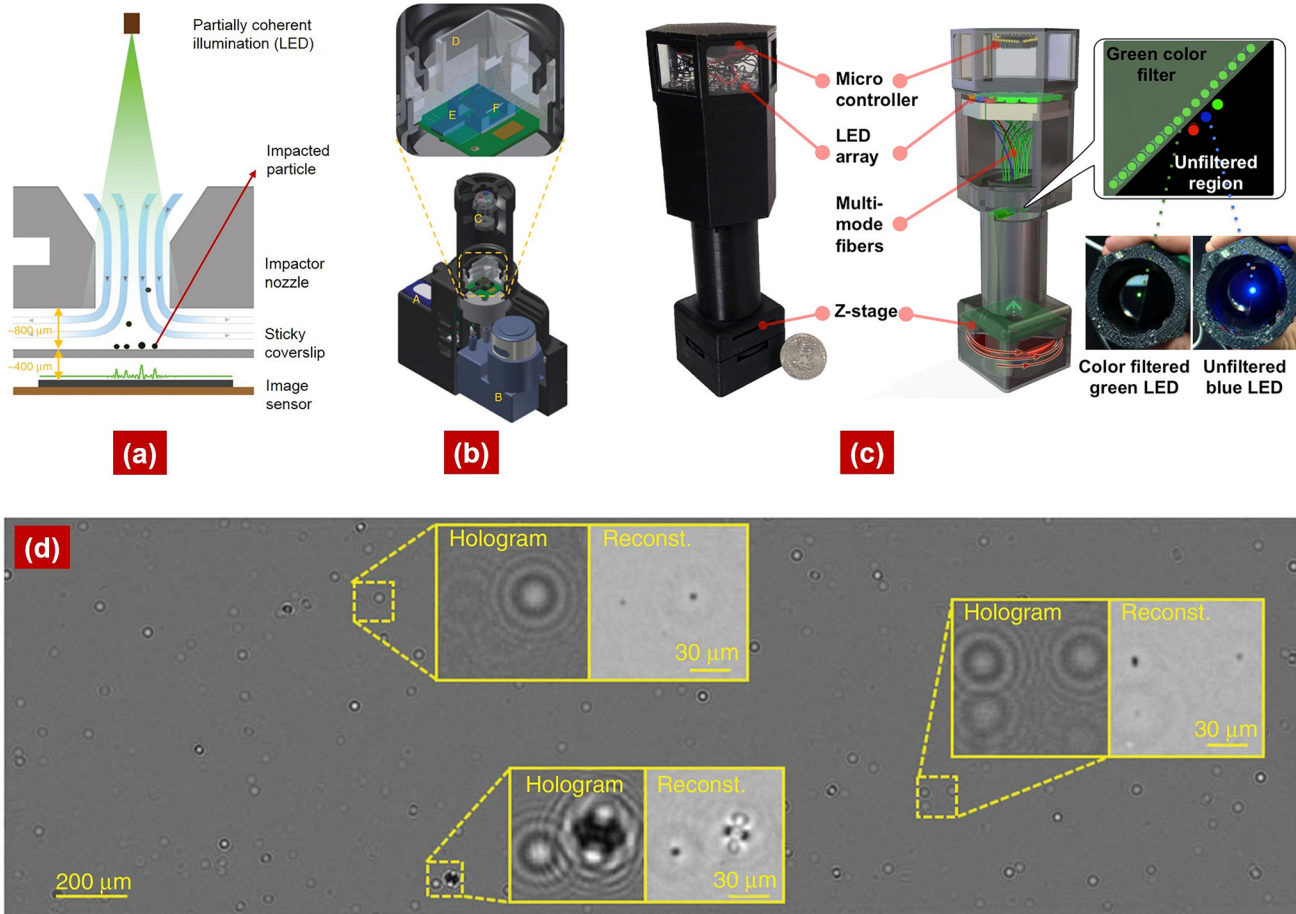


**FIG. 18.** (a) 2D and (b) 3D computer-aided-design (CAD) schematic drawings of lensfree holographic on-chip microscope for airborne microparticle detection showing (A) rechargeable battery, (B) vacuum pump, (C) point-light sources consisting of fiber-coupled LEDs of red (624 nm), green (527 nm) and blue (470 nm), (D) mechanical impactor for airborne particle sampling, (E) a sticky coverslip to place the impacted particles, and (F) the image sensor. Reprinted with permission from Wu *et al.* *Light: Sci. Appl.* **6**(9), e17046 (2017). Copyright 2017 Springer Nature.<sup>140</sup> (c) Another type of portable lensfree super-resolution microscope with colorization algorithm having a weight of  $\sim$ 145 grams and two separate LED array groups. The first LED array contains 17 green LEDs butt-coupled to a multimode fiber where its emission passes through a color filter for enabling pixel super-resolution based on source shifting. The second LED array is composed of three LEDs (470 nm, 527 nm, and 625 nm) is used for enabling the acquisition of a lower resolution color image. Reproduced with permission from Greenbaum *et al.*, *PLoS One* **8**, e76475 (2013).<sup>207</sup> Copyright 2013 Author(s), licensed under a Creative Commons Attribution 4.0 License. (d) Recorded hologram image of impacted airborne microparticles during sampling and its reconstructed results. Reprinted with permission from Wu *et al.* *Light: Sci. Appl.* **6**(9), e17046 (2017). Copyright 2017 Springer Nature.<sup>140</sup>

particle mixtures (5 orders-of-magnitude higher number concentration), can be resolved with a large particle size distribution range (from 40 nm to millimeter-scale).<sup>456</sup> Meanwhile, a similar setup has been employed for real-time mapping of the air quality at an air quality monitoring station approved by United States Environmental Protection Agency (EPA) and in one of the United States airports over 24 h demonstrating the robustness of LED-based optical particle sensors [Figs. 18(d)].<sup>140</sup>

As a main component for optical particle detectors,  $\mu$ LEDs bring in novel functions and enhanced performance, e.g., hybrid or monolithic integration with CMOS electronics will be made feasible. In addition, for the holography-based lensless particle sensor, the use of micro-LEDs enhances the spatial coherence length of the light source, thus acting as a better point illumination source, in comparison with

commercially available large-sized LEDs, which leads to a quality improvement of the obtained microscopy images of the deposited particles on the sample object.<sup>169,176</sup>

#### IV. CONCLUSION

We are presently witnessing a tremendous extension of GaN based photonics, based on the fascinating success of solid-state lighting technology and InGaN/GaN LEDs. GaN based LEDs offer highest efficiency even when processed into micro- and nanoscale devices. This opens up many new directions for research as well as application. Based on the amazing cost reduction in GaN technology, it is quite safe to expect that GaN micro-LED displays will be superior to LCD and OLED displays, leading to a disruptive revolution in display technology. GaN micro-LED displays are at the same time very interesting

for small displays, like their usage in augmented reality applications; highest efficiency and highest brightness is expected to finally lead to best performance. However, GaN micro-LED applications will move far beyond that. There are many other fields where GaN micro-LEDs are of particular advantage. They will serve as an enabler for highly integrated microsensors with optical activation of gas reactions, act as the main component for biological detectors and optogenetics, and possibly even be the basis for a completely new type of superresolution microscopy based on nano-LED arrays. All that will only become reality if further research will be devoted to the miniaturization of GaN micro-LEDs and their integration into sensors as well as into silicon microelectronics. Such an integration will also have substantial impact on GaN high-frequency (HF) and power electronics research (which, however, has not been in the scope of this review). Appropriate research efforts have to combine epitaxy, nanometrology, and chip processing as well as CMOS design at the highest level, and with highest precision. This imposes substantial challenges on research infrastructure, calling for new and comprehensive research strategies.

## ACKNOWLEDGMENTS

The authors would like to thank their co-workers of the many joint projects, who have carried micro-LED research on over the past years at both our affiliations. The support of the epitaxy competence center (ec<sup>2</sup>) and the collaboration with Osram Opto Semiconductors GmbH, Regensburg, Germany are gratefully acknowledged. The core projects have been the European project of ChipScope funded by the European Union's Horizon 2020 research and innovation program under Grant Agreement No. 737089, the European Union's Seventh Framework Program (No. FP/2007-2013)/ERC Grant Agreement No. 336917 funded by the European Research Council, and the incubation project "Superlight Photonics" funded by the German Federal Ministry of Education and Research (BMBF). H. S. Wasisto would like to thank the Lower Saxony Ministry for Science and Culture (N-MWK) for funding the junior research group LENA-OptoSense and the Directorate General of Higher Education, Science, and Technology Resources (Ditjen SDID) from the Ministry of Research, Technology and Higher Education of the Republic of Indonesia (RISTEKDIKTI) for providing excellent Indonesian diaspora platforms of World-Class Scholar Symposium [Simposium Cendekia Kelas Dunia (SCKD)] and Indonesian-German Center for Nano and Quantum Technologies (IG-Nano). J. D. Prades acknowledges the support from the Serra Húnter Program and the ICREA Academia programme; and together with A. Waag, the German Research Foundation (DFG) Project GrK NanoMet. A. Waag and J. Gülink would like to thank the Excellence Clusters QuantumFrontiers and PhoenixD, where part of the more recent work has been performed.

## REFERENCES

- <sup>1</sup>H. Amano, M. Kito, K. Hiramatsu, and I. Akasaki, "P-type conduction in Mg-doped GaN treated with low-energy electron beam irradiation (LEEBI)," *Jpn. J. Appl. Phys., Part 2* **28**(12), L2112–L2114 (1989).
- <sup>2</sup>E. F. Schubert and J. K. Kim, "Solid-state light sources getting smart," *Science* **308**(5726), 1274–1278 (2005).
- <sup>3</sup>T. Hager *et al.*, "Power blue and green laser diodes and their applications," *SPIE Proc.* **8640**, 86400G (2013).
- <sup>4</sup>S. Li and A. Waag, "GaN based nanorods for solid state lighting," *J. Appl. Phys.* **111**(7), 071101 (2012).
- <sup>5</sup>Gallium Nitride-Enabled High Frequency and High Efficiency Power Conversion (Integrated Circuits and Systems), 1st ed., edited by G. Meneghesso, M. Meneghini, and E. Zanoni (Springer, 2018).
- <sup>6</sup>M. F. Fatahilah *et al.*, "Top-down GaN nanowire transistors with nearly zero gate hysteresis for parallel vertical electronics," *Sci. Rep.* **9**(1), 1–11 (2019).
- <sup>7</sup>F. Yu *et al.*, "Normally off vertical 3-D GaN nanowire MOSFETs with inverted p-GaN channel," *IEEE Trans. Electron Devices* **65**(6), 2439–2445 (2018).
- <sup>8</sup>M. F. Fatahilah, K. Stremmel, F. Yu, S. Vodapally, A. Waag, and H. S. Wasisto, "3D GaN nanoarchitecture for field-effect transistors," *Micro Nano Eng.* **3**, 59–81 (2019).
- <sup>9</sup>B. Hahn, B. Galler, and K. Engl, "Development of high-efficiency and high-power vertical light emitting diodes," *Jpn. J. Appl. Phys., Part 1* **53**(10), 100208 (2014).
- <sup>10</sup>Navigant Consulting, Inc., [https://www.energy.gov/sites/prod/files/2016/09/f33/energysavingsforecast16\\_2.pdf](https://www.energy.gov/sites/prod/files/2016/09/f33/energysavingsforecast16_2.pdf) for "Energy savings forecast of solid-state lighting in general applications" (2016); accessed 3 November 2019.
- <sup>11</sup>Cree, Inc., <https://www.cree.com/news-media/news/article/cree-first-to-break-300-lumens-per-watt-barrier> for "Cree first to break 300 lumens-per-watt barrier" (2014); accessed 27 September 2019.
- <sup>12</sup>M. Tchernycheva *et al.*, "Integrated photonic platform based on InGaN/GaN nanowire emitters and detectors," *Nano Lett.* **14**(6), 3515–3520 (2014).
- <sup>13</sup>S. Li *et al.*, "GaN nanorods and LED structures grown on patterned Si and AlN/Si substrates by selective area growth," *Phys. Status Solidi* **7**(7–8), 2224–2226 (2010).
- <sup>14</sup>F. Yu *et al.*, "GaN nanowire arrays with nonpolar sidewalls for vertically integrated field-effect transistors," *Nanotechnology* **28**(9), 95206 (2017).
- <sup>15</sup>M. Sun, Y. Zhang, X. Gao, and T. Palacios, "High-performance GaN vertical Fin power transistors on bulk GaN substrates," *IEEE Electron Device Lett.* **38**(4), 509–512 (2017).
- <sup>16</sup>M. K. Kelly, R. P. Vaudo, V. M. Phanse, L. Goergens, O. Ambacher, and M. Stutzmann, "Large free-standing GaN substrates by hydride vapor phase epitaxy and laser-induced lift-off," *Jpn. J. Appl. Phys.* **38**, L217–L219 (1999).
- <sup>17</sup>J. W. Chung, B. Lu, and T. Palacios, "On-wafer seamless integration of GaN and Si (100) electronics," in Technical Digest - IEEE Compound Semiconductor Integrated Circuit Symposium, CSIC (2009).
- <sup>18</sup>J. Herrnsdorf *et al.*, "Active-matrix GaN micro light-emitting diode display with unprecedented brightness," *IEEE Trans. Electron Devices* **62**(6), 1918–1925 (2015).
- <sup>19</sup>F. Templier, "GaN-based emissive microdisplays: A very promising technology for compact, ultra-high brightness display systems," *J. Soc. Inf. Disp.* **24**(11), 669–675 (2016).
- <sup>20</sup>C.-M. Kang *et al.*, "Hybrid full-color inorganic light-emitting diodes integrated on a single wafer using selective area growth and adhesive bonding," *ACS Photonics* **5**(11), 4413–4422 (2018).
- <sup>21</sup>R. T. Azuma, "A survey of augmented reality," *Presence Teleoperators Virtual Environ.* **6**(4), 355–385 (1997).
- <sup>22</sup>D. Tsonev *et al.*, "A 3-Gb/s single-LED OFDM-based wireless VLC link using a gallium nitride μLED," *IEEE Photonics Technol. Lett.* **26**(7), 637–640 (2014).
- <sup>23</sup>J. D. McKendry *et al.*, "High-speed visible light communications using individual pixels in a micro light-emitting diode array," *IEEE Photonics Technol. Lett.* **22**(18), 1346–1348 (2010).
- <sup>24</sup>R. X. G. Ferreira *et al.*, "High bandwidth GaN-based micro-LEDs for multi-Gb/s visible light communications," *IEEE Photonics Technol. Lett.* **28**(19), 2023–2026 (2016).
- <sup>25</sup>ChipScope, <http://www.chipscope.eu/> for "Overcoming the limits of diffraction with super-resolution lighting on a chip (ChipScope EU Project)" (2019); accessed 4 November 2019.
- <sup>26</sup>N. Markiewicz *et al.*, "Micro light plates for low-power photoactivated (gas) sensors," *Appl. Phys. Lett.* **114**(5), 053508 (2019).
- <sup>27</sup>I. M. Watson, "Metal organic vapour phase epitaxy of AlN, GaN, InN and their alloys: A key chemical technology for advanced device applications," *Coord. Chem. Rev.* **257**(13–14), 2120–2141 (2013).

- <sup>28</sup>W. V. Lundin, A. V. Sakharov, A. F. Tsatsulnikov, and V. M. Ustinov, "MOVPE of device-oriented wide-band-gap III-N heterostructures," *Semicond. Sci. Technol.* **26**(1), 014039 (2011).
- <sup>29</sup>H. Amano, "MOCVD of nitrides," *Handbook of Crystal Growth*, 2nd ed., Vol. III, Part A, Chap. 16 (Elsevier, 2015), pp. 683–704.
- <sup>30</sup>D. Feezell and S. Nakamura, "Invention, development, and status of the blue light-emitting diode, the enabler of solid-state lighting," *C. R. Phys.* **19**(3), 113–133 (2018).
- <sup>31</sup>J. Cho, J. H. Park, J. K. Kim, and E. F. Schubert, "White light-emitting diodes: History, progress, and future," *Laser Photonics Rev.* **11**(2), 1600147 (2017).
- <sup>32</sup>M. Malinverni, D. Martin, and N. Grandjean, "InGaN based micro light emitting diodes featuring a buried GaN tunnel junction," *Appl. Phys. Lett.* **107**(5), 051107 (2015).
- <sup>33</sup>F. B. Naranjo, S. Fernández, M. A. Sánchez-García, F. Calle, and E. Calleja, "Resonant-cavity InGaN multiple-quantum-well green light-emitting diode grown by molecular-beam epitaxy," *Appl. Phys. Lett.* **80**(12), 2198–2200 (2002).
- <sup>34</sup>OSRAM-Group, <https://www.osram-group.com/en/media/press-releases/pr-2014/28-03-2014> for "Osram constructs the world's most efficient LED lamp," Press Release (2019); accessed 24 February 2019.
- <sup>35</sup>S. Nakamura, "The roles of structural imperfections in InGaN-based blue light-emitting diodes and laser diodes," *Science* **281**(5379), 956–961 (1998).
- <sup>36</sup>J.-I. Hwang, R. Hashimoto, S. Saito, and S. Nunoue, "Development of InGaN-based red LED grown on (0001) polar surface," *Appl. Phys. Express* **7**(7), 071003 (2014).
- <sup>37</sup>T.-J. Yang, R. Shivaraman, J. S. Speck, and Y.-R. Wu, "The influence of random indium alloy fluctuations in indium gallium nitride quantum wells on the device behavior," *J. Appl. Phys.* **116**(11), 113104 (2014).
- <sup>38</sup>J. Iveland, L. Martinelli, J. Peretti, J. S. Speck, and C. Weisbuch, "Direct measurement of auger electrons emitted from a semiconductor light-emitting diode under electrical injection: Identification of the dominant mechanism for efficiency droop," *Phys. Rev. Lett.* **110**(17), 177406 (2013).
- <sup>39</sup>B. Galler *et al.*, "Experimental determination of the dominant type of auger recombination in InGaN quantum wells," *Appl. Phys. Express* **6**(11), 112101 (2013).
- <sup>40</sup>G. Verzellesi *et al.*, "Efficiency droop in InGaN/GaN blue light-emitting diodes: Physical mechanisms and remedies," *J. Appl. Phys.* **114**(7), 071101 (2013).
- <sup>41</sup>S. F. Chichibu *et al.*, "Origin of defect-insensitive emission probability in In-containing (Al,In,Ga)N alloy semiconductors," *Nat. Mater.* **5**(10), 810–816 (2006).
- <sup>42</sup>A. Hangleiter *et al.*, "Suppression of nonradiative recombination by V-shaped pits in GaInN/GaN quantum wells produces a large increase in the light emission efficiency," *Phys. Rev. Lett.* **95**(12), 127402 (2005).
- <sup>43</sup>R. M. Farrell, E. C. Young, F. Wu, S. P. DenBaars, and J. S. Speck, "Materials and growth issues for high-performance nonpolar and semipolar light-emitting devices," *Semicond. Sci. Technol.* **27**(2), 024001 (2012).
- <sup>44</sup>F. Nippert *et al.*, "Temperature-dependent recombination coefficients in InGaN light-emitting diodes: Hole localization, Auger processes, and the green gap," *Appl. Phys. Lett.* **109**(16), 161103 (2016).
- <sup>45</sup>M. Binder *et al.*, "Identification of nnp and npp Auger recombination as significant contributor to the efficiency droop in (GaIn)N quantum wells by visualization of hot carriers in photoluminescence," *Appl. Phys. Lett.* **103**(7), 071108 (2013).
- <sup>46</sup>X. A. Cao *et al.*, "Blue and near-ultraviolet light-emitting diodes on free-standing GaN substrates," *Appl. Phys. Lett.* **84**(21), 4313–4315 (2004).
- <sup>47</sup>M. Kneissl and J. Rass, *III-Nitride Ultraviolet Emitters* (Springer International Publishing, Cham, 2016), Vol. 227.
- <sup>48</sup>M. Kneissl *et al.*, "Advances in group III-nitride-based deep UV light-emitting diode technology," *Semicond. Sci. Technol.* **26**(1), 014036 (2011).
- <sup>49</sup>M. Bickermann *et al.*, "Deep-UV transparent bulk single-crystalline AlN substrates," *Phys. Status Solidi* **7**(7–8), 1743–1745 (2010).
- <sup>50</sup>Z. Bryan, I. Bryan, S. Mita, J. Tweedie, Z. Sitar, and R. Collazo, "Strain dependence on polarization properties of AlGaN and AlGaN-based ultraviolet lasers grown on AlN substrates," *Appl. Phys. Lett.* **106**(23), 232101 (2015).
- <sup>51</sup>A. Sedhain, L. Du, J. H. Edgar, J. Y. Lin, and H. X. Jiang, "The origin of 2.78 eV emission and yellow coloration in bulk AlN substrates," *Appl. Phys. Lett.* **95**(26), 262104 (2009).
- <sup>52</sup>See <http://www.qubedot.com> for "QubeDot" (2019); accessed 4 November 2019.
- <sup>53</sup>A. Jaros *et al.*, "Photoluminescence of planar and 3D InGaN/GaN LED structures excited with femtosecond laser pulses close to the damage threshold," *Sci. Rep.* **8**(1), 1–8 (2018).
- <sup>54</sup>Y. Narukawa *et al.*, "White light emitting diodes with super-high luminous efficacy," *J. Phys. D: Appl. Phys.* **43**, 354002 (2010).
- <sup>55</sup>J. L. Liu *et al.*, "Status of GaN-based green light-emitting diodes," *Chin. Phys. B* **24**(6), 067804 (2015).
- <sup>56</sup>Y. Zhao, H. Fu, G. T. Wang, and S. Nakamura, "Toward ultimate efficiency: Progress and prospects on planar and 3D nanostructured nonpolar and semipolar InGaN light-emitting diodes," *Adv. Opt. Photonics* **10**(1), 246 (2018).
- <sup>57</sup>J. Chen, S. Loeb, and J. H. Kim, "LED revolution: Fundamentals and prospects for UV disinfection applications," *Environ. Sci. Water Res. Technol.* **3**(2), 188–202 (2017).
- <sup>58</sup>Y. Nagasawa and A. Hirano, "A review of AlGaN-based deep-ultraviolet light-emitting diodes on sapphire," *Appl. Sci.* **8**(8), 1264 (2018).
- <sup>59</sup>Y. Taniyasu, M. Kasu, and T. Makimoto, "An aluminium nitride light-emitting diode with a wavelength of 210 nanometres," *Nature* **441**(7091), 325–328 (2006).
- <sup>60</sup>N. F. Gardner *et al.*, "Blue-emitting InGaN–GaN double-heterostructure light-emitting diodes reaching maximum quantum efficiency above 200 A/cm<sup>2</sup>," *Appl. Phys. Lett.* **91**(24), 243506 (2007).
- <sup>61</sup>Y.-L. Li, Y.-R. Huang, and Y.-H. Lai, "Efficiency droop behaviors of InGaN/GaN multiple-quantum-well light-emitting diodes with varying quantum well thickness," *Appl. Phys. Lett.* **91**(18), 181113 (2007).
- <sup>62</sup>L. Wang *et al.*, "Study on injection efficiency in InGaN/GaN multiple quantum wells blue light emitting diodes," *Appl. Phys. Express* **1**, 021101 (2008).
- <sup>63</sup>R. A. Arif, Y.-K. Ee, and N. Tansu, "Polarization engineering via staggered InGaN quantum wells for radiative efficiency enhancement of light emitting diodes," *Appl. Phys. Lett.* **91**(9), 091110 (2007).
- <sup>64</sup>S.-H. Park, D. Ahn, J. Park, and Y.-T. Lee, "Optical properties of staggered InGaN/InGaN/GaN quantum-well structures with Ga- and N-faces," *Jpn. J. Appl. Phys., Part 1* **50**(7), 072101 (2011).
- <sup>65</sup>X. Ni, Q. Fan, R. Shimada, Ü. Özgür, and H. Morkoç, "Reduction of efficiency droop in InGaN light emitting diodes by coupled quantum wells," *Appl. Phys. Lett.* **93**(17), 171113 (2008).
- <sup>66</sup>W. Lv *et al.*, "InGaN quantum dot green light-emitting diodes with negligible blue shift of electroluminescence peak wavelength," *Appl. Phys. Express* **7**(2), 025203 (2014).
- <sup>67</sup>M.-H. Kim *et al.*, "Origin of efficiency droop in GaN-based light-emitting diodes," *Appl. Phys. Lett.* **91**(18), 183507 (2007).
- <sup>68</sup>S.-H. Park, D. Ahn, B.-H. Koo, and J.-W. Kim, "Electronic and optical properties of staggered InGaN/InGaN quantum-well light-emitting diodes," *Phys. Status Solidi* **206**(11), 2637–2640 (2009).
- <sup>69</sup>H. Masui, S. Nakamura, S. P. DenBaars, and U. K. Mishra, "Nonpolar and semipolar III-nitride light-emitting diodes: Achievements and challenges," *IEEE Trans. Electron Devices* **57**(1), 88–100 (2010).
- <sup>70</sup>S.-C. Ling, T.-C. Lu, S.-P. Chang, J.-R. Chen, H.-C. Kuo, and S.-C. Wang, "Low efficiency droop in blue-green m-plane InGaN/GaN light emitting diodes," *Appl. Phys. Lett.* **96**(23), 231101 (2010).
- <sup>71</sup>M. Monavarian *et al.*, "A decade of nonpolar and semipolar III-nitrides: A review of successes and challenges," *Phys. Status Solidi A* **216**, 1800628 (2019).
- <sup>72</sup>H.-S. Chen *et al.*, "Surface plasmon coupled light-emitting diode with metal protrusions into p-GaN," *Appl. Phys. Lett.* **102**(4), 041108 (2013).
- <sup>73</sup>C.-F. Lu, C.-H. Liao, C.-Y. Chen, C. Hsieh, Y.-W. Kiang, and C. C. Yang, "Reduction in the efficiency droop effect of a light-emitting diode through surface plasmon coupling," *Appl. Phys. Lett.* **96**(26), 261104 (2010).
- <sup>74</sup>J. J. Wierer, J. Y. Tsao, and D. S. Sizov, "Comparison between blue lasers and light-emitting diodes for future solid-state lighting," *Laser Photonics Rev.* **7**(6), 963–993 (2013).
- <sup>75</sup>L. Wang *et al.*, "A review on experimental measurements for understanding efficiency droop in InGaN-based light-emitting diodes," *Material* **10**(11), 1233 (2017).
- <sup>76</sup>Y.-S. Yoo, J.-H. Na, S. J. Son, and Y.-H. Cho, "Effective suppression of efficiency droop in GaN-based light-emitting diodes: Role of significant reduction of carrier density and built-in field," *Sci. Rep.* **6**(1), 34586 (2016).

- <sup>77</sup>P. Waltereit *et al.*, “Nitride semiconductors free of electrostatic fields for efficient white light-emitting diodes,” *Nature* **406**(6798), 865–868 (2000).
- <sup>78</sup>Y. Zhao *et al.*, “Indium incorporation and emission properties of nonpolar and semipolar InGaN quantum wells,” *Appl. Phys. Lett.* **100**(20), 201108 (2012).
- <sup>79</sup>S. Pleasants, “Overcoming the ‘green gap’,” *Nat. Photonics* **7**(8), 585–585 (2013).
- <sup>80</sup>W. G. Scheibenzuber, U. T. Schwarz, R. G. Veprek, B. Witzigmann, and A. Hangleiter, “Calculation of optical eigenmodes and gain in semipolar and nonpolar InGaN/GaN laser diodes,” *Phys. Rev. B* **80**(11), 115320 (2009).
- <sup>81</sup>D. F. Feezell, M. C. Schmidt, S. P. DenBaars, and S. Nakamura, “Development of nonpolar and semipolar InGaN/GaN visible light-emitting diodes,” *MRS Bull.* **34**(5), 318–323 (2009).
- <sup>82</sup>D. L. Becerra *et al.*, “High-power low-droop violet semipolar (303̄) InGaN/GaN light-emitting diodes with thick active layer design,” *Appl. Phys. Lett.* **105**(17), 171106 (2014).
- <sup>83</sup>K. J. Vampola *et al.*, “Highly efficient broad-area blue and white light-emitting diodes on bulk GaN substrates,” *Phys. Status Solidi* **206**(2), 200–202 (2009).
- <sup>84</sup>M. Funato *et al.*, “Blue, green, and amber InGaN/GaN light-emitting diodes on semipolar {11–22} GaN bulk substrates,” *Jpn. J. Appl. Phys., Part 2* **45**(26), L659–L662 (2006).
- <sup>85</sup>H. Sato *et al.*, “High power and high efficiency green light emitting diode on free-standing semipolar (112) bulk GaN substrate,” *Phys. Status Solidi RRL* **1**(4), 162–164 (2007).
- <sup>86</sup>H. Sato *et al.*, “High power and high efficiency semipolar InGaN light emitting diodes,” *J. Light Vis. Environ.* **32**(2), 107–110 (2008).
- <sup>87</sup>C.-C. Pan *et al.*, “High-power, low-efficiency-droop semipolar (2021) single-quantum-well blue light-emitting diodes,” *Appl. Phys. Express* **5**(6), 062103 (2012).
- <sup>88</sup>Y. Zhao *et al.*, “Green semipolar (2021) InGaN light-emitting diodes with small wavelength shift and narrow spectral linewidth,” *Appl. Phys. Express* **6**(6), 062102 (2013).
- <sup>89</sup>S. Yamamoto *et al.*, “High-efficiency single-quantum-well green and yellow-green light-emitting diodes on semipolar (2021) GaN substrates,” *Appl. Phys. Express* **3**(12), 122102 (2010).
- <sup>90</sup>Y. Zhao *et al.*, “30-mW-class high-power and high-efficiency blue semipolar (101̄1) InGaN/GaN light-emitting diodes obtained by backside roughening technique,” *Appl. Phys. Express* **3**(10), 102101 (2010).
- <sup>91</sup>Y. Zhao *et al.*, “Optimization of device structures for bright blue semipolar (101̄1) light emitting diodes via metalorganic chemical vapor deposition,” *Jpn. J. Appl. Phys., Part 1* **49**(7), 070206 (2010).
- <sup>92</sup>Y. Zhao *et al.*, “High-power blue-violet semipolar (2021) InGaN/GaN light-emitting diodes with low efficiency droop at 200 A/cm<sup>2</sup>,” *Appl. Phys. Express* **4**(8), 082104 (2011).
- <sup>93</sup>M. Monavarian *et al.*, “Impact of crystal orientation on the modulation bandwidth of InGaN/GaN light-emitting diodes,” *Appl. Phys. Lett.* **112**(4), 041104 (2018).
- <sup>94</sup>R. Koester *et al.*, “High-speed GaN/GaInN nanowire array light-emitting diode on silicon(111),” *Nano Lett.* **15**(4), 2318–2323 (2015).
- <sup>95</sup>P. Tian *et al.*, “Size-dependent efficiency and efficiency droop of blue InGaN micro-light emitting diodes,” *Appl. Phys. Lett.* **101**(23), 231110 (2012).
- <sup>96</sup>C. Shen, T. K. Ng, Y. Yang, D. Cha, and B. S. Ooi, “InGaN micro-LED-pillar as the building block for high brightness emitters,” in 2013 IEEE Photonics Conference (2013), pp. 174–175.
- <sup>97</sup>H. Kim *et al.*, “Measurements of current spreading length and design of GaN-based light emitting diodes,” *Appl. Phys. Lett.* **90**(6), 063510 (2007).
- <sup>98</sup>Y. B. Tao *et al.*, “Size effect on efficiency droop of blue light emitting diode,” *Phys. Status Solidi* **9**(3–4), 616–619 (2012).
- <sup>99</sup>V. K. Malyutenko, S. S. Bolgov, and A. D. Podoltsev, “Current crowding effect on the ideality factor and efficiency droop in blue lateral InGaN/GaN light emitting diodes,” *Appl. Phys. Lett.* **97**(25), 251110 (2010).
- <sup>100</sup>S. D. Hersee, X. Sun, and X. Wang, “The controlled growth of GaN nanowires,” *Nano Lett.* **6**(8), 1808–1811 (2006).
- <sup>101</sup>H.-M. Kim *et al.*, “High-brightness light emitting diodes using dislocation-free indium gallium nitride/gallium nitride multiquantum-well nanorod arrays,” *Nano Lett.* **4**(6), 1059–1062 (2004).
- <sup>102</sup>T. Schimpke *et al.*, “The influence of MOVPE growth conditions on the shell of core-shell GaN microrod structures,” *J. Cryst. Growth* **465**, 34–42 (2017).
- <sup>103</sup>X. Wang *et al.*, “Growth kinetics and mass transport mechanisms of GaN columns by selective area metal organic vapor phase epitaxy,” *J. Appl. Phys.* **115**, 163104 (2014).
- <sup>104</sup>J. Hartmann *et al.*, “High aspect ratio gan fin microstructures with nonpolar sidewalls by continuous mode metalorganic vapor phase epitaxy,” *Cryst. Growth Des.* **16**(3), 1458–1462 (2016).
- <sup>105</sup>T. Schimpke *et al.*, “Phosphor-converted white light from blue-emitting InGaN microrod LEDs,” *Phys. Status Solidi* **213**(6), 1577–1584 (2016).
- <sup>106</sup>J. Hartmann *et al.*, “Growth mechanisms of GaN microrods for 3D core-shell LEDs: The influence of silane flow,” *Phys. Status Solidi* **212**(12), 2830 (2015).
- <sup>107</sup>B. Monemar, B. J. Ohlsson, N. F. Gardner, and L. Samuelson, “Nanowire-based visible light emitters, present status and outlook,” *Semicond. Semimetals* **94**, 227–271 (2016).
- <sup>108</sup>W. Bergbauer *et al.*, “Continuous-flux MOVPE growth of position-controlled N-face GaN nanorods and embedded InGaN quantum wells,” *Nanotechnology* **21**(30), 305201 (2010).
- <sup>109</sup>R. Koester, J. S. Hwang, C. Durand, D. Le Si Dang, and J. Eymery, “Self-assembled growth of catalyst-free GaN wires by metal–organic vapour phase epitaxy,” *Nanotechnology* **21**(1), 015602 (2010).
- <sup>110</sup>J. Ledig *et al.*, “Characterization of the internal properties of InGaN/GaN core-shell LEDs,” *Phys. Status Solidi* **213**(1), 11–18 (2016).
- <sup>111</sup>J. Ledig *et al.*, “Electro-optical characterization of 3D-LEDs—Nondestructive inspection of 4” wafers in bird’s eye view by an FE-SEM,” *Imag. Microsc.* **18**(2), 44–46 (2016), see <https://www.imaging-git.com/science/electron-and-ion-microscopy/electro-optical-characterization-3d-leds>.
- <sup>112</sup>M. S. Mohajerani *et al.*, “Direct correlations of structural and optical properties of three-dimensional GaN/InGaN core/shell micro-light emitting diodes,” *Jpn. J. Appl. Phys.* **55**, 05FJ09 (2016).
- <sup>113</sup>J. Rass and N. Lobo-Ploch, “Optical polarization and light extraction from UV LEDs,” *III-Nitride Ultraviolet Emitters* (Springer, Cham, 2016), pp. 137–170.
- <sup>114</sup>P.-M. Coulon *et al.*, “Hybrid top-down/bottom-up fabrication of regular arrays of AlN nanorods for deep-UV core-shell LEDs,” *Phys. Status Solidi* **255**(5), 1700445 (2018).
- <sup>115</sup>P.-M. Coulon, G. Kusch, R. W. Martin, and P. A. Shields, “Deep UV emission from highly ordered AlGaN/AlN core-shell nanorods,” *ACS Appl. Mater. Interfaces* **10**(39), 33441–33449 (2018).
- <sup>116</sup>J. Hartmann *et al.*, “Study of 3D-growth conditions for selective area MOVPE of high aspect ratio GaN fins with non-polar vertical sidewalls,” *J. Cryst. Growth* **476**, 1–14 (2017).
- <sup>117</sup>M. A. M. Al-Suleiman, Y. Al-Hadeethi, and A. Waag, “Process optimization of GaN nanorods fabricated using CH<sub>4</sub>/H<sub>2</sub>/SF<sub>6</sub> inductively coupled plasma etch technology,” *Sci. Adv. Mater.* **7**(12), 2523–2527 (2015).
- <sup>118</sup>Q. Li *et al.*, “Optical performance of top-down fabricated InGaN/GaN nanorod light emitting diode arrays,” *Opt. Express* **19**(25), 25528 (2011).
- <sup>119</sup>F. Yu *et al.*, “Vertical architecture for enhancement mode power transistors based on GaN nanowires,” *Appl. Phys. Lett.* **108**(21), 213503 (2016).
- <sup>120</sup>G. Hamdانا *et al.*, “Nanoindentation of crystalline silicon pillars fabricated by soft UV nanoimprint lithography and cryogenic deep reactive ion etching,” *Sens. Actuators, A* **283**, 65–78 (2018).
- <sup>121</sup>G. Hamdانا *et al.*, “Towards fabrication of 3D isotopically modulated vertical silicon nanowires in selective areas by nanosphere lithography,” *Microelectron. Eng.* **179**, 74–82 (2017).
- <sup>122</sup>N. Markiewicz *et al.*, “Top-down fabrication of arrays of vertical GaN nanorods with freestanding top contacts for environmental exposure,” *Proceedings* **2**(13), 845 (2018).
- <sup>123</sup>T. Granz *et al.*, “Nanofabrication of vertically aligned 3D GaN nanowire arrays with sub-50 nm feature sizes using nanosphere lift-off lithography,” *Proceedings* **1**(4), 309 (2017).
- <sup>124</sup>S. Mariana *et al.*, “Vertical GaN nanowires and nanoscale light-emitting-diode arrays for lighting and sensing applications,” *ACS Appl. Nano Mater.* **2**(7), 4133–4142 (2019).
- <sup>125</sup>W. Wu *et al.*, “Nano-structured transmissive spectral filter matrix based on guided-mode resonances,” *J. Eur. Opt. Soc. Publ.* **15**(1), 19 (2019).

- <sup>126</sup>S. Merzsch *et al.*, "Production of vertical nanowire resonators by cryogenic-ICP-DRIE," *Microsyst. Technol.* **20**(4–5), 759–767 (2014).
- <sup>127</sup>D. Paramanik *et al.*, "Formation of large-area GaN nanostructures with controlled geometry and morphology using top-down fabrication scheme," *J. Vac. Sci. Technol., B* **30**(5), 52202 (2012).
- <sup>128</sup>M. F. Fatahilah *et al.*, "Traceable nanomechanical metrology of GaN micropillar array," *Adv. Eng. Mater.* **20**(10), 1800353 (2018).
- <sup>129</sup>J.-M. Lee, K.-M. Chang, S.-W. Kim, C. Huh, I.-H. Lee, and S.-J. Park, "Dry etch damage in n-type GaN and its recovery by treatment with an N<sub>2</sub> plasma," *J. Appl. Phys.* **87**(11), 7667–7670 (2000).
- <sup>130</sup>J. Liu *et al.*, "A practical route towards fabricating GaN nanowire arrays," *CrystEngComm* **13**(19), 5929 (2011).
- <sup>131</sup>C. H. Chiu *et al.*, "Fabrication of InGaN/GaN nanorod light-emitting diodes with self-assembled Ni metal islands," *Nanotechnology* **18**(44), 445201 (2007).
- <sup>132</sup>R. Debnath *et al.*, "Top-down fabrication of large-area GaN micro- and nano-pillars," *J. Vac. Sci. Technol., B* **32**(2), 21204 (2014).
- <sup>133</sup>K.-S. Im *et al.*, "Fabrication of normally-off GaN nanowire gate-all-around FET with top-down approach," *Appl. Phys. Lett.* **109**(14), 143106 (2016).
- <sup>134</sup>Q. Li *et al.*, "Single-mode GaN nanowire lasers," *Opt. Express* **20**(16), 17873 (2012).
- <sup>135</sup>Y.-W. Jo *et al.*, "First demonstration of GaN-based vertical nanowire FET with top-down approach," in *2015 73rd Annual Device Research Conference (DRC)* (IEEE, 2015).
- <sup>136</sup>A. Piquette, W. Bergbauer, B. Galler, and K. C. Mishra, "On choosing phosphors for near-UV and blue LEDs for white light," *ECS J. Solid State Sci. Technol.* **5**(1), R3146–R3159 (2016).
- <sup>137</sup>B. S. Tan, S. Yuan, and X. J. Kang, "Performance enhancement of InGaN light-emitting diodes by laser lift-off and transfer from sapphire to copper substrate," *Appl. Phys. Lett.* **84**(15), 2757–2759 (2004).
- <sup>138</sup>A. Laubsch, M. Sabathil, J. Baur, M. Peter, and B. Hahn, "High-power and high-efficiency InGaN-based light emitters," *IEEE Trans. Electron Devices* **57**(1), 79–87 (2010).
- <sup>139</sup>M. K. Kelly, O. Ambacher, R. Dimitrov, R. Handschuh, and M. Stutzmann, "Optical process for liftoff of group III-nitride films," *Phys. Status Solidi* **159**(1), R3–R4 (1997).
- <sup>140</sup>Y.-C. Wu *et al.*, "Air quality monitoring using mobile microscopy and machine learning," *Light: Sci. Appl.* **6**(9), e17046 (2017).
- <sup>141</sup>W. S. Wong *et al.*, "Fabrication of thin-film InGaN light-emitting diode membranes by laser lift-off," *Appl. Phys. Lett.* **75**(10), 1360–1362 (1999).
- <sup>142</sup>T. Ueda, M. Ishida, and M. Yuri, "Separation of thin GaN from sapphire by laser lift-off technique," *Jpn. J. Appl. Phys., Part 1* **50**(4), 041001 (2011).
- <sup>143</sup>H. Aoshima *et al.*, "Laser lift-off of AlN/sapphire for UV light-emitting diodes," *Phys. Status Solidi* **9**(3–4), 753–756 (2012).
- <sup>144</sup>N. Yulianto *et al.*, "Transferable substrateless GaN LED chips produced by femtosecond laser lift-off for flexible sensor applications," *Proceedings* **2**(13), 891 (2018).
- <sup>145</sup>S. Bornemann *et al.*, "Structural modifications in free-standing InGaN/GaN LEDs after femtosecond laser lift-off," *Proceedings* **2**(13), 897 (2018).
- <sup>146</sup>C. Lalau Keraly, L. Kuritzky, M. Cochet, and C. Weisbuch, "Light extraction efficiency Part A. Ray tracing for light extraction efficiency (LEE) modeling in nitride LEDs," in *III-Nitride Based Light Emitting Diodes and Applications*, edited by T. Y. Seong, J. Han, H. Amano, and H. Morkoc (Springer, Dordrecht, 2013), pp. 231–269.
- <sup>147</sup>A. David *et al.*, "Photonic bands in two-dimensionally patterned multimode GaN waveguides for light extraction," *Appl. Phys. Lett.* **87**(10), 101107 (2005).
- <sup>148</sup>K. H. Li, Y. F. Cheung, W. Y. Fu, K. K.-Y. Wong, and H. W. Choi, "Monolithic integration of GaN-on-sapphire light-emitting diodes, photodetectors, and waveguides," *IEEE J. Sel. Top. Quantum Electron.* **24**(6), 1–6 (2018).
- <sup>149</sup>L. Williams, G. Nehmetallah, and P. P. Banerjee, "Digital tomographic compressive holographic reconstruction of three-dimensional objects in transmissive and reflective geometries," *Appl. Opt.* **52**(8), 1702 (2013).
- <sup>150</sup>B. S. Yoon *et al.*, "Technology roadmap for automotive flexible display," *Planning and Roadmapping Technological Innovations* (Springer International Publishing, 2013), pp. 159–175.
- <sup>151</sup>C.-W. Sher *et al.*, "Large-area, uniform white light LED source on a flexible substrate," *Opt. Express* **23**(19), A1167 (2015).
- <sup>152</sup>K. Cherenack and L. van Pietersen, "Smart textiles: Challenges and opportunities," *J. Appl. Phys.* **112**(9), 091301 (2012).
- <sup>153</sup>A. Russo, B. Y. Ahn, J. J. Adams, E. B. Duoss, J. T. Bernhard, and J. A. Lewis, "Pen-on-paper flexible electronics," *Adv. Mater.* **23**(30), 3426–3430 (2011).
- <sup>154</sup>B. S. Yoon *et al.*, *Technology Roadmap for Automotive Flexible Display* (Springer, Cham, 2014), pp. 159–175.
- <sup>155</sup>R. Bao *et al.*, "Flexible and controllable piezo-phototronic pressure mapping sensor matrix by ZnO NW/p-polymer LED array," *Adv. Funct. Mater.* **25**(19), 2884–2891 (2015).
- <sup>156</sup>D. Kang, B. Gai, B. Thompson, S.-M. Lee, N. Malmstadt, and J. Yoon, "Flexible opto-fluidic fluorescence sensors based on heterogeneously integrated micro-VCSELs and silicon photodiodes," *ACS Photonics* **3**(6), 912–918 (2016).
- <sup>157</sup>J. Yoon *et al.*, "GaAs photovoltaics and optoelectronics using releasable multi-layer epitaxial assemblies," *Nature* **465**(7296), 329–333 (2010).
- <sup>158</sup>R.-H. Kim *et al.*, "Waterproof AlInGaP optoelectronics on stretchable substrates with applications in biomedicine and robotics," *Nat. Mater.* **9**(11), 929–937 (2010).
- <sup>159</sup>N. Guan, X. Dai, A. V. Babichev, F. H. Julien, and M. Tchernycheva, "Flexible inorganic light emitting diodes based on semiconductor nanowires," *Chem. Sci.* **8**(12), 7904–7911 (2017).
- <sup>160</sup>Samsung, <https://news.samsung.com/global/samsung-unveils-the-wall-the-worlds-first-modular-microoled-146-inch-tv> for "Samsung Unveils 'The Wall,' the World's First Modular MicroLED 146-inch TV" (2018); accessed 4 March 2019.
- <sup>161</sup>B. Richter *et al.*, "Bidirectional OLED microdisplay: Combining display and image sensor functionality into a monolithic CMOS chip," in *2011 IEEE International Solid-State Circuits Conference* (2011), pp. 314–316.
- <sup>162</sup>U. Vogel, P. Wartenberg, B. Richter, S. Brenner, K. Fehse, and M. Schober, "OLED-on-silicon microdisplays: technology, devices, applications," in *2018 48th European Solid-State Device Research Conference (ESSDERC)* (2018), pp. 90–93.
- <sup>163</sup>E. Virey, "Are microLEDs really the next display revolution?," *Inf. Disp.* **34**(3), 22–27 (2018).
- <sup>164</sup>D. Cuypers, H. De Smet, and A. Van Calster, "VAN LCOS microdisplays: A decade of technological evolution," *IEEE/OSA J. Disp. Technol.* **7**(3), 127–134 (2011).
- <sup>165</sup>H. X. Jiang and J. Y. Lin, "Nitride micro-LEDs and beyond—A decade progress review," *Opt. Express* **21**(S3), A475 (2013).
- <sup>166</sup>B. Kress and T. Starner, "A review of head-mounted displays (HMD) technologies and applications for consumer electronics," *Proc. SPIE* **8720**, 87200A (2013).
- <sup>167</sup>U. Vogel *et al.*, "Ultra-low power OLED microdisplay for extended battery life in NTE displays," *Soc. Inf. Disp. Tech. Pap.* **48**(1), 1125–1128 (2017).
- <sup>168</sup>W. Lukosz, "Optical systems with resolving powers exceeding the classical limit II," *J. Opt. Soc. Am.* **57**(7), 932 (1967).
- <sup>169</sup>B. Huang, M. Bates, and X. Zhuang, "Super-resolution fluorescence microscopy," *Annu. Rev. Biochem.* **78**(1), 993–1016 (2009).
- <sup>170</sup>R. Heintzmann and T. Huser, "Super-resolution structured illumination microscopy," *Chem. Rev.* **117**(23), 13890–13908 (2017).
- <sup>171</sup>J. Biteen and K. A. Willets, "Introduction: Super-resolution and single-molecule imaging," *Chem. Rev.* **117**(11), 7241–7243 (2017).
- <sup>172</sup>A. Jovicic, J. Li, and T. Richardson, "Visible light communication: Opportunities, challenges and the path to market," *IEEE Commun. Mag.* **51**(12), 26–32 (2013).
- <sup>173</sup>L. Yin and H. Haas, "Physical-layer security in multiuser visible light communication networks," *IEEE J. Sel. Areas Commun.* **36**(1), 162–174 (2018).
- <sup>174</sup>S. Rajbhandari *et al.*, "A review of gallium nitride LEDs for multi-gigabit-per-second visible light data communications," *Semicond. Sci. Technol.* **32**(2), 1–40 (2017).
- <sup>175</sup>H. Elgala, R. Mesleh, and H. Haas, "Indoor optical wireless communication: Potential and state-of-the-art," *IEEE Commun. Mag.* **49**(9), 56–62 (2011).
- <sup>176</sup>G. Stepniak, M. Schuppert, and C. A. Bunge, "Advanced modulation formats in phosphorous LED VLC links and the impact of blue filtering," *J. Lightwave Technol.* **33**(21), 4413–4423 (2015).
- <sup>177</sup>T. H. Do and M. Yoo, "Performance analysis of visible light communication using CMOS sensors," *Sensors* **16**(3), 1–23 (2016).

- <sup>178</sup>N. Franch, O. Alonso, J. Canals, A. Vilà, and A. Dieguez, "A low cost fluorescence lifetime measurement system based on SPAD detectors and FPGA processing," *J. Instrum.* **12**(02), C02070 (2017).
- <sup>179</sup>A. Dieguez, J. Canals, N. Franch, J. Dieguez, O. Alonso, and A. Vila, "A compact analog-histogramming SPAD-based CMOS chip for time-resolved fluorescence," *IEEE Trans. Biomed. Circuits Syst.* **13**, 343 (2019).
- <sup>180</sup>J. Grubor, S. Randel, K. D. Langer, and J. W. Walewski, "Bandwidth-efficient indoor optical wireless communications with white light-emitting diodes," in Proceedings of the 6th International Symposium on Communication Systems, Networks and Digital Signal Processing, CSNDSP 08 (2008), pp. 165–169.
- <sup>181</sup>A. Rashidi *et al.*, "Differential carrier lifetime and transport effects in electrically injected III-nitride light-emitting diodes," *J. Appl. Phys.* **122**(3), 035706 (2017).
- <sup>182</sup>J. D. McKendry *et al.*, "Visible-light communications using emitting-diode array," *J. Lightwave Technol.* **30**(1), 61–67 (2012).
- <sup>183</sup>S. Rajbhandari *et al.*, "A multigigabit per second integrated multiple-input multiple-output VLC demonstrator," *J. Lightwave Technol.* **35**(20), 4358–4365 (2017).
- <sup>184</sup>X. Li *et al.*, "Wireless visible light communications employing feed-forward pre-equalization and PAM-4 modulation," *J. Lightwave Technol.* **34**(8), 2049–2055 (2016).
- <sup>185</sup>H. Chun *et al.*, "Visible light communication using a blue GaN μLED and fluorescent polymer color converter," *IEEE Photonics Technol. Lett.* **26**(20), 2035–2038 (2014).
- <sup>186</sup>S. Zhang *et al.*, "1.5 Gbit/s multi-channel visible light communications using CMOS-controlled GaN-based LEDs," *J. Light. Technol.* **31**(8), 1211–1216 (2013).
- <sup>187</sup>Y.-C. Chi, D.-H. Hsieh, C.-T. Tsai, H.-Y. Chen, H.-C. Kuo, and G.-R. Lin, "450-nm GaN laser diode enables high-speed visible light communication with 9-Gbps QAM-OFDM," *Opt. Express* **23**(10), 13051 (2015).
- <sup>188</sup>Y.-C. Chi *et al.*, "Phosphorous diffused diverged blue laser diode for indoor lighting and communication," *Sci. Rep.* **5**(1), 18690 (2015).
- <sup>189</sup>J. R. D. Retamal *et al.*, "4-Gbit/s visible light communication link based on 16-QAM OFDM transmission over remote phosphor-film converted white light by using blue laser diode," *Opt. Express* **23**(26), 33656 (2015).
- <sup>190</sup>A. Rashidi, M. Monavarian, A. Aragon, A. Rishinaramangalam, and D. Feezell, "GHz-bandwidth nonpolar InGaN/GaN micro-LED operating at low current density for visible-light communication," in Conference Digest-IEEE International Semiconductor Laser Conference September (2018), Vol. 2018, pp. 57–58.
- <sup>191</sup>D. Lee, S. Ryu, U. Kim, D. Jung, and C. Joo, "Color-coded LED microscopy for multi-contrast and quantitative phase-gradient imaging," *Biomed. Opt. Express* **6**(12), 4912 (2015).
- <sup>192</sup>C. Zuo, J. Sun, J. Zhang, Y. Hu, and Q. Chen, "Lensless phase microscopy and diffraction tomography with multi-angle and multi-wavelength illuminations using a LED matrix," *Opt. Express* **23**(11), 14314 (2015).
- <sup>193</sup>L. Tian and L. Waller, "Quantitative differential phase contrast imaging in an LED array microscope," *Opt. Express* **23**(9), 11394 (2015).
- <sup>194</sup>X. Ou, R. Horstmeyer, C. Yang, and G. Zheng, "Quantitative phase imaging via Fourier ptychographic microscopy," *Opt. Lett.* **38**(22), 4845 (2013).
- <sup>195</sup>L. Tian and L. Waller, "3D intensity and phase imaging from light field measurements in an LED array microscope," *Optica* **2**(2), 104 (2015).
- <sup>196</sup>G. Zheng, C. Kolner, and C. Yang, "Microscopy refocusing and dark-field imaging by using a simple LED array," *Opt. Lett.* **36**(20), 3987 (2011).
- <sup>197</sup>Z. Liu, L. Tian, S. Liu, and L. Waller, "Real-time brightfield, darkfield, and phase contrast imaging in a light-emitting diode array microscope," *J. Biomed. Opt.* **19**(10), 106002 (2014).
- <sup>198</sup>G. Zheng, R. Horstmeyer, and C. Yang, "Wide-field, high-resolution Fourier ptychographic microscopy," *Nat. Photonics* **7**(9), 739–745 (2013).
- <sup>199</sup>L. Tian, X. Li, K. Ramchandran, and L. Waller, "Multiplexed coded illumination for Fourier ptychography with an LED array microscope," *Biomed. Opt. Express* **5**(7), 2376 (2014).
- <sup>200</sup>R. Heer *et al.*, "Preparation and integration of a multi-wavelength LED matrix for testing light cell interaction in a novel lens less optical microscope," *Proceedings* **2**(13), 1074 (2018).
- <sup>201</sup>E. McLeod and A. Ozcan, "Unconventional methods of imaging: Computational microscopy and compact implementations," *Rep. Prog. Phys.* **79**(7), 76001 (2016).
- <sup>202</sup>H. C. Koydemir, J. T. Coulibaly, D. Tseng, I. I. Bogoch, and A. Ozcan, "Design and validation of a wide-field mobile phone microscope for the diagnosis of schistosomiasis," *Travel Med. Infect. Dis.* **30**, 128–129 (2019).
- <sup>203</sup>I. Hernández-Neuta *et al.*, "Smartphone-based clinical diagnostics: Towards democratization of evidence-based health care," *J. Intern. Med.* **285**(1), 19–39 (2018).
- <sup>204</sup>Y. Rivenson *et al.*, "Deep learning enhanced mobile-phone microscopy," *ACS Photonics* **5**(6), 2354–2364 (2018).
- <sup>205</sup>L. Repetto, E. Piano, and C. Pontiggia, "Lensless digital holographic microscope with light-emitting diode illumination," *Opt. Lett.* **29**(10), 1132 (2004).
- <sup>206</sup>U. Gopinathan, G. Pedrini, and W. Osten, "Coherence effects in digital inline holographic microscopy," *J. Opt. Soc. Am. A* **25**(10), 2459 (2008).
- <sup>207</sup>A. Greenbaum, N. Akbari, A. Feizi, W. Luo, and A. Ozcan, "Field-portable pixel super-resolution colour microscope," *PLoS One* **8**(9), e76475 (2013).
- <sup>208</sup>M. K. Kim, "Principles and techniques of digital holographic microscopy," *SPIE Rev.* **1**(1), 018005 (2010).
- <sup>209</sup>W. Xu, M. H. Jericho, I. A. Meinertzhagen, and H. J. Kreuzer, "Digital in-line holography of microspheres," *Appl. Opt.* **41**(25), 5367 (2002).
- <sup>210</sup>D. Gabor, "A new microscopic principle," *Nature* **161**(4098), 777–778 (1948).
- <sup>211</sup>O. Mudanyali *et al.*, "Compact, light-weight and cost-effective microscope based on lensless incoherent holography for telemedicine applications," *Lab Chip* **10**(11), 1417 (2010).
- <sup>212</sup>S. Seo, T.-W. Su, D. K. Tseng, A. Erlinger, and A. Ozcan, "Lensfree holographic imaging for on-chip cytometry and diagnostics," *Lab Chip* **9**(6), 777–787 (2009).
- <sup>213</sup>A. Greenbaum *et al.*, "Imaging without lenses: Achievements and remaining challenges of wide-field on-chip microscopy," *Nat. Methods* **9**(9), 889–895 (2012).
- <sup>214</sup>V. Müller *et al.*, "Identification of pathogenic bacteria in complex samples using a smartphone based fluorescence microscope," *RSC Adv.* **8**(64), 36493–36502 (2018).
- <sup>215</sup>M. U. Daloglu *et al.*, "3D imaging of sex-sorted bovine spermatozoon locomotion, head spin and flagellum beating," *Sci. Rep.* **8**(1), 15650 (2018).
- <sup>216</sup>A. F. Coskun, A. E. Cetin, B. C. Galarreta, D. A. Alvarez, H. Altug, and A. Ozcan, "Lensfree optofluidic plasmonic sensor for real-time and label-free monitoring of molecular binding events over a wide field-of-view," *Sci. Rep.* **4**(1), 6789 (2014).
- <sup>217</sup>M. M. Shimogawa *et al.*, "Parasite motility is critical for virulence of African trypanosomes," *Sci. Rep.* **8**(1), 9122 (2018).
- <sup>218</sup>Y. Zhang *et al.*, "Accurate color imaging of pathology slides using holography and absorbance spectrum estimation of histochemical stains," *J. Biophotonics* **12**, e201800335 (2018).
- <sup>219</sup>Y. Zhang *et al.*, "High-throughput screening of encapsulated islets using wide-field lens-free on-chip imaging," *ACS Photonics* **5**(6), 2081–2086 (2018).
- <sup>220</sup>G. Scholz *et al.*, "LED-based tomographic imaging for live-cell monitoring of pancreatic islets in microfluidic channels," *Proceedings* **1**(4), 552 (2017).
- <sup>221</sup>G. Scholz *et al.*, "Continuous live-cell culture monitoring by compact lensless LED microscopes," *Proceedings* **2**(13), 877 (2018).
- <sup>222</sup>A. B. Dharmawan *et al.*, "Artificial neural networks for automated cell quantification in lensless LED imaging systems," *Proceedings* **2**(13), 989 (2018).
- <sup>223</sup>G. Scholz *et al.*, "Continuous live-cell culture imaging and single-cell tracking by computational lensfree LED microscopy," *Sensors* **19**(5), 1234 (2019).
- <sup>224</sup>I. Schmidt *et al.*, "Gold-modified indium tin oxide as a transparent window in optoelectronic diagnostics of electrochemically active biofilms," *Biosens. Bioelectron.* **94**, 74–80 (2017).
- <sup>225</sup>I. Pushkarsky *et al.*, "Automated single-cell motility analysis on a chip using lensfree microscopy," *Sci. Rep.* **4**(1), 4717 (2014).
- <sup>226</sup>M. S. Peery and L. Hesselink, "Wavelength selection for true-color holography," *Appl. Opt.* **33**(29), 6811 (1994).
- <sup>227</sup>W. Bishara *et al.*, "Holographic pixel super-resolution in portable lensless on-chip microscopy using a fiber-optic array," *Lab Chip* **11**(7), 1276 (2011).
- <sup>228</sup>D. Jung *et al.*, "Smartphone-based multi-contrast microscope using color-multiplexed illumination," *Sci. Rep.* **7**(1), 7564 (2017).
- <sup>229</sup>Z. F. Phillips *et al.*, "Multi-contrast imaging and digital refocusing on a mobile microscope with a domed LED array," *PLoS One* **10**(5), e0124938 (2015).
- <sup>230</sup>S. Mariana *et al.*, "Pinhole microLED array as point source illumination for miniaturized lensless cell monitoring systems," *Proceedings* **2**(13), 866 (2018).

- <sup>231</sup>W. Luo, Y. Zhang, A. Feizi, Z. Göröcs, and A. Ozcan, "Pixel super-resolution using wavelength scanning," *Light: Sci. Appl.* **5**(4), e16060 (2015).
- <sup>232</sup>Y. Wu, Y. Zhang, W. Luo, and A. Ozcan, "Demosaiced pixel super-resolution for multiplexed holographic color imaging," *Sci. Rep.* **6**(1), 28601 (2016).
- <sup>233</sup>M. Veli and A. Ozcan, "Computational sensing of *Staphylococcus aureus* on contact lenses using 3D imaging of curved surfaces and machine learning," *ACS Nano* **12**(3), 2554–2559 (2018).
- <sup>234</sup>Y. Rivenson, Z. Göröcs, H. Güneydin, Y. Zhang, H. Wang, and A. Ozcan, "Deep learning microscopy," *Optica* **4**(11), 1437 (2017).
- <sup>235</sup>Y. Rivenson, Y. Zhang, H. Güneydin, D. Teng, and A. Ozcan, "Phase recovery and holographic image reconstruction using deep learning in neural networks," *Light: Sci. Appl.* **7**(2), 17141 (2017).
- <sup>236</sup>W. Wu *et al.*, "Pixel-wise multispectral sensing system using nanostructured filter matrix for biomedical applications," *Proceedings* **2**(13), 880 (2018).
- <sup>237</sup>A. Greenbaum, W. Luo, B. Khademhosseini, T.-W. Su, A. F. Coskun, and A. Ozcan, "Increased space-bandwidth product in pixel super-resolved lens-free on-chip microscopy," *Sci. Rep.* **3**(1), 1717 (2013).
- <sup>238</sup>X. Hu, P. H. Bessette, J. Qian, C. D. Meinhart, P. S. Daugherty, and H. T. Soh, "Marker-specific sorting of rare cells using dielectrophoresis," *Proc. Natl. Acad. Sci.* **102**(44), 15757–15761 (2005).
- <sup>239</sup>J. K. Valley, S. Neale, H.-Y. Hsu, A. T. Ohta, A. Jamshidi, and M. C. Wu, "Parallel single-cell light-induced electroporation and dielectrophoretic manipulation," *Lab Chip* **9**(12), 1714 (2009).
- <sup>240</sup>R. Pethig, "Review article—Dielectrophoresis: Status of the theory, technology, and applications," *Biomicrofluidics* **4**(2), 22811 (2010).
- <sup>241</sup>X. Ding *et al.*, "On-chip manipulation of single microparticles, cells, and organisms using surface acoustic waves," *Proc. Natl. Acad. Sci.* **109**(28), 11105–11109 (2012).
- <sup>242</sup>Y. Yamakoshi, Y. Koitabashi, N. Nakajima, and T. Miwa, "Yeast cell trapping in ultrasonic wave field using ultrasonic contrast agent," *Jpn. J. Appl. Phys., Part 1* **45**(5B), 4712–4717 (2006).
- <sup>243</sup>D. J. Stevenson, F. Gunn-Moore, and K. Dholakia, "Light forces the pace: Optical manipulation for biophotonics," *J. Biomed. Opt.* **15**(4), 41503 (2010).
- <sup>244</sup>J. D. Adams, U. Kim, and H. T. Soh, "Multitarget magnetic activated cell sorter," *Proc. Natl. Acad. Sci.* **105**(47), 18165–18170 (2008).
- <sup>245</sup>P. Y. Chiou, A. T. Ohta, and M. C. Wu, "Massively parallel manipulation of single cells and microparticles using optical images," *Nature* **436**(7049), 370–372 (2005).
- <sup>246</sup>P.-Y. Chiou, A. T. Ohta, A. Jamshidi, H.-Y. Hsu, and M. C. Wu, "Light-actuated AC electroosmosis for nanoparticle manipulation," *J. Microelectromech. Syst.* **17**(3), 525–531 (2008).
- <sup>247</sup>K.-W. Huang, T.-W. Su, A. Ozcan, and P.-Y. Chiou, "Optoelectronic tweezers integrated with lensfree holographic microscopy for wide-field interactive cell and particle manipulation on a chip," *Lab Chip* **13**(12), 2278 (2013).
- <sup>248</sup>Y. Lu, Y. Huang, J. A. Yeh, and C. Lee, "Controllability of non-contact cell manipulation by image dielectrophoresis (iDEP)," *Opt. Quantum Electron.* **37**(13–15), 1385–1395 (2005).
- <sup>249</sup>H. Hsu, A. T. Ohta, P.-Y. Chiou, A. Jamshidi, S. L. Neale, and M. C. Wu, "Phototransistor-based optoelectronic tweezers for dynamic cell manipulation in cell culture media," *Lab Chip* **10**(2), 165–172 (2010).
- <sup>250</sup>A. T. Ohta *et al.*, "Optoelectronic tweezers for the manipulation of cells, microparticles, and nanoparticles," in *Recent Optical and Photonic Technologies*, edited by K. Y. Kim (InTech, 2010), Vol. 2, p. 64.
- <sup>251</sup>A. T. Ohta *et al.*, "Optically controlled cell discrimination and trapping using optoelectronic tweezers," *IEEE J. Sel. Top. Quantum Electron.* **13**(2), 235–243 (2007).
- <sup>252</sup>A. T. Ohta *et al.*, "Dynamic cell and microparticle control via optoelectronic tweezers," *J. Microelectromech. Syst.* **16**(3), 491–499 (2007).
- <sup>253</sup>S. L. Neale, A. T. Ohta, H.-Y. Hsu, J. K. Valley, A. Jamshidi, and M. C. Wu, "Trap profiles of projector based optoelectronic tweezers (OET) with HeLa cells," *Opt. Express* **17**(7), 5231 (2009).
- <sup>254</sup>H. Hwang and J.-K. Park, "Measurement of molecular diffusion based on optoelectrofluidic fluorescence microscopy," *Anal. Chem.* **81**(21), 9163–9167 (2009).
- <sup>255</sup>Y.-H. Lin, C.-M. Chang, and G.-B. Lee, "Manipulation of single DNA molecules by using optically projected images," *Opt. Express* **17**(17), 15318 (2009).
- <sup>256</sup>M. Hoeb, J. O. Rädler, S. Klein, M. Stutzmann, and M. S. Brandt, "Light-induced dielectrophoretic manipulation of DNA," *Biophys. J.* **93**(3), 1032–1038 (2007).
- <sup>257</sup>A. Zarowna-Dabrowska *et al.*, "Miniaturized optoelectronic tweezers controlled by GaN micro-pixel light emitting diode arrays," *Opt. Express* **19**(3), 2720 (2011).
- <sup>258</sup>A. H. Jeorrett *et al.*, "Optoelectronic tweezers system for single cell manipulation and fluorescence imaging of live immune cells," *Opt. Express* **22**(2), 1372 (2014).
- <sup>259</sup>H. X. Zhang *et al.*, "Individually-addressable flip-chip AlInGaN micropixelated light emitting diode arrays with high continuous and nanosecond output power," *Opt. Express* **16**(13), 9918 (2008).
- <sup>260</sup>H. Hwang, Y.-J. Choi, W. Choi, S.-H. Kim, J. Jang, and J.-K. Park, "Interactive manipulation of blood cells using a lens-integrated liquid crystal display based optoelectronic tweezers system," *Electrophoresis* **29**(6), 1203–1212 (2008).
- <sup>261</sup>S. Zhang, J. Juvert, J. M. Cooper, and S. L. Neale, "Manipulating and assembling metallic beads with optoelectronic tweezers," *Sci. Rep.* **6**(1), 32840 (2016).
- <sup>262</sup>S. L. Neale, M. Mazilu, J. I. B. Wilson, K. Dholakia, and T. F. Krauss, "The resolution of optical traps created by light induced dielectrophoresis (LIDEP)," *Opt. Express* **15**(20), 12619 (2007).
- <sup>263</sup>A. Grakoui, "The immunological synapse: A molecular machine controlling T cell activation," *Science* **285**(5425), 221–227 (1999).
- <sup>264</sup>J. K. Valley, A. Jamshidi, A. T. Ohta, H.-Y. Hsu, and M. C. Wu, "Operational regimes and physics present in optoelectronic tweezers," *J. Microelectromech. Syst.* **17**(2), 342–350 (2008).
- <sup>265</sup>H. Zhang *et al.*, "A reaction-based near-infrared fluorescent sensor for Cu<sup>2+</sup> detection in aqueous buffer and its application in living cells and tissues imaging," *Biosens. Bioelectron.* **94**, 24–29 (2017).
- <sup>266</sup>F. C. Hendriks *et al.*, "Single-molecule fluorescence microscopy reveals local diffusion coefficients in the pore network of an individual catalyst particle," *J. Am. Chem. Soc.* **139**(39), 13632–13635 (2017).
- <sup>267</sup>A. von Diezmann, Y. Shechtman, and W. E. Moerner, "Three-dimensional localization of single molecules for super-resolution imaging and single-particle tracking," *Chem. Rev.* **117**(11), 7244–7275 (2017).
- <sup>268</sup>M. Panagiotopoulou, S. Kunath, P. X. Medina-Rangel, K. Haupt, and B. Tse Sum Bui, "Fluorescent molecularly imprinted polymers as plastic antibodies for selective labeling and imaging of hyaluronan and sialic acid on fixed and living cells," *Biosens. Bioelectron.* **88**, 85–93 (2017).
- <sup>269</sup>J.-Y. Tinevez *et al.*, "TrackMate: An open and extensible platform for single-particle tracking," *Methods* **115**, 80–90 (2017).
- <sup>270</sup>M. I. Rowley, A. C. C. Coolen, B. Vojnovic, and P. R. Barber, "Robust Bayesian fluorescence lifetime estimation, decay model selection and instrument response determination for low-intensity FLIM imaging," *PLoS One* **11**(6), e0158404 (2016).
- <sup>271</sup>F. M. Della Rocca *et al.*, "Real-time fluorescence lifetime actuation for cell sorting using a CMOS SPAD silicon photomultiplier," *Opt. Lett.* **41**(4), 673 (2016).
- <sup>272</sup>G. Crivat and J. W. Taraska, "Imaging proteins inside cells with fluorescent tags," *Trends Biotechnol.* **30**(1), 8–16 (2012).
- <sup>273</sup>W. Xu, K. M. Chan, and E. T. Kool, "Fluorescent nucleobases as tools for studying DNA and RNA," *Nat. Chem.* **9**(11), 1043–1055 (2017).
- <sup>274</sup>J. X. Zhang *et al.*, "Predicting DNA hybridization kinetics from sequence," *Nat. Chem.* **10**(1), 91–98 (2017).
- <sup>275</sup>S. Huang, L. Wang, C. Huang, W. Su, and Q. Xiao, "Label-free and ratiometric fluorescent nanosensor based on amino-functionalized graphene quantum dots coupling catalytic G-quadruplex/hemin DNAzyme for ultrasensitive recognition of human telomere DNA," *Sens. Actuators, B: Chem.* **245**, 648–655 (2017).
- <sup>276</sup>L. Wei and D. Ho, "Recent advances in fluorescence lifetime analytical microsystems: Contact optics and CMOS time-resolved electronics," *Sensors* **17**(12), 2800 (2017).
- <sup>277</sup>X. Tang, P. Li, Q. Zhang, Z. Zhang, W. Zhang, and J. Jiang, "Time-resolved fluorescence immunochromatographic assay developed using two idiotypic nanobodies for rapid, quantitative, and simultaneous detection of aflatoxin

- and zearalenone in maize and its products," *Anal. Chem.* **89**(21), 11520–11528 (2017).
- <sup>278</sup>Q. Pian, R. Yao, N. Sinsuebphon, and X. Intes, "Compressive hyperspectral time-resolved wide-field fluorescence lifetime imaging," *Nat. Photonics* **11**(7), 411–414 (2017).
- <sup>279</sup>A. Boreham, R. Brodwolf, K. Walker, R. Haag, and U. Alexiev, "Time-resolved fluorescence spectroscopy and fluorescence lifetime imaging microscopy for characterization of dendritic polymer nanoparticles and applications in nanomedicine," *Molecules* **22**(1), 17 (2016).
- <sup>280</sup>J. Sipior, G. M. Carter, J. R. Lakowicz, and G. Rao, "Blue light-emitting diode demonstrated as an ultraviolet excitation source for nanosecond phase-modulation fluorescence lifetime measurements," *Rev. Sci. Instrum.* **68**(7), 2666–2670 (1997).
- <sup>281</sup>J. Sytsma, J. M. Vroom, C. J. de Grauw, and H. C. Gerritsen, "Time-gated fluorescence lifetime imaging and microvolume spectroscopy using two-photon excitation," *J. Microsc.* **191**(1), 39–51 (2008).
- <sup>282</sup>M. Rosenberg *et al.*, "Design, synthesis, and time-gated cell imaging of carbon-bridged triangulenium dyes with long fluorescence lifetime and red emission," *Chem. Sci.* **9**(12), 3122–3130 (2018).
- <sup>283</sup>G. Accocia, A. Cominelli, M. Ghioni, and I. Rech, "Fast fully-integrated front-end circuit to overcome pile-up limits in time-correlated single photon counting with single photon avalanche diodes," *Opt. Express* **26**(12), 15398 (2018).
- <sup>284</sup>A. Cominelli, G. Accocia, P. Peronio, I. Rech, and M. Ghioni, "Readout architectures for high efficiency in time-correlated single photon counting experiments—Analysis and review," *IEEE Photonics J.* **9**(3), 1–15 (2017).
- <sup>285</sup>V. Westphal, C. M. Blanca, M. Dyba, L. Kastrup, and S. W. Hell, "Laser-diode-stimulated emission depletion microscopy," *Appl. Phys. Lett.* **82**(18), 3125–3127 (2003).
- <sup>286</sup>G. Donnert, C. Eggeling, and S. W. Hell, "Major signal increase in fluorescence microscopy through dark-state relaxation," *Nat. Methods* **4**(1), 81–86 (2006).
- <sup>287</sup>A. D. Scully *et al.*, "Development of a laser-based fluorescence microscope with subnanosecond time resolution," *J. Fluoresc.* **6**(2), 119–125 (1996).
- <sup>288</sup>Q. Li, T. Ruckstuhl, and S. Seeger, "Deep-UV laser-based fluorescence lifetime imaging microscopy of single molecules," *J. Phys. Chem. B* **108**(24), 8324–8329 (2004).
- <sup>289</sup>P. Urayama *et al.*, "A UV-visible-NIR fluorescence lifetime imaging microscope for laser-based biological sensing with picosecond resolution," *Appl. Phys. B* **76**(5), 483–496 (2003).
- <sup>290</sup>G. J. M. Koper, J. Bonnet, J. G. M. Christiaanse, and J. S. Ploem, "An epilluminator/detector unit permitting arc lamp illumination for fluorescence activated cell sorters," *Cytometry* **3**(1), 10–14 (1982).
- <sup>291</sup>T. Araki and H. Misawa, "Light emitting diode-based nanosecond ultraviolet light source for fluorescence lifetime measurements," *Rev. Sci. Instrum.* **66**(12), 5469–5472 (1995).
- <sup>292</sup>C.-W. Jeon, H. W. Choi, and M. D. Dawson, "A novel fabrication method for a 64 × 64 matrix-addressable GaN-based micro-LED array," *Phys. Status Solidi A* **200**(1), 79–82 (2003).
- <sup>293</sup>W. J. O'Hagan, M. McKenna, D. C. Sherrington, O. J. Rolinski, and D. J. S. Birch, "MHz LED source for nanosecond fluorescence sensing," *Meas. Sci. Technol.* **13**(1), 84–91 (2002).
- <sup>294</sup>C. Griffin *et al.*, "Fluorescence excitation and lifetime measurements using GaN/InGaN micro-LED arrays," in *the 17th Annual Meeting of the IEEE Lasers and Electro-Optics Society, LEOS* (IEEE, 2004).
- <sup>295</sup>H. Robbins, K. Sumitomo, N. Tsujimura, and T. Kamei, "Integrated thin film Si fluorescence sensor coupled with a GaN microLED for microfluidic point-of-care testing," *J. Micromech. Microeng.* **28**(2), 24001 (2018).
- <sup>296</sup>P. A. Porta and H. D. Summers, "Vertical-cavity semiconductor devices for fluorescence spectroscopy in biochips and microfluidic platforms," *J. Biomed. Opt.* **10**(3), 34001 (2005).
- <sup>297</sup>E. Thrush *et al.*, "Integrated semiconductor vertical-cavity surface-emitting lasers and PIN photodetectors for biomedical fluorescence sensing," *IEEE J. Quantum Electron.* **40**(5), 491–498 (2004).
- <sup>298</sup>B. R. Rae *et al.*, "CMOS driven micro-pixel LEDs integrated with single photon avalanche diodes for time resolved fluorescence measurements," *J. Phys. D* **41**(9), 94011 (2008).
- <sup>299</sup>B. Rae *et al.*, "A CMOS time-resolved fluorescence lifetime analysis micro-system," *Sensors* **9**(11), 9255–9274 (2009).
- <sup>300</sup>B. R. Rae *et al.*, "A vertically integrated CMOS microsystem for time-resolved fluorescence analysis," *IEEE Trans. Biomed. Circuits Syst.* **4**(6), 437–444 (2010).
- <sup>301</sup>Z. Gong *et al.*, "Matrix-addressable micropixelated InGaN light-emitting diodes with uniform emission and increased light output," *IEEE Trans. Electron Devices* **54**(10), 2650–2658 (2007).
- <sup>302</sup>C. Niclass, A. Rochas, P.-A. Besse, R. S. Popovic, and E. Charbon, "CMOS imager based on single photon avalanche diodes," in *the 13th International Conference on Solid-State Sensors, Actuators and Microsystems, Digest of Technical Papers, TRANSDUCERS '05* (IEEE, 2005).
- <sup>303</sup>C.-W. Jeon, H. W. Choi, E. Gu, and M. D. Dawson, "High-density matrix-addressable AlInGaN-based 368-nm microarray light-emitting diodes," *IEEE Photonics Technol. Lett.* **16**(11), 2421–2423 (2004).
- <sup>304</sup>H. W. Choi, C. W. Jeon, and M. D. Dawson, "Fabrication of matrix-addressable micro-LED arrays based on a novel etch technique," *J. Cryst. Growth* **268**(3–4), 527–530 (2004).
- <sup>305</sup>K. Davitt *et al.*, "290 and 340 nm UV LED arrays for fluorescence detection from single airborne particles," *Opt. Express* **13**(23), 9548 (2005).
- <sup>306</sup>G. Patounakis, K. L. Shepard, and R. Levicky, "Active CMOS array sensor for time-resolved fluorescence detection," *IEEE J. Solid-State Circuits* **41**(11), 2521–2530 (2006).
- <sup>307</sup>H.-J. Yoon, S. Itoh, and S. Kawahito, "A CMOS image sensor with in-pixel two-stage charge transfer for fluorescence lifetime imaging," *IEEE Trans. Electron Devices* **56**(2), 214–221 (2009).
- <sup>308</sup>E. Charbon, "Towards large scale CMOS single-photon detector arrays for lab-on-chip applications," *J. Phys. D* **41**(9), 94010 (2008).
- <sup>309</sup>D. E. Schwartz, E. Charbon, and K. L. Shepard, "A Single-photon avalanche diode array for fluorescence lifetime imaging microscopy," *IEEE J. Solid-State Circuits* **43**(11), 2546–2557 (2008).
- <sup>310</sup>J. Zhang, M. A. Itzler, H. Zbinden, and J.-W. Pan, "Advances in InGaAs/InP single-photon detector systems for quantum communication," *Light: Sci. Appl.* **4**(5), e286 (2015).
- <sup>311</sup>S. Pellegrini *et al.*, "Design and performance of an InGaAs-InP single-photon avalanche diode detector," *IEEE J. Quantum Electron.* **42**(4), 397–403 (2006).
- <sup>312</sup>M. D. Eisaman, J. Fan, A. Migdall, and S. V. Polyakov, "Invited review article: Single-photon sources and detectors," *Rev. Sci. Instrum.* **82**(7), 71101 (2011).
- <sup>313</sup>M. A. Itzler *et al.*, "Advances in InGaAsP-based avalanche diode single photon detectors," *J. Mod. Opt.* **58**(3–4), 174–200 (2011).
- <sup>314</sup>A. F. Coskun, T.-W. Su, and A. Ozcan, "Wide field-of-view lens-free fluorescent imaging on a chip," *Lab Chip* **10**(7), 824 (2010).
- <sup>315</sup>T.-I. Kim *et al.*, "Injectable, cellular-scale optoelectronics with applications for wireless optogenetics," *Science* **340**(6129), 211–216 (2013).
- <sup>316</sup>J. G. McCall *et al.*, "Fabrication and application of flexible, multimodal light-emitting devices for wireless optogenetics," *Nat. Protoc.* **8**(12), 2413–2428 (2013).
- <sup>317</sup>J.-W. Jeong *et al.*, "Wireless optofluidic systems for programmable in vivo pharmacology and optogenetics," *Cell* **162**(3), 662–674 (2015).
- <sup>318</sup>F. Pisanello, L. Sileo, and M. D. Vittorio, "Micro- and nanotechnologies for optical neural interfaces," *Front. Neurosci.* **10**, 468 (2016).
- <sup>319</sup>F. Yang, C. Gao, P. Wang, G.-J. Zhang, and Z. Chen, "Fish-on-a-chip: Microfluidics for zebrafish research," *Lab Chip* **16**(7), 1106–1125 (2016).
- <sup>320</sup>W. Al-Atabany, B. McGovern, K. Mehran, R. Berlinguer-Palmini, and P. Degenaar, "A processing platform for optoelectronic/optogenetic retinal prosthesis," *IEEE Trans. Biomed. Eng.* **60**(3), 781–791 (2013).
- <sup>321</sup>J. M. Barrett, R. Berlinguer-Palmini, and P. Degenaar, "Optogenetic approaches to retinal prosthesis," *Vis. Neurosci.* **31**(4–5), 345–354 (2014).
- <sup>322</sup>P. Degenaar *et al.*, "Optobionic vision—A new genetically enhanced light on retinal prosthesis," *J. Neural Eng.* **6**(3), 35007 (2009).
- <sup>323</sup>T. Moser, "Optogenetic stimulation of the auditory pathway for research and future prosthetics," *Curr. Opin. Neurobiol.* **34**, 29–36 (2015).
- <sup>324</sup>C. Goßler *et al.*, "GaN-based micro-LED arrays on flexible substrates for optical cochlear implants," *J. Phys. D: Appl. Phys.* **47**(20), 205401 (2014).
- <sup>325</sup>V. H. Hernandez *et al.*, "Optogenetic stimulation of the auditory pathway," *J. Clin. Invest.* **124**(3), 1114–1129 (2014).

- <sup>326</sup>M. Jeschke and T. Moser, "Considering optogenetic stimulation for cochlear implants," *Hear. Res.* **322**, 224–234 (2015).
- <sup>327</sup>E. Klein, C. Gossler, O. Paul, and P. Ruther, "High-density  $\mu$ LED-based optical cochlear implant with improved thermomechanical behavior," *Front. Neurosci.* **12**, 659 (2018).
- <sup>328</sup>M. Häusser, "Optogenetics: The age of light," *Nat. Methods* **11**(10), 1012–1014 (2014).
- <sup>329</sup>S. K. Mohanty and V. Lakshminarayanan, "Optical techniques in optogenetics," *J. Mod. Opt.* **62**(12), 949–970 (2015).
- <sup>330</sup>V. Poher *et al.*, "Micro-LED arrays: A tool for two-dimensional neuron stimulation," *J. Phys. D: Appl. Phys.* **41**(9), 94014 (2008).
- <sup>331</sup>J. Tønnesen *et al.*, "Functional integration of grafted neural stem cell-derived dopaminergic neurons monitored by optogenetics in an in vitro Parkinson model," *PLoS One* **6**(3), e17560 (2011).
- <sup>332</sup>A. N. Yaroslavsky, P. C. Schulze, I. V. Yaroslavsky, R. Schober, F. Ulrich, and H.-J. Schwarzmaier, "Optical properties of selected native and coagulated human brain tissues in vitro in the visible and near infrared spectral range," *Phys. Med. Biol.* **47**(12), 2059–2073 (2002).
- <sup>333</sup>O. Volkov *et al.*, "Structural insights into ion conduction by channelrhodopsin 2," *Science* **358**(6366), eaan8862 (2017).
- <sup>334</sup>G. Nagel *et al.*, "Channelrhodopsin-2, a directly light-gated cation-selective membrane channel," *Proc. Natl. Acad. Sci. U.S.A.* **100**(24), 13940–13945 (2003).
- <sup>335</sup>L. Fenco, O. Yizhar, and K. Deisseroth, "The development and application of optogenetics," *Annu. Rev. Neurosci.* **34**(1), 389–412 (2011).
- <sup>336</sup>O. A. Sineshchekov, K.-H. Jung, and J. L. Spudich, "Two rhodopsins mediate phototaxis to low- and high-intensity light in *Chlamydomonas reinhardtii*," *Proc. Natl. Acad. Sci. U.S.A.* **99**(13), 8689–8694 (2002).
- <sup>337</sup>C. Bamann, T. Kirsch, G. Nagel, and E. Bamberg, "Spectral characteristics of the photocycle of channelrhodopsin-2 and its implication for channel function," *J. Mol. Biol.* **375**(3), 686–694 (2008).
- <sup>338</sup>G. Nagel, "Channelrhodopsin-1: A light-gated proton channel in green algae," *Science* **296**(5577), 2395–2398 (2002).
- <sup>339</sup>M. G. Shapiro, K. Homma, S. Villarreal, C.-P. Richter, and F. Bezanilla, "Infrared light excites cells by changing their electrical capacitance," *Nat. Commun.* **3**(1), 736 (2012).
- <sup>340</sup>N. Grossman *et al.*, "Multi-site optical excitation using ChR2 and micro-LED array," *J. Neural Eng.* **7**(1), 16004 (2010).
- <sup>341</sup>E. S. Boyden, F. Zhang, E. Bamberg, G. Nagel, and K. Deisseroth, "Millisecond-timescale, genetically targeted optical control of neural activity," *Nat. Neurosci.* **8**(9), 1263–1268 (2005).
- <sup>342</sup>F. Zhang *et al.*, "Multimodal fast optical interrogation of neural circuitry," *Nature* **446**(7136), 633–639 (2007).
- <sup>343</sup>V. Gradinariu *et al.*, "Molecular and cellular approaches for diversifying and extending optogenetics," *Cell* **141**(1), 154–165 (2010).
- <sup>344</sup>V. Gradinariu, M. Mogri, K. R. Thompson, J. M. Henderson, and K. Deisseroth, "Optical deconstruction of Parkinsonian neural circuitry," *Science* **324**(5925), 354–359 (2009).
- <sup>345</sup>L. Campagnola, H. Wang, and M. J. Zylka, "Fiber-coupled light-emitting diode for localized photostimulation of neurons expressing channelrhodopsin-2," *J. Neurosci. Methods* **169**(1), 27–33 (2008).
- <sup>346</sup>V. Poher *et al.*, "Optical sectioning microscopes with no moving parts using a micro-stripe array light emitting diode," *Opt. Express* **15**(18), 11196 (2007).
- <sup>347</sup>C.-W. Jeon, K.-S. Kim, and M. D. Dawson, "Fabrication of two-dimensional InGaN-based micro-LED arrays," *Phys. Status Solidi A* **192**(2), 325–328 (2002).
- <sup>348</sup>S. Ayub *et al.*, "Hybrid intracerebral probe with integrated bare LED chips for optogenetic studies," *Biomed. Microdev.* **19**(3), 49 (2017).
- <sup>349</sup>R. Scharf, T. Tsunematsu, N. McAlinden, M. D. Dawson, S. Sakata, and K. Mathieson, "Depth-specific optogenetic control in vivo with a scalable, high-density  $\mu$ LED neural probe," *Sci. Rep.* **6**(1), 28381 (2016).
- <sup>350</sup>S. Szobota *et al.*, "Remote control of neuronal activity with a light-gated glutamate receptor," *Neuron* **54**(4), 535–545 (2007).
- <sup>351</sup>B. McGovern *et al.*, "A new individually addressable micro-LED array for photogenetic neural stimulation," *IEEE Trans. Biomed. Circuits Syst.* **4**(6), 469–476 (2010).
- <sup>352</sup>S. Ayub, M. Schwaerzel, O. Paul, and P. Ruther, "An intracerebral probe with integrated  $10 \times 1 \mu$ LED array for optogenetic experiments at 460 nm," *Procedia Eng.* **120**, 472–475 (2015).
- <sup>353</sup>N. McAlinden *et al.*, "Thermal and optical characterization of micro-LED probes for in vivo optogenetic neural stimulation," *Opt. Lett.* **38**(6), 992 (2013).
- <sup>354</sup>N. McAlinden, E. Gu, M. D. Dawson, S. Sakata, and K. Mathieson, "Optogenetic activation of neocortical neurons in vivo with a sapphire-based micro-scale LED probe," *Front. Neural Circuits* **9**, 25 (2015).
- <sup>355</sup>S. M. Wellman *et al.*, "A materials roadmap to functional neural interface design," *Adv. Funct. Mater.* **28**(12), 1701269 (2017).
- <sup>356</sup>B. Fan and W. Li, "Miniaturized optogenetic neural implants: A review," *Lab Chip* **15**(19), 3838–3855 (2015).
- <sup>357</sup>A. N. Zorzos, E. S. Boyden, and C. G. Fonstad, "Multiwaveguide implantable probe for light delivery to sets of distributed brain targets," *Opt. Lett.* **35**(24), 4133 (2010).
- <sup>358</sup>A. N. Zorzos, J. Scholvin, E. S. Boyden, and C. G. Fonstad, "Three-dimensional multiwaveguide probe array for light delivery to distributed brain circuits," *Opt. Lett.* **37**(23), 4841 (2012).
- <sup>359</sup>T. V. F. Abaya, S. Blair, P. Tathireddy, L. Rieth, and F. Solzbacher, "A 3D glass optrode array for optical neural stimulation," *Biomed. Opt. Express* **3**(12), 3087 (2012).
- <sup>360</sup>F. Pisanello *et al.*, "Multipoint-emitting optical fibers for spatially addressable in vivo optogenetics," *Neuron* **82**(6), 1245–1254 (2014).
- <sup>361</sup>M. Pisanello, A. Della Patria, L. Sileo, B. L. Sabatini, M. D. Vittorio, and F. Pisanello, "Modal demultiplexing properties of tapered and nanostructured optical fibers for in vivo optogenetic control of neural activity," *Biomed. Opt. Express* **6**(10), 4014 (2015).
- <sup>362</sup>L. Grosenick, J. H. Marshel, and K. Deisseroth, "Closed-loop and activity-guided optogenetic control," *Neuron* **86**(1), 106–139 (2015).
- <sup>363</sup>A. Canales *et al.*, "Multifunctional fibers for simultaneous optical, electrical and chemical interrogation of neural circuits in vivo," *Nat. Biotechnol.* **33**(3), 277–284 (2015).
- <sup>364</sup>J. Lee, I. Ozden, Y.-K. Song, and A. V. Nurmikko, "Transparent intracortical microprobe array for simultaneous spatiotemporal optical stimulation and multichannel electrical recording," *Nat. Methods* **12**(12), 1157–1162 (2015).
- <sup>365</sup>G. Cui *et al.*, "Deep brain optical measurements of cell type-specific neural activity in behaving mice," *Nat. Protoc.* **9**(6), 1213–1228 (2014).
- <sup>366</sup>G. Cui *et al.*, "Concurrent activation of striatal direct and indirect pathways during action initiation," *Nature* **494**(7436), 238–242 (2013).
- <sup>367</sup>A. Morton, C. Murawski, S. R. Pulver, and M. C. Gather, "High-brightness organic light-emitting diodes for optogenetic control of *Drosophila* locomotor behaviour," *Sci. Rep.* **6**(1), 31117 (2016).
- <sup>368</sup>A. Steude, E. C. Witten, G. B. Miles, and M. C. Gather, "Arrays of microscopic organic LEDs for high-resolution optogenetics," *Sci. Adv.* **2**(5), e1600061 (2016).
- <sup>369</sup>M. A. Rossi, V. Go, T. Murphy, Q. Fu, J. Morizio, and H. H. Yin, "A wirelessly controlled implantable LED system for deep brain optogenetic stimulation," *Front. Integr. Neurosci.* **9**, 8 (2015).
- <sup>370</sup>F. Wu, E. Stark, P.-C. Ku, K. D. Wise, G. Buzsáki, and E. Yoon, "Monolithically integrated  $\mu$ LEDs on silicon neural probes for high-resolution optogenetic studies in behaving animals," *Neuron* **88**(6), 1136–1148 (2015).
- <sup>371</sup>R. U. Verma *et al.*, "Auditory responses to electric and infrared neural stimulation of the rat cochlear nucleus," *Hear. Res.* **310**, 69–75 (2014).
- <sup>372</sup>H. Cao, L. Gu, S. K. Mohanty, and J.-C. Chiao, "An integrated  $\mu$ LED optrode for optogenetic stimulation and electrical recording," *IEEE Trans. Biomed. Eng.* **60**(1), 225–229 (2013).
- <sup>373</sup>B. Fan, K. Y. Kwon, A. J. Weber, and W. Li, "An implantable, miniaturized SU-8 optical probe for optogenetics-based deep brain stimulation," in 36th Annual International Conference of the IEEE Engineering in Medicine and Biology Society (2014), pp. 450–453.
- <sup>374</sup>B. Fan *et al.*, "A polycrystalline diamond-based, hybrid neural interfacing probe for optogenetics," in 28th IEEE International Conference on Micro Electro Mechanical Systems (MEMS) (2015), pp. 616–619.
- <sup>375</sup>K. Y. Kwon, B. Sirowatka, A. Weber, and W. Li, "Opto- $\mu$ EECoG array: A hybrid neural interface with transparent  $\mu$ EECoG electrode array and

- integrated LEDs for optogenetics," *IEEE Trans. Biomed. Circuits Syst.* **7**(5), 593–600 (2013).
- <sup>376</sup>K. Y. Kwon, H.-M. Lee, M. Ghovanloo, A. Weber, and W. Li, "Design, fabrication, and packaging of an integrated, wirelessly-powered optrode array for optogenetics application," *Front. Syst. Neurosci.* **9**, 69 (2015).
- <sup>377</sup>N. McAlinden *et al.*, "Multisite microLED optrode array for neural interfacing," *Neurophotonics* **6**(3), 035010 (2019).
- <sup>378</sup>K. Y. Kwon, A. Khomenko, M. Haq, and W. Li, "Integrated slanted microneedle-LED array for optogenetics," in *35th Annual International Conference of the IEEE Engineering in Medicine and Biology Society (EMBC)* (IEEE, 2013).
- <sup>379</sup>M. Schwaerzel, P. Elmlinger, O. Paul, and P. Ruther, "Miniaturized 3x3 optical fiber array for optogenetics with integrated 460 nm light sources and flexible electrical interconnection," in *28th IEEE International Conference on Micro Electro Mechanical Systems (MEMS)* (IEEE, 2015).
- <sup>380</sup>R. Scharf *et al.*, "A compact integrated device for spatially-selective optogenetic neural stimulation based on the Utah Optrode Array," *Proc. SPIE BiOS* **10482**, 104820M (2018).
- <sup>381</sup>R. Scharf *et al.*, "Refined Utah optrode array and  $\mu$ LED array for deep cortical optogenetic stimulation in primates," in *Biophotonics Congress: Biomedical Optics Congress 2018 (Microscopy/Translational/Brain/OTS)* (OSA, 2018).
- <sup>382</sup>C. Wyart and F. Del Bene, "Let there be light: Zebrafish neurobiology and the optogenetic revolution," *Rev. Neurosci.* **22**(1), 121–130 (2011).
- <sup>383</sup>A. Soltan, G. Passetti, P. Maaskant, and P. Degenaar, "High density  $\mu$ LED array for retinal prothesis with a eye-tracking system," in *IEEE Biomedical Circuits and Systems Conference (BioCAS)* (IEEE, 2016).
- <sup>384</sup>A. Soltan *et al.*, "A head mounted device stimulator for optogenetic retinal prosthesis," *J. Neural Eng.* **15**(6), 65002 (2018).
- <sup>385</sup>P. P. Maaskant *et al.*, "High-speed substrate-emitting micro-light-emitting diodes for applications requiring high radiance," *Appl. Phys. Express* **6**(2), 22102 (2013).
- <sup>386</sup>M. Ruzzarin *et al.*, "Demonstration of UV-induced threshold voltage instabilities in vertical GaN nanowire array-based transistors," *IEEE Trans. Electron Devices* **66**(5), 2119–2124 (2019).
- <sup>387</sup>J. W. Jorgenson, "Chromatography: fundamentals and applications of chromatography and related differential migration methods, Part A: Fundamentals and techniques, 6th ed. journal of chromatography library, volume 69A," *J. Am. Chem. Soc.* **127**(12), 4540–4541 (2005).
- <sup>388</sup>K. Claus-Dieter and T. Wagner, *Gas Sensing Fundamentals* (Springer, New York, 2014).
- <sup>389</sup>K. Triyana *et al.*, "A highly sensitive safrole sensor based on polyvinyl acetate (PVAc) nanofiber-coated QCM," *Sci. Rep.* **9**(1), 15407 (2019).
- <sup>390</sup>J. Xu, M. Bertke, H. S. Wasisto, and E. Peiner, "Piezoresistive microcantilevers for humidity sensing," *J. Micromech. Microeng.* **29**(5), 053003 (2019).
- <sup>391</sup>M. Bertke, J. Xu, M. Fahrbach, A. Setiono, H. Wasisto, and E. Peiner, "Strategy toward miniaturized, Self-out-readable resonant cantilever and integrated electrostatic microchannel separator for highly sensitive airborne nanoparticle detection," *Sensors* **19**(4), 901 (2019).
- <sup>392</sup>R. Jaaniso and O. K. Tan, *Semiconductor Gas Sensors* (Woodhead Publishing Limited, 2013).
- <sup>393</sup>J. Huang and Q. Wan, "Gas sensors based on semiconducting metal oxide one-dimensional nanostructures," *Sensors* **9**(12), 9903–9924 (2009).
- <sup>394</sup>G. Korotcenkov, "Metal oxides for solid state gas sensors: What determines our choice?," *Mater. Sci. Eng. B* **139**, 1–23 (2015).
- <sup>395</sup>N. L. W. Septiani and B. Yuliarto, "Review—The development of gas sensor based on carbon nanotubes," *J. Electrochem. Soc.* **163**(3), B97–B106 (2016).
- <sup>396</sup>A. Kolmakov and M. Moskovits, "Chemical sensing and catalysis by one-dimensional metal-oxide nanostructures," *Annu. Rev. Mater. Res.* **34**(1), 151–180 (2004).
- <sup>397</sup>D. Gupta, D. Dutta, P. B. Barman, S. Basu, and S. K. Hazra, "A review on palladium with low dimensional configurations for chemical gas sensor applications," *Sens. Lett.* **14**(3), 211–233 (2016).
- <sup>398</sup>P. Qi *et al.*, "Toward large arrays of multiplex functionalized carbon nanotube sensors for highly sensitive and selective molecular detection," *Nano Lett.* **3**(3), 347–351 (2003).
- <sup>399</sup>M. W. G. Hoffmann *et al.*, "Highly selective SAM-nanowire hybrid NO<sub>2</sub> sensor: Insight into charge transfer dynamics and alignment of frontier molecular orbitals," *Adv. Funct. Mater.* **24**(5), 595–602 (2014).
- <sup>400</sup>M. W. G. Hoffmann *et al.*, "A highly selective and self-powered gas sensor via organic surface functionalization of p-Si/n-ZnO diodes," *Adv. Mater.* **26**(47), 8017–8022 (2014).
- <sup>401</sup>J. Schalwig *et al.*, "Hydrogen response mechanism of Pt–GaN Schottky diodes," *Appl. Phys. Lett.* **80**(7), 1222 (2002).
- <sup>402</sup>M. Stutzmann *et al.*, "GaN-based heterostructures for sensor applications," *Diam. Relat. Mater.* **11**(3–6), 886–891 (2002).
- <sup>403</sup>S. J. Pearson, B. S. Kang, S. Kim, F. Ren, B. P. Gila, C. R. Abernathy, J. Lin, and S. N. G. Chu, "GaN-based diodes and transistors for chemical, gas, biological and pressure sensing," *J. Phys.: Condens. Matter* **16**(29), R961 (2004).
- <sup>404</sup>R. Mehandru *et al.*, "AlGaN/GaN HEMT based liquid sensors," *Solid. State. Electron.* **48**(2), 351–353 (2004).
- <sup>405</sup>P. K. Clifford and D. T. Tuma, "Characteristics of semiconductor gas sensors I. Steady state gas response," *Sens. Actuators* **3**, 233–254 (1982).
- <sup>406</sup>P. K. Clifford and D. T. Tuma, "Characteristics of semiconductor gas sensors II. Transient response to temperature change," *Sens. Actuators* **3**, 255–281 (1982).
- <sup>407</sup>N. Taguchi, "Gas-detecting device," U.S. patent 3,631,436 (28 December 1971).
- <sup>408</sup>J. Fonollosa, L. Fernández, R. Huerta, A. Gutiérrez-Gálvez, and S. Marco, "Temperature optimization of metal oxide sensor arrays using mutual Information," *Sens. Actuators, B* **187**, 331–339 (2013).
- <sup>409</sup>I. Elmí, S. Zampolli, E. Cozzani, F. Mancarella, and G. C. Cardinali, "Development of ultra-low-power consumption MOX sensors with ppb-level VOC detection capabilities for emerging applications," *Sens. Actuators, B* **135**(1), 342–351 (2008).
- <sup>410</sup>S. Vallejos, I. Gràcia, O. Chmela, E. Figueras, J. Hubálek, and C. Cané, "Chemoresistive micromachined gas sensors based on functionalized metal oxide nanowires: Performance and reliability," *Sens. Actuators, B* **235**, 525–534 (2016).
- <sup>411</sup>J. D. Prades *et al.*, "Ultralow power consumption gas sensors based on self-heated individual nanowires," *Appl. Phys. Lett.* **93**(12), 123110 (2008).
- <sup>412</sup>J. D. Prades, R. Jimenez-Díaz, F. Hernandez-Ramirez, A. Cirera, A. Romano-Rodríguez, and J. R. Morante, "Harnessing self-heating in nanowires for energy efficient, fully autonomous and ultra-fast gas sensors," *Sens. Actuators, B* **144**(1), 1–5 (2010).
- <sup>413</sup>C. Fabrega, O. Casals, F. Hernández-Ramírez, and J. D. Prades, "A review on efficient self-heating in nanowire sensors: Prospects for very-low power devices," *Sens. Actuators, B* **256**, 797–811 (2017).
- <sup>414</sup>J. D. Prades *et al.*, "Equivalence between thermal and room temperature UV light-modulated responses of gas sensors based on individual SnO<sub>2</sub> nanowires," *Sens. Actuators, B* **140**(2), 337–341 (2009).
- <sup>415</sup>E. Espid and F. Taghipour, "UV-LED photo-activated chemical gas sensors: A review," *Crit. Rev. Solid State Mater. Sci.* **42**(5), 416–432 (2017).
- <sup>416</sup>J. D. Prades *et al.*, "A model for the response towards oxidizing gases of photo-activated sensors based on individual SnO<sub>2</sub> nanowires," *Phys. Chem. Chem. Phys.* **11**(46), 10881–10889 (2009).
- <sup>417</sup>J. Sun, J. Xu, Y. Yu, P. Sun, F. Liu, and G. Lu, "UV-activated room temperature metal oxide based gas sensor attached with reflector," *Sens. Actuators, B* **169**, 291–296 (2012).
- <sup>418</sup>B. Gong *et al.*, "UV irradiation-assisted ethanol detection operated by the gas sensor based on ZnO nanowires/optical fiber hybrid structure," *Sens. Actuators, B* **245**, 821–827 (2017).
- <sup>419</sup>C. Y. Wang *et al.*, "Integration of In<sub>2</sub>O<sub>3</sub> nanoparticle based ozone sensors with GaInN/GaN light emitting diodes," *Appl. Phys. Lett.* **91**(10), 103509 (2007).
- <sup>420</sup>J. H. Yu *et al.*, "Sensing mechanism and behavior of sputtered ZnCdO ozone sensors enhanced by photons for room- temperature operation," *J. Electron. Mater.* **42**(4), 720–725 (2013).
- <sup>421</sup>C. L. Hsu, L. F. Chang, and T. J. Hsueh, "Light-activated humidity and gas sensing by ZnO nanowires grown on LED at room temperature," *Sens. Actuators, B* **249**, 265–277 (2017).
- <sup>422</sup>O. Casals *et al.*, "A parts per billion (ppb) sensor for NO<sub>2</sub> with microwatt ( $\mu$ W) power requirements based on micro light plates," *ACS Sens.* **4**(4), 822 (2019).
- <sup>423</sup>V. M. Zhyrovetsky, D. I. Popovych, S. S. Savka, and A. S. Serednytski, "Nanopowder metal oxide for photoluminescent gas sensing," *Nanoscale Res. Lett.* **12**(1), 132 (2017).

- <sup>424</sup>C. Yang and C. Wöll, "IR spectroscopy applied to metal oxide surfaces: Adsorbate vibrations and beyond," *Adv. Phys. X* **2**(2), 373–408 (2017).
- <sup>425</sup>W. J. Salcedo, F. J. R. Fernandez, and J. C. Rubim, "Photoluminescence quenching effect on porous silicon films for gas sensors application," *Spectrochim. Acta, Part A* **60**(5), 1065–1070 (2004).
- <sup>426</sup>A. Bismuto *et al.*, "Room-temperature gas sensing based on visible photoluminescence properties of metal oxide nanobelts," *J. Opt. A* **8**(7), S585–S588 (2006).
- <sup>427</sup>S. Lettieri *et al.*, "On the mechanism of photoluminescence quenching in tin dioxide nanowires by NO<sub>2</sub> adsorption," *New J. Phys.* **10**(2), 043013 (2008).
- <sup>428</sup>O. Weidemann, P. K. Kandaswamy, E. Monroy, G. Jegert, M. Stutzmann, and M. Eickhoff, "GaN quantum dots as optical transducers for chemical sensors," *Appl. Phys. Lett.* **94**(11), 113108 (2009).
- <sup>429</sup>S. Paul, A. Helwig, G. Müller, and F. Furtmayr, "Opto-chemical sensor system for the detection of H<sub>2</sub> and hydrocarbons based on InGaN/GaN nanowires," *Sens. Actuators, B* **173**, 120–126 (2012).
- <sup>430</sup>K. Maier *et al.*, "Detection of oxidising gases using an optochemical sensor system based on GaN/InGaN nanowires," *Sens. Actuators, B* **197**, 87–94 (2014).
- <sup>431</sup>J. Teubert, P. Becker, F. Furtmayr, and M. Eickhoff, "GaN nanodisks embedded in nanowires as optochemical transducers," *Nanotechnology* **22**(27), 275505 (2011).
- <sup>432</sup>K. Maier, A. Helwig, G. Müller, P. Hille, J. Teubert, and M. Eickhoff, "Photoluminescence probing of complex H<sub>2</sub>O adsorption on InGaN/GaN nanowires," *Nano Lett.* **17**(2), 615–621 (2017).
- <sup>433</sup>R. M. Harrison and J. Yin, "Particulate matter in the atmosphere: which particle properties are important for its effects on health?," *Sci. Total Environ.* **249**(1–3), 85–101 (2000).
- <sup>434</sup>H. S. Wasisto, S. Merzsch, E. Uhde, A. Waag, and E. Peiner, "Handheld personal airborne nanoparticle detector based on microelectromechanical silicon resonant cantilever," *Microelectron. Eng.* **145**, 96–103 (2015).
- <sup>435</sup>C. Asbach *et al.*, "Comparability of portable nanoparticle exposure monitors," *Ann. Occup. Hyg.* **56**(5), 606–621 (2012).
- <sup>436</sup>J. Marra, M. Voetz, and H.-J. Kiesling, "Monitor for detecting and assessing exposure to airborne nanoparticles," *J. Nanopart. Res.* **12**(1), 21–37 (2010).
- <sup>437</sup>J. Marra, "Using the aerasense nanotracer for simultaneously obtaining several ultrafine particle exposure metrics," *J. Phys.: Conf. Ser.* **304**, 12010 (2011).
- <sup>438</sup>L. Morawska *et al.*, "Indoor aerosols: From personal exposure to risk assessment," *Indoor Air* **23**(6), 462–487 (2013).
- <sup>439</sup>M. Carminati *et al.*, "Capacitive detection of micrometric airborne particulate matter for solid-state personal air quality monitors," *Sens. Actuators, A* **219**, 80–87 (2014).
- <sup>440</sup>M. Bertke, G. Hamdانا, W. Wu, H. S. Wasisto, E. Uhde, and E. Peiner, "Analysis of asymmetric resonance response of thermally excited silicon micro-cantilevers for mass-sensitive nanoparticle detection," *J. Micromech. Microeng.* **27**(6), 64001 (2017).
- <sup>441</sup>H. S. Wasisto *et al.*, "Silicon resonant nanopillar sensors for airborne titanium dioxide engineered nanoparticle mass detection," *Sens. Actuators, B* **189**, 146–156 (2013).
- <sup>442</sup>H. S. Wasisto *et al.*, "Silicon nanowire resonators: Aerosol nanoparticle mass sensing in the workplace," *IEEE Nanotechnol. Mag.* **7**(2), 18–23 (2013).
- <sup>443</sup>H. S. Wasisto *et al.*, "Femtogram aerosol nanoparticle mass sensing utilising vertical silicon nanowire resonators," *Micro Nano Lett.* **8**(10), 554–558 (2013).
- <sup>444</sup>H. S. Wasisto, S. Merzsch, A. Waag, E. Uhde, T. Salthammer, and E. Peiner, "Evaluation of photoresist-based nanoparticle removal method for recycling silicon cantilever mass sensors," *Sens. Actuators, A* **202**, 90–99 (2013).
- <sup>445</sup>J. Yang *et al.*, "Piezoresistive silicon cantilever covered by ZnO nanorods for humidity sensing," *Procedia Eng.* **168**, 1114–1117 (2016).
- <sup>446</sup>H. S. Wasisto, E. Uhde, and E. Peiner, "Enhanced performance of pocket-sized nanoparticle exposure monitor for healthy indoor environment," *Build. Environ.* **95**, 13–20 (2016).
- <sup>447</sup>H. S. Wasisto, S. Merzsch, E. Uhde, A. Waag, and E. Peiner, "Partially integrated cantilever-based airborne nanoparticle detector for continuous carbon aerosol mass concentration monitoring," *J. Sens. Sens. Syst.* **4**(1), 111–123 (2015).
- <sup>448</sup>H. S. Wasisto, F. Steib, S. Merzsch, A. Waag, and E. Peiner, "Vertical silicon nanowire array-patterned microcantilever resonators for enhanced detection of cigarette smoke aerosols," *Micro Nano Lett.* **9**(10), 676–679 (2014).
- <sup>449</sup>H. S. Wasisto, K. Huang, S. Merzsch, A. Stranz, A. Waag, and E. Peiner, "Finite element modeling and experimental proof of NEMS-based silicon pillar resonators for nanoparticle mass sensing applications," *Microsyst. Technol.* **20**(4–5), 571–584 (2014).
- <sup>450</sup>H. S. Wasisto, Q. Zhang, S. Merzsch, A. Waag, and E. Peiner, "A phase-locked loop frequency tracking system for portable microelectromechanical piezoresistive cantilever mass sensors," *Microsyst. Technol.* **20**(4–5), 559–569 (2014).
- <sup>451</sup>A. Setiono *et al.*, "Real-time frequency tracking of an electro-thermal piezoresistive cantilever resonator with ZnO nanorods for chemical sensing," *Chemosensors* **7**(1), 2 (2019).
- <sup>452</sup>H. S. Wasisto, S. Merzsch, A. Waag, E. Uhde, T. Salthammer, and E. Peiner, "Airborne engineered nanoparticle mass sensor based on a silicon resonant cantilever," *Sens. Actuators, B* **180**, 77–89 (2013).
- <sup>453</sup>H. S. Wasisto, S. Merzsch, A. Waag, E. Uhde, T. Salthammer, and E. Peiner, "Portable cantilever-based airborne nanoparticle detector," *Sens. Actuators, B* **187**, 118–127 (2013).
- <sup>454</sup>K. Davitt *et al.*, "Spectroscopic sorting of aerosols by a compact sensor employing UV LEDs," *Aerosol Sci. Technol.* **40**(12), 1047–1051 (2006).
- <sup>455</sup>W. Luo *et al.*, "High throughput on-chip analysis of high-energy charged particle tracks using lensfree imaging," *Appl. Phys. Lett.* **106**(15), 151107 (2015).
- <sup>456</sup>E. McLeod *et al.*, "High-throughput and label-free single nanoparticle sizing based on time-resolved on-chip microscopy," *ACS Nano* **9**(3), 3265–3273 (2015).
- <sup>457</sup>Q. Wei, E. McLeod, H. Qi, Z. Wan, R. Sun, and A. Ozcan, "On-chip cytometry using plasmonic nanoparticle enhanced lensfree holography," *Sci. Rep.* **3**(1), 1699 (2013).
- <sup>458</sup>S. Merzsch *et al.*, "Cleaning of structured templates from nanoparticle accumulation using silicone," *Microsyst. Technol.* **18**(7–8), 835–842 (2012).
- <sup>459</sup>H. S. Wasisto *et al.*, "Femtogram mass measurement of airborne engineered nanoparticles using silicon nanopillar resonators," *Procedia Eng.* **47**, 289–292 (2012).
- <sup>460</sup>H. S. Wasisto *et al.*, "Determination of exposure to engineered carbon nanoparticles using a self-sensing piezoresistive silicon cantilever sensor," *Microsyst. Technol.* **18**(7–8), 905–915 (2012).
- <sup>461</sup>S. Merzsch *et al.*, "Low-weight electrostatic sampler for airborne nanoparticles," in *IEEE Sensors Proceedings* (2011), pp. 1177–1180.
- <sup>462</sup>L. D. Knibbs, R. J. de Dear, L. Morawska, and P. M. Coote, "A simple and inexpensive dilution system for the TSI 3007 condensation particle counter," *Atmos. Environ.* **41**(21), 4553–4557 (2007).
- <sup>463</sup>S. Shen, P. A. Jaques, Y. Zhu, M. D. Geller, and C. Sioutas, "Evaluation of the SMPS–APS system as a continuous monitor for measuring PM<sub>2.5</sub>, PM<sub>10</sub>, and coarse (PM<sub>2.5</sub>–10) concentrations," *Atmos. Environ.* **36**(24), 3939–3950 (2002).
- <sup>464</sup>G. J. Sem, "Design and performance characteristics of three continuous-flow condensation particle counters: A summary," *Atmos. Res.* **62**(3–4), 267–294 (2002).
- <sup>465</sup>C. Asbach *et al.*, "Comparison of four mobility particle sizers with different time resolution for stationary exposure measurements," *J. Nanopart. Res.* **11**(7), 1593–1609 (2009).
- <sup>466</sup>Y. Li Pan, J. Hartings, R. G. Pinnick, S. C. Hill, J. Halverson, and R. K. Chang, "Single-particle fluorescence spectrometer for ambient aerosols," *Aerosol Sci. Technol.* **37**(8), 628–639 (2003).
- <sup>467</sup>P. H. Kaye, W. R. Stanley, E. Hirst, E. V. Foot, K. L. Baxter, and S. J. Barrington, "Single particle multichannel bio-aerosol fluorescence sensor," *Opt. Express* **13**(10), 3583 (2005).
- <sup>468</sup>V. Sivaprakasam, A. L. Huston, C. Scotto, and J. D. Eversole, "Multiple UV wavelength excitation and fluorescence of bioaerosols," *Opt. Express* **12**(19), 4457 (2004).
- <sup>469</sup>L. M. Brosseau, D. Vesley, N. Rice, K. Goodell, M. Nellis, and P. Hairston, "Differences in detected fluorescence among several bacterial species measured with a direct-reading particle sizer and fluorescence detector," *Aerosol Sci. Technol.* **32**(6), 545–558 (2000).
- <sup>470</sup>Z. Ren *et al.*, "Growth, characterization, and application of high Al-content AlGaN and high power III-nitride ultraviolet emitters," *MRS Proc.* **831**, E1.4 (2004).
- <sup>471</sup>V. Adivarahan *et al.*, "High-power deep ultraviolet light-emitting diodes based on a micro-pixel design," *Appl. Phys. Lett.* **85**(10), 1838–1840 (2004).
- <sup>472</sup>Y.-L. Pan, V. Boutou, R. K. Chang, I. Ozden, K. Davitt, and A. V. Nurmiikko, "Application of light-emitting diodes for aerosol fluorescence detection," *Opt. Lett.* **28**(18), 1707 (2003).